UDK 66:54(05)
CODEN HMIDA 8
ISSN 0367–598X

2

Hemijska industrija

Vol. 79

Časopis Saveza hemijskih inženjera Srbije

Chemical Industry

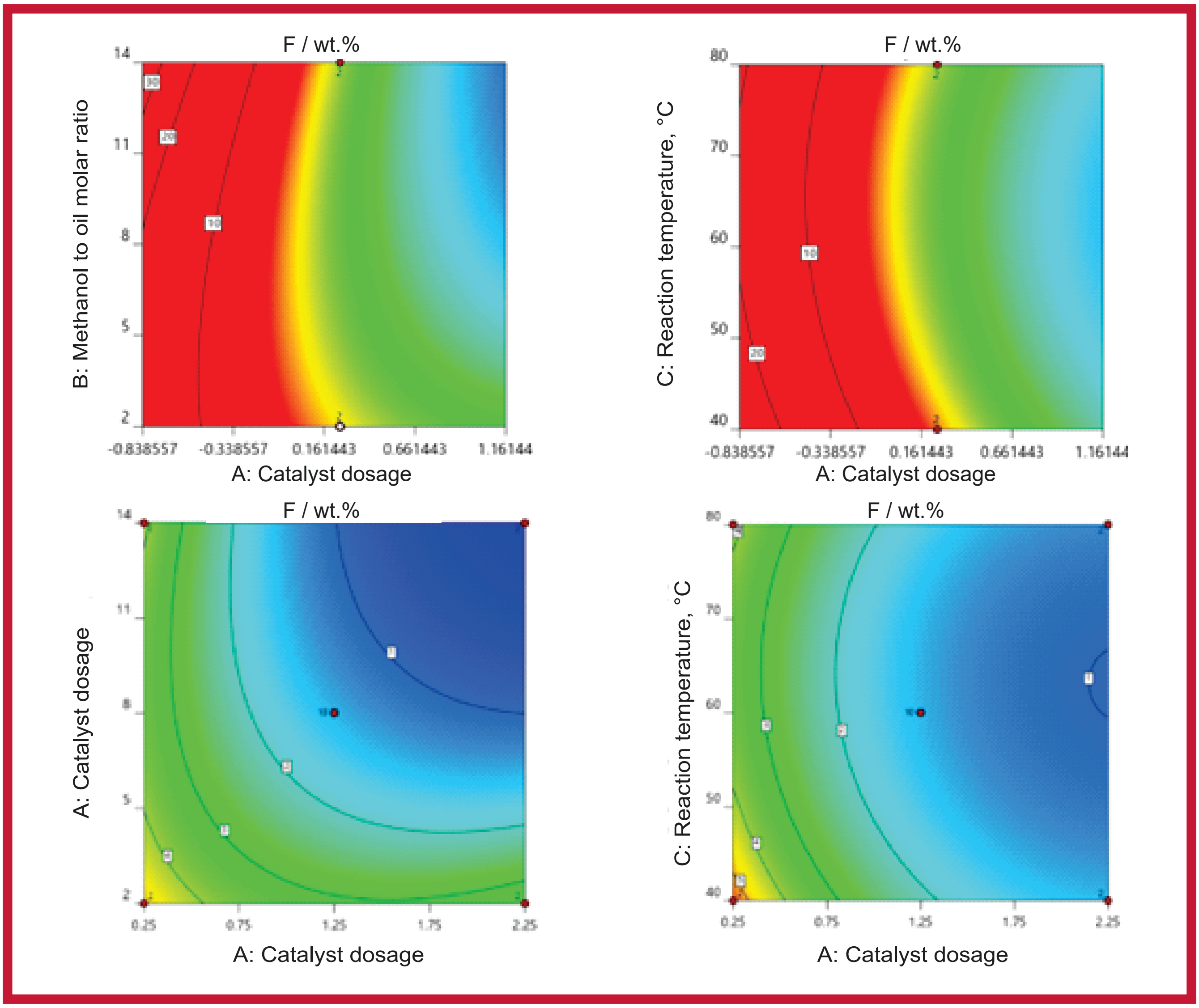

BEOGRAD, APRIL-JUN 2025.
HMIDA 8, 79(2) 69-125 (2025)

Aktivnosti Saveza hemijskih inženjera Srbije pomažu:

MINISTARSTVO NAUKE,
TEHNOLOŠKOG RAZVOJA
I INOVACIJA
REPUBLIKE SRBIJE

Tehnološko-metalurški fakultet
Univerziteta u Beogradu

Prirodno-matematički fakultet
Univerziteta u Novom Sadu

ITNMS
Institut za tehnologiju nuklearnih i
drugih mineralnih sirovina, Beograd

Tehnološki fakultet
Univerziteta u Novom Sadu

Institut za hemiju, tehnologiju i metalurgiju
Univerziteta u Beogradu

Fakultet tehničkih nauka
Univerziteta u Novom Sadu

Tehnološki fakultet
Univerziteta u Nišu, Leskovac

Fakultet tehničkih nauka
Univerziteta u Prištini
Kosovska Mitrovica

Institut IMS, Beograd

DCP HEMIGAL
Leskovac

Barič

Elixir Prahovo

Chemical Industry
Химическая промышленность

Hemijska industrija

Časopis Saveza hemijskih inženjera Srbije
Journal of the Association of Chemical Engineers of Serbia
Журнал Союза химических инженеров Сербии

VOL. 79 **Beograd, april – juni 2025.** **Broj 2**

Izdavač
Savez hemijskih inženjera Srbije
Beograd, Kneza Miloša 9/I

Likovno-grafičko rešenje naslovne strane
Milan Jovanović

Redakcija
11000 Beograd, Kneza Miloša 9/I
Tel/fax: 011/3240-018
E-pošta: shi@ache.org.rs
www.ache.org.rs

Izlazi kvartalno, rukopisi se ne vraćaju

Za izdavača: Ivana T. Drvenica

Sekretar redakcije: Slavica Desnica

Izdavanje časopisa pomaže
Republika Srbija, Ministarstvo nauke, tehnološkog razvoja i inovacija

Uplata pretplate i oglasnog prostora vrši se na tekući račun Saveza hemijskih inženjera Srbije, Beograd, broj 205-2172-71, Komercijalna banka a.d., Beograd

Menadžer časopisa i kompjuterska priprema
Aleksandar Dekanski

Štampa
Razvojno-istraživački centar grafičkog inženjerstva, Tehnološko-metalurški fakultet, Univerzitet u Beogradu, Karnegijeva 4, 11000 Beograd

Indeksiranje
Radovi koji se publikuju u časopisu *Hemijska Industrija* ideksiraju se preko *Thompson Reuters Scietific®* servisa *Science Citation Index - Expanded™* i *Journal Citation Report (JCR)*

SADRŽAJ/CONTENTS

Chemical Engineering/Hemijsko inženjerstvo

Biochemical Engineering/Biohemijsko inženjerstvo

Inorganic materials/Neorganski materijali

Biomaterials/Biomaterijali

Kinetic behaviour of the roasting/selective reduction process with the use of a mixture of bituminous coal and fuel oil as the additive

Hugo Javier Angulo-Palma[1,2], Manuel Saldana[3,4], Ángel Legrá Legrá[1], Alisa Lamorú Urgellés[1], Carlos Hernández Pedrera[5], Sandra Gallegos[3], Felipe M. Galleguillos Madrid[6] and Norman Toro[3]

[1]*Centro de Investigaciones del Níquel ``Alberto Fernández Montes de Oca´´ (CEDINIQ), Moa, Holguín, Cuba*
[2]*Departamento de Metalurgia Química, Universidad de Moa, Holguín, Cuba*
[3]*Faculty of Engineering and Architecture, Universidad Arturo Prat, Iquique, Chile*
[4]*Departamento de Ingeniería Química y Procesos de Minerales, Universidad de Antofagasta, Antofagasta, Chile*
[5]*Facultad de Ingeniería Química y Agronomía, Universidad de Oriente, Santiago de Cuba, Cuba*
[6]*Centro de Desarrollo Energético Antofagasta, Universidad de Antofagasta, Antofagasta, Chile*

Abstract

Lateritic ore is currently the main raw material that allows extraction of Ni by the Caron process. To date, the kinetic behaviour of the roasting/selective reduction process of lateritic nickeliferous ores on a pilot scale is largely unknown. In the present study, the kinetic behaviour, the controlling stage and the mechanisms that describe this process with the use of a mixture of 2 wt.% bituminous coal and 1.25 wt.% fuel oil as a reducing additive were determined during the evaluation of the high and low thermal profiles, respectively. The phases of the reduced/leached minerals and the fed ore were analysed by X-ray powder diffraction. It was observed that the mixture used as a reducing additive guarantees an adequate transformation in both thermal profiles; the relationship between the residual Ni and residence time is described by a first-order reaction with the determination coefficients greater than 0.949. Although the influence of post-combustion air is not analysed, the controlling stage was diffusion through the ash layer with an activation energy of 14.4060 kJ mol^{-1}. Thus, the most precise combination to describe the process is diffusion through the ash layer and the growth of the nuclei.

Keywords: Reaction kinetics and mechanisms; furnace operation; pyrometallurgy; lateritic nickeliferous ore; Caron process.

TECHNICAL PAPER

UDC: 622.782:622.348.1

Hem. Ind. **79(2)** 69-77 (2025)

1. INTRODUCTION

Nickel is considered a strategic and critical chemical element used in the production of nickel-cadmium and nickel-metal hydride batteries, as well as in the production of special steels and aerospace alloys [1]. With the explosion in the production of electric vehicles, the global demand for this metal is forecast to increase around 10 times from 2018 to 2025 [2]. Main reserves of this metal are found in sulphide and lateritic ores. As the supply of Ni sulphide ores gradually depletes, its extraction from laterite ores generates significant attention [3]. Laterites contain 72.2 % of the world's Ni reserves, with an increase in annual production from 2004 to the present from 42 to 69 % [4]. These deposits are produced by prolonged and deep weathering of Ni-silica-bearing ultramafic rocks, generally in humid tropical or subtropical climates, where the minerals will be classified into hydrated silicates, clay silicates and oxide deposits. One of the main technologies that is capable of extracting Ni from lateritic ores is the Caron process [5]. This technology combines pyrometallurgical and hydrometallurgical processes [6], and is based on leaching of previously reduced lateritic minerals with solutions of ammonium-ammoniacal carbonate ($(NH_4)_2CO_3$), reduction being one of the stages that most influences the extractions [7-9] and final costs [10,11].

Reduction of lateritic ore is carried out in Herreschoff multiple hearth furnaces. The furnaces are oil-fired and are operated at air deficiency to produce the required ratio of carbon monoxide to carbon dioxide in each hearth. Temperatures in the reduction zone are maintained at 700 to 800 °C [12].

Corresponding author: Norman Toro, Faculty of Engineering and Architecture, Antofagasta, Chile
E-mail: notoro@unap.cl

Paper received: 18 September 2024; Paper accepted: 20 March 2025; Paper published: 7 May 2025.
https://doi.org/10.2298/HEMIND240918005A

In general, different investigations recognize that the characteristics of the lateritic ore [13-15], the furnace operation [16-20] and the use of reducing additives [7,21-24] constitute the most important variables to control during the roasting/selective reduction process.

In previous research studies [25,26], specifically the ones focusing on the use of reducing additives in multiple hearth furnaces, it has been shown that the use of the mixture of bituminous coal and fuel oil at the concentrations of 2.0 wt.% and 1.25 wt.%, respectively (denoted here as BC2.0-FO1.25) benefits the process technically and economically.

Since the introduction of the reducing additive BC2.0-FO1.25 on commercial scales currently constitutes one of the main technological modifications that can benefit the Caron process, it is necessary to determine the kinetics and the controlling mechanism during the selective roasting/reduction of NiO, which is also justification of the present study.

2. METHODOLOGY

In this research, the main kinetic parameters and the controlling mechanism of the selective roasting/reduction process of NiO are determined with the use of the reducing additive of bituminous coal at 2.0 % by weight and fuel oil at 1.25 wt.% (denoted here as BC2-FO1.25) on a pilot scale. For this purpose, the installation that simulates the Caron process was used in the Centro de Investigaciones del Niquel: Alberto Fernández Montes de Oca, Moa, Cuba (CEDINIQ) [16,26]. The reduction process was carried out in a multi-hearth furnace (Fig. 1) composed of 17 hearths, listed from top to the bottom from hearth 0 (H-0) to 16 (H-16), enclosed in a metal cylinder 11 m high and 2.51 m in diameter, coated internally by a refractory material; the post-combustion air being fed by the furnace hearths 4 (H-4) and 6 (H-6). The residence time in the furnace is 80 min, considering the initial and final time at the exit of hearths 0 and 16, respectively.

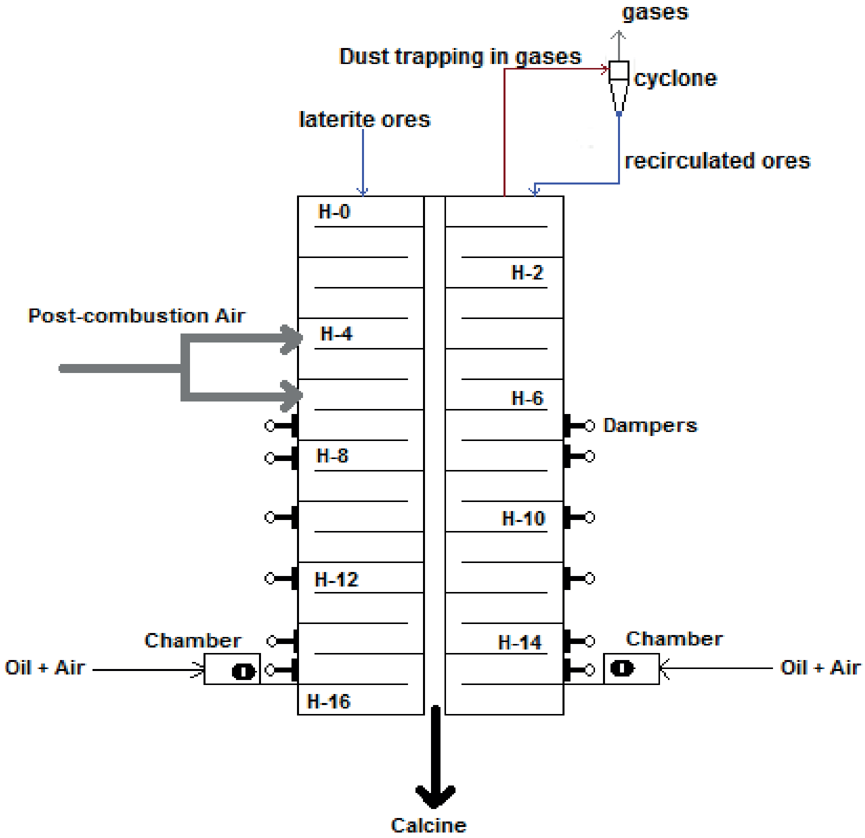

Figure 1. *Pilot plant scale reduction furnace; letter H designate hearth [26]*

The study was based on evaluating the conversion of NiO by analysing the kinetic data by the integral method, through the selection of kinetic equations with the objective of identifying the best fit of the experimental data, considering that the effect of reoxidation is insignificant. To confirm the controlling mechanism in the roasting/reduction processes, the value of the activation energy was used as a criterion, based on the development of the Arrhenius equation:

$$E_A = \frac{\log\left(\frac{k_{T_2}}{k_{T_1}}\right)\frac{R}{0.434152}\left(\frac{T_2T_1}{T_2\text{-}T_1}\right)}{1000} \tag{1}$$

where:

T_1 is the final temperature of the mineral reduced by the low thermal profile (LTP), K

T_2 is the final temperature of the mineral reduced by the high thermal profile (HTP), K

k_{T_1} is the reaction rate constant corresponding to the low thermal profile, min^{-1}

k_{T_2} is the reaction rate constant corresponding to the high thermal profile, min^{-1}

R is the universal gas constant, 8.314 J mol^{-1} K^{-1}

E_A E_A is the activation energy of the reduction process, kJ mol^{-1}

Thermal profiles shown in Figure 2 were used in the investigation. The high and low thermal profiles were used to facilitate the weakening of the crystalline structure by gradual heating in the temperature ranges that are used in commercial scales [10,12,16,26]. Temperature measurements within different hearths were carried out by using type K thermocouples (Taizhou Best Electric Equipment Co., Ltd., China). Experiments were repeated 3 times for each thermal profile.

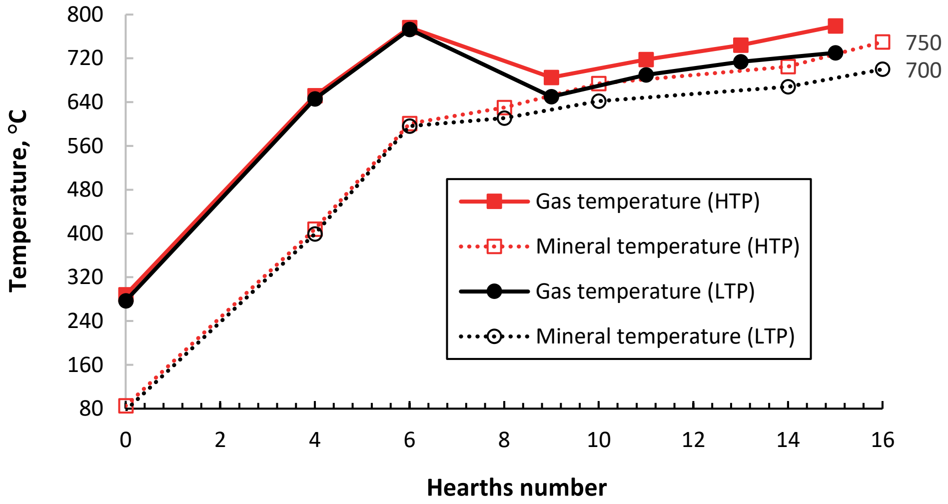

Figure 2. *Temperature profiles in the reduction furnace*

2. 1. Physical chemistry characteristics of the fed lateritic ore

Lateritic ore with a degree of homogenization greater than 90 % was fed to the furnace at a rate of 750 kg h^{-1}, after being dried and ground until the moisture content was less than 4 mass. % and the size distribution of particle less than 75 µm was from 84 to 88 %. Table 1 shows the main average (avg) characteristics of the mineral showing insignificant differences between the processed samples during the evaluation of the two thermal profiles in terms of the contents of Ni, Co, Fe, MgO, SiO_2, Al_2O_3, H_2O, C and S. The average component content (avg) of lateritic mineral in both LTP and HTP was similar with standard deviation (σ) values less than 1.56 and particle size distribution of the ore suitable for processing by the Caron process.

Table 1. *Characteristics of the lateritic mineral with the two thermal profiles evaluated in the reduction process.*

Thermal profile		Content, wt.%												
		Component									Particle size, µm			
		Ni	Co	Fe	MgO	SiO_2	Al_2O_3	H_2O	S	C	150	75	45	<45
LTP	avg	1.165	0.098	38.921	3.153	7.696	7.916	3.225	0.255	2.081	3.844	10.078	6.598	79.481
	σ	0.014	0.005	0.873	0.168	0.367	0.357	0.420	0.016	0.010	0.694	1.552	1.365	0.918
HTP	avg	1.167	0.099	39.323	2.828	7.788	8.080	3.660	0.251	2.088	3.425	9.783	7.392	79.400
	σ	0.013	0.001	0.416	0.513	0.249	0.228	0.190	0.018	0.032	0.698	0.585	1.133	1.500

2. 2. Chemical analysis and mineralogical characteristics of the reduced/leached samples

The reduced ore samples were taken from the even hearths of the furnace using the procedure proposed previously [16,18]. Each sample was then leached with the ammonium carbonate solution at a concentration of NH_3 from 80 to 85 g dm^{-3} and CO_2 from 40 to 42 g dm^{-3} for 2 h at a liquid/solid mass ratio (L/S) of 10/1.

The individual elements of interest in the leached mineral were determined by atomic absorption spectrometry (AAS, model SOLAR 929, Solar System ATI, Unicam Analytical Technology Inc., Cambridge, UK).

The crystalline structure and composition of the reduced/leached minerals were analysed by powder X-ray diffraction (XRD) by a PANalytical X'PERT3 diffractometer (Malvern Panalytical, UK) with Gonio type sweep in 2θ angular registration from 4.0042° to 79.9962°, with step distance of 0.0080° with Cu radiation and nickel filter, potential difference of 40 kV, current of 30 mA and a calibration checked by an external silicon standard scanning. Fractions of nickel, iron, and cobalt reduced to the metallic state of the ore in H16 were determined by leaching the reacted samples with a bromine-ethanol solution [27] followed by AAS analysis with flame and generator hydride (model SOLAR 929, Solar System ATI, Unicam Analytical Technology Inc., Cambridge, UK).

2. 3. Determination of the controlling mechanism in the roasting/reduction process

The controlling mechanism of the roasting/reduction process was determined by evaluating the equations of the unreacted core model reported by Levenvspiel [28] and the nucleation models reported by Bo *et al.* [29], typical of heterogeneous solid-fluid reactions. Table 2 shows the equations used.

Table 2. Controlling mechanisms analysed

Model type	Controlling mechanism	Equation
Unreacted core	Diffusion through the gas film (DGF)	$x_{Ni}=k_{DGF}t$
	Diffusion through the ash layer (DAL)	$1\text{-}3(1\text{-}x_{Ni})^{2/3}+2(1\text{-}x_{Ni})=k_{DAL}t$
	Chemical reaction (ChR)	$1\text{-}(1\text{-}x_{Ni})^{1/3}=k_{ChR}t$
Nucleation	2-D growth of nuclei (GN-2)	$\left[\text{-ln}(1\text{-}x_{Ni})\right]^{1/2}=k_{GN\text{-}2}t$
	3-D growth of nuclei (GN-3)	$\left[\text{-ln}(1\text{-}x_{Ni})\right]^{1/3}=k_{GN\text{-}3}t$
	5-D growth of nuclei (GN-5)	$\left[\text{-ln}(1\text{-}x_{Ni})\right]^{1/5}=k_{GN\text{-}5}t$

In Table 2 x_{Ni} is the conversion ratio of Ni (degree of reduction) and t is the time, while k_{DGF}, k_{DAL}, k_{ChR}, k_{GN-2}, k_{GN-3} and k_{GN-5} are the rate constants for each proposed mechanism.

3. RESULTS AND DISCUSSIONS

3. 1. Effect of the thermal profile with the use of the BC2-FO1.25 additive

Figure 3 shows the XRD patterns of the fed and reduced/leached lateritic ore samples corresponding to each thermal profile analysed.

It is observed that iron oxides and oxihydroxides (goethite, maghemite and hematite) as well as aluminium hydroxide (gibbsite) predominated in the lateritic ore fed. The secondary phases grouped the contents of silicon and magnesium, identifying the phases of hydrated magnesium silicate (lizardite), aluminium and magnesium oxide (spinel) and some silicon oxide (quartz).

The main mineralogical phases identified in the reduced/leached mineral, regardless of the thermal profile evaluated, were iron oxides (magnetite and maghemite, syn), magnesium iron aluminium chromium oxide (magnesiochromite, ferroan) and magnesium iron silicate (fayalite). These identified phases coincide with those reported by different studies [26,30] and indicate that during the evaluation of both thermal profiles an adequate roasting reduction process is achieved.

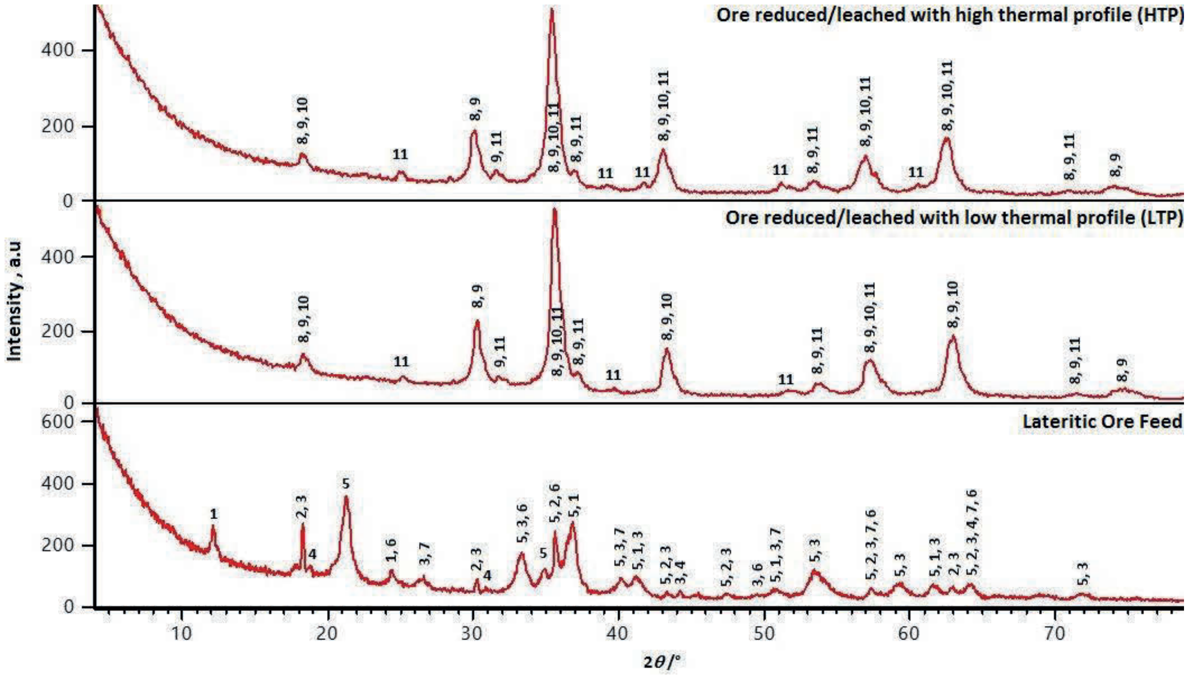

Figure 3. *XRD patterns of reduced/leached lateritic mineral samples with the use of BC2-FO1.25 additive and two thermal profiles. 1 - lizardite: $Mg_3Si_2O_5(OH)_4$; 2 - maghemite: $Fe_{21.16}O_{31.92}$; 3 - gibbsite: $Al(OH)_3$; 4 - spinel: $MgAl_2O_4$; 5 - goethite: FeOOH; 6 - hematite: Fe_2O_3; 7 - quartz: SiO_2; 8 - magnetite, syn: Fe_3O_4; 9 - maghemite, syn: Fe_2O_3; 10 - magnesiochromite, ferroan: $[(Mg, Fe)(Cr, Al)_2O_4]$ and 11 - fayalite: $Mg_{26}Fe_{1,74}(SiO_4)$.*

Formation of fayalite and magnesiumchromite, ferroane in the reduced and leached mineral (Fig. 3), justify the presence of non-leachable Ni contents in the process. These results agree with those obtained by Rhamdhani *et al.* [31-33], when identifying that the mineralogical phases of olivine and ferro-chromite spinels are not leached by the carbonate-ammonia technology. The presence of fayalite in both thermal profiles confirms that the reduced mineral reaches temperatures greater than and equal to 700 °C and that the use of the additive BC2-FO1.25 allows an adequate transformation of the serpentinitic phases. This finding coincides with the results of Valix & Cheung [34,35] during the evaluation of S as a reducing additive in the Caron process in the temperature range of 600 to 800 °C.

Although both thermal profiles present similarity, the shape of the peaks in the high thermal profile (HTP) became sharper, indicating an increase in the crystalline nature of the roasted product.

3. 2. Activation energy corresponding to the roasting/reduction process with the use of the additive BC2-FO1.25

Figure 4 relates the average $Ni_{residual}$ (residual Ni mass percentage after the reduction/leaching process) in the pilot Herreshoff furnace as a function of time, for the two thermal profiles evaluated. All data are presented in Supplementary Material S1 and S2. The decrease in the percentage of residual Ni as the residence time increases for both thermal profiles is observed as a trend, a regularity typical of an adequate reduction process in which the effects of reoxidation of the reduced mineral are minimized.

The behaviour presented by the high and low thermal profile curves indicates that the kinetic process of the general transformation of NiO into Ni^o adjusts to a first-order reaction with a coefficient of determination greater than 0.9490; this behaviour coincides with that reported by Shoubao [36] and Castellanos [37] during the evaluation of the roasting/reduction process of nickel-bearing lateritic ores. The average feed Ni percentage ranged from 1.1550 to 1.1780 wt.%, which corresponds to the chemical characteristics of the lateritic ore used in the study, see Table 1.

The average reaction rate constant at the low thermal profile (k_{T1}) was 0.0176 min^{-1}, which is for about 8.3 % lower than that achieved when using the high temperature profile (Figure 4); aspect that confirms compliance with the Arrhenius equation. Substitution of the values of the reaction rate constant and the final temperature of the reduced mineral in Equation (1) allows obtaining an activation energy of 14.4060 kJ mol^{-1} when using the additive BC2-FO1.25 in the process of roasting/reduction (Table 3).

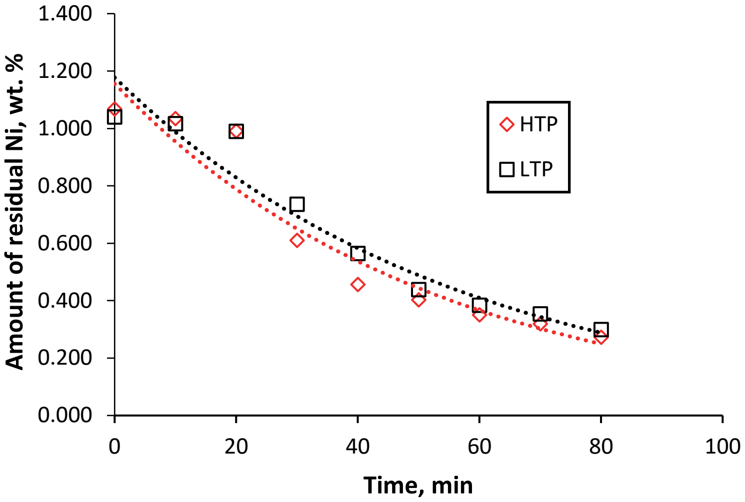

Figure 4. *NiO reduction kinetics on a pilot scale at two temperature profiles and with the use of the BC2-FO1.25 additive*

Table 3. *Activation energy and reaction rate constants with the reducing additive BC2-FO1.25*

Thermal profile				E_A / kJ mol^{-1}
Low		High		
k_{T_1} / min^{-1}	T_1/ °C	k_{T_2} / min^{-1}	T_2 / °C	
0.0176	700	0.0192	750	14.4060

The value of the activation energy with the BC2-FO1.25 additive corresponds to those reported, at laboratory scale during the evaluation of the reduction process in the temperature range of 675 to 800 °C, by Castellanos [37] (17.1544 kJ mol^{-1} for laterites from the Nicaro region with the fuel oil additive at 2.5 wt.%) and Ilyas [21] (13.80 kJ mol^{-1} for laterites from Bajaur, Pakistan with a mixture of 10 wt.% of coal and 9 wt.% of Na_2SO_4).

3. 3. Determination of the controlling stage of the roasting/reduction process with the use of the additive BC2-FO1.25

Table 4 shows the results of determination of the controlling stage in the roasting/reduction process for the high and low thermal profiles, when considering the unreacted nucleus models for particles of constant size and growth of nuclei.

Table 4. *Predicted times for reaction completion according to different controlling mechanisms shown in Table 2*

Thermal profile	Complete reaction time, min					
	Chemical reaction	Diffusion		Growth of nuclei		
		Through the gas film	Through the ash layer	GN-2	GN-3	GN-5
High	203	98	277	59	59	59
Low	230	103	336	64	62	61

The analysis of the complete reaction times allows us to identify that the controlling stage of the process is diffusion through the ash layer (DAL), with times necessary to complete the reaction of 277 and 336 min for the high and low thermal profiles, respectively. The controlling stage in the process was directly related to the activation energy value obtained in this study (value less than 17 kJ mol^{-1}, Table 3) and to the mechanism reported during the roasting/reduction of lateritic ores in different investigations [14,21,36-38].

To identify the mechanism that best describes the lateritic ore roasting/reduction process with the use of the additive BC2-FO1.25 and the high and low thermal profiles, possible combinations between the ChR, DGF, DAL and GN models were evaluated. To identify the mechanism that best describes the lateritic ore roasting/reduction process with the use of the additive BC2-FO1.25 and the high and low thermal profiles, possible combinations between the ChR, DGF, DAL and GN models were evaluated, according to the procedure described by Levenspiel [28]. The mechanism that best describes the roasting/reduction process in the low thermal profile (LTP) is the combination of the diffusion model through the ash layer (DAL) and growth of the nuclei (GN-5) with a coefficient of determination of 0.9838. In the case of the high thermal profile (HTP), it is observed that the most accurate combination to describe the process is diffusion through the ash layer (DAL) and the growth of nuclei (GN-3) with a correlation of 0.9623. (See Figure 5). These results are logical and justified because the increase in temperature causes an increase in the work per gram-molecule necessary to form a growth nucleus.

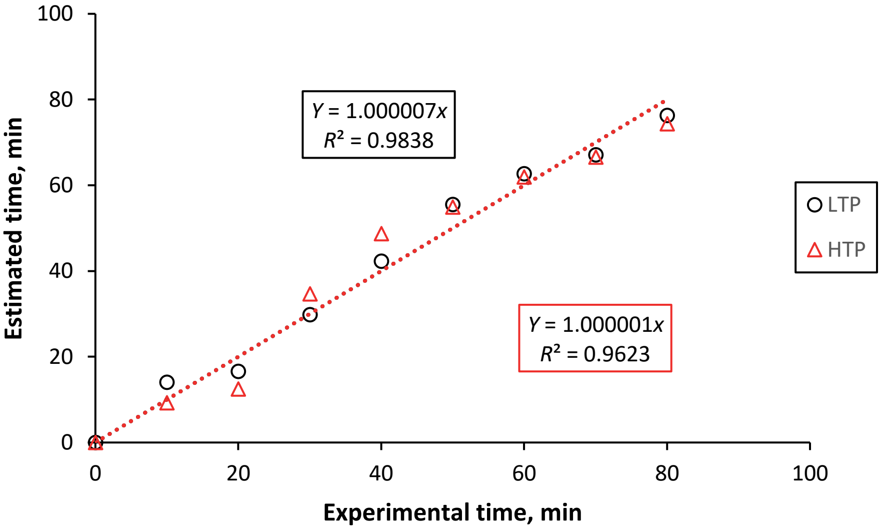

Figure 5. *Combinations of mechanisms (DAL and GN) to describe the roasting/reduction process of lateritic ore with the use of the additive BC2-FO1.25*

4. CONCLUSIONS

The BC2-FO1.25 additive can guarantee adequate mineralogical transformations in the roasting/reduction process of lateritic ores with a predominance of iron oxides-oxihydroxides at the use of high and low thermal profiles. The results of this study suggest that the relationship between the average $\mathrm{Ni}_{\mathrm{residual}}$ percentage after the reduction/leaching process and residence time is described by a first-order reaction with determination coefficients greater than 0.9490. The pilot-scale kinetic behaviours for both thermal profiles evaluated indicate that the controlling mechanism is diffusion through the ash layer, with complete reaction times that ranged from 276 to 336 min and an activation energy of 14.4060 kJ mol^{-1}.

Supplementary material

Additional data are available electronically at https://www.ache-pub.org.rs/index.php/HemInd/article/view/1385 or from the corresponding author on request.

Declaration of interest statement: The authors declare they have no conflict of interest.

Acknowledgement: Manuel Saldana acknowledges the infrastructure and support from Doctorado en Ingeniería de Procesos de Minerales at the Universidad de Antofagasta.

REFERENCES

[1] Bartzas G, Tsakiridis PE, Komnitsas K. Nickel industry: Heavy metal(loid)s contamination - sources, environmental impacts and recent advances on waste valorization. *Curr Opin Environ Sci Heal.* 2021; 21: 100253. https://doi.org/10.1016/j.coesh.2021.100253

[2] Mitterecker J, Košević M, Stopic S, Friedrich B, Panić V, Stevanović J, Mihailović M. Electrochemical Investigation of Lateritic Ore Leaching Solutions for Ni and Co Ions Extraction. *Metals (Basel).* 2022; 12(2): 325 https://doi.org/10.3390/met12020325

[3] Hu X, Ma B, He F, Chen Y, Wang C. Mineralogical characterization of low-grade nickel laterites from the North Oman Mountains: Using mineral liberation analyses - scanning electron microscopy-based automated quantitative mineralogy. *Ore Geol Rev.* 2020; 120: 103429. https://doi.org/10.1016/j.oregeorev.2020.103429

[4] Zevgolis EN, Daskalakis KA. The Nickel Production Methods from Laterites and the Greek Ferronickel Production among Them.

Mater Proc. 2021; *5*(1): 104. https://doi.org/10.3390/materproc2021005104.

[5] Pintowantoro S, Widyartha AB, Setiyorini Y, Abdul F. Sodium Thiosulfate and Natural Sulfur: Novel Potential Additives for Selective Reduction of Limonitic Laterite Ore. *J Sustain Metall* .2021; 7(2): 481-494. doi: 10.1007/s40831-021-00352-4.

[6] Moats MS, Davenport WG: Chapter 2.3 Nickel and Cobalt, In *Treatise on Process Metallurgy*. 2nd ed. Elsevier; 2024: 575-604. https://doi.org/10.1016/B978-0-323-85373-6.00030-2.

[7] Caron MH. Fundamental and practical factors in ammonia leaching of nickel and cobalt ores. *JOM.* 1950; *2*(1): 67-90. https://doi.org/10.1007/BF03398981.

[8] Caron MH. "Separation of Nickel and Cobalt" *JOM.* 1950; 2(1): 91-103. https://doi.org/10.1007/BF03398982.

[9] Kießling F, Stopic S, Gürmen S, Friedrich B. Recovery of Diamond and Cobalt Powders from Polycrystalline Drawing Die Blanks via Ultrasound Assisted Leaching Process—Part 2: Kinetics and Mechanisms. *Metals (Basel)* 2020; 10(6): 741. https://doi.org/10.3390/met10060741.

[10] Rodriguez R. Reduction in energy cost in Cuban Caron Process Plants. In: *International Laterite Nickel Symposium 2004 (as held during the 2004 TMS Annual Meeting)*. The Minerals, Metals & Materials Society 2004, pp. 657-664. ISBN: 0-87339-550-6.

[11] Caetano GC, Ostroski IC, de Barros MASD. Lateritic Nickel and Cobalt Recovery Routes: Strategic Technologies. *Miner Process Extr Metall Rev.* 2024; 400-414. https://doi.org/10.1080/08827508.2024.2328696.

[12] Canterford Jh. Oxide Ores of Nickel — The Australian Situation. *Miner Process Extr Metall Rev.* 1983; 1(1-2): 85-109. https://doi.org/10.1080/08827508308952590.

[13] Coello-Velázquez AL, Quijano Arteaga V, Menéndez-Aguado JM, Pole FM, Llorente L. Use of the Swebrec Function to Model Particle Size Distribution in an Industrial-Scale Ni-Co Ore Grinding Circuit. *Metals (Basel).* 2019; 9(8): 882. https://doi.org/10.3390/met9080882.

[14] De Graaf JE. The treatment of lateritic nickel ores — a further study of the caron process and other possible improvements. Part I. Effect of reduction conditions. *Hydrometallurgy* 1979; 5(1): 47-65. https://doi.org/10.1016/0304-386X(79)90027-6.

[15] Mano ES., Caner L., Petit S., Chaves AP., Mexias, A. S. Ni-smectitic ore behaviour during the Caron process. *Hydrometallurgy.* 2019; 186: 200-209. https://doi.org/10.1016/j.hydromet.2019.04.010.

[16] Angulo Palma HJ, Legrá AL, Urgellés AL, Gálvez E, Castillo J. Post-combustion Effect on Nickel and Cobalt Extractions from the Caron Process. *In: Bindhu V, Tavares JM, Ţălu Ş, eds.* Proceedings of Fourth International Conference on Inventive Material Science Applications. *Springer, Singapore* 2022; 515-527. https://doi.org/10.1007/978-981-16-4321-7_43.

[17] Ramírez Pérez IM, Ramírez Serrano B. Efecto de la postcombustión sobre los principales índices técnico-económicos en un horno Herreshoff para la producción de níquel. Post-combustion effect on the main technical-economic indices in the Herreshoff furnace for nickel production. *Min Geol.* 2021; 37(4): 426-444. (Spanish).

[18] Angulo Palma HJ, Terencio Guevara PL, Legrá AL, Videaux Arcia L. Análisis especiales en un horno de reducción de níquel a escala de Planta Piloto. Special Analysis in a Nickel Reduction Furnace at Pilot Plant scale. *RTQ.* 2017; 37(3): 484-499. (Spanish).

[19] Pickles CA, Anthony W. A Thermodynamic Study of the Reduction of a Limonitic Laterite Ore by Methane. *High Temp Mater Proc.* 2018; 37(9-10): 909-919. https://doi.org/10.1515/htmp-2017-0106.

[20] Pickles CA, Anthony W. Thermodynamic modelling of the reduction of a saprolitic laterite ore by methane. *Miner Eng.* 2018; 120: 47-59. https://doi.org/10.1016/j.mineng.2018.02.006.

[21] Ilyas S, Kim H, Srivastava RR. Carbothermic Reduction Roasting of a Low-Grade Nickel Laterite Ore in the Modified Caron Process. *In: C. Anderson et al., eds*. The 5th International Symposium on Nickel and Cobalt. Switzerland: Springer Nature; 2021: 317-328. https://doi.org/10.1007/978-3-030-65647-8_27.

[22] Ilyas S, Srivastava RR, Kim H, Ilyas N, Sattar R. Extraction of nickel and cobalt from a laterite ore using the carbothermic reduction roasting-ammoniacal leaching process. *Sep Purif Technol.* 2020; 232: 115971. https://doi.org/10.1016/j.seppur.2019.115971.

[23] Angulo Palma HJ, Legrá AL, Hernández Pedrera C, Lamorú Urgellés A, Vega Cala RJ. Efecto de la sustitución del petróleo aditivo por carbón bituminoso en el proceso de reducción de lateritas. Effect Substit Addit Oil with Bitum Coal Process Reducing Laterites. *RTQ.* 2018; 38: 750-764. (Spanish).

[24] De Alvarenga Oliveira V, dos Santos CG, de Albuquerque Brocchi E. Assessing the Influence of NaCl on the Reduction of a Siliceous Laterite Nickel Ore Under Caron Process Conditions. *Metall Mater Trans B.* 2019; 50(3): 1309-1321. https://doi.org/https://doi.org/10.1007/s11663-019-01552-w.

[25] Angulo Palma HJ, Legrá AL, Hernández Pdrera C, Lamorú Urgellés A, Toro Villarroel N. Reducción de menas lateríticas utilizando como aditivo mezclas de carbón bituminoso y petróleo. Reduction of lateritic minerals using additive mixtures of bituminous coal and oil. *RTQ.* 2020; 40: 93-105. (Spanish).

[26] Angulo Palma HJ., Legrá AL., Lamorú Urgellés A., Hernández Pedrera C., Gallegos S., Galleguillos Madrid FM., Toro Villarroel, N. Use of a mixture of coal and oil as an additive for selective reduction of lateritic ore by the Caron process: *Hem Ind.* 2024; 78: 17-27. https://doi.org/10.2298/HEMIND230118017A.

[27] Sant B. Chemical reaction engineering. *Talanta.* 1968; 15(12): 1483-1486. https://doi.org/10.1016/0039-9140(68)80211-5.

[28] Levenspiel O. Chemical Reaction Engineering. 3rd ed., New York, NY: John Wiley & Sons; 1999. ISBN 0-471-25424-X.

[29] Li B., Ding Z., Wei Y., Wang H., Yang Y., Barati M. Kinetics of reduction of low-grade nickel laterite ore using carbon monoxide. *Metall Mater Trans B.* 2018; 49: 3067-3073. https://doi.org/10.1007/s11663-018-1367-8.

[30] Cabrera G, Gómez JM, Hernández I, Coto O, Cantero D. Different strategies for recovering metals from CARON process residue. *J Hazard Mater.* 2011; 189(3): 836-42. https://doi.org/10.1016/j.jhazmat.2011.03.048.

[31] Rhamdhani MA, Chen J., Hidayat T, Jak E., Hayes P. Advances in research on nickel production through the Caron process. In: Harre J, ed. Proceedings of European Metallurgical Conference 2009. Germany: GDMB; 2009: 899-914. ISBN 978-3-940276-19-3.

[32] Rhamdhani MA, Hayes PC, Jak E. Nickel laterite Part 1-microstructure and phase characterisations during reduction roasting and leaching. *Miner Process Extr.* 2009; 118: 129-145. https://doi.org/10.1179/174328509X431391.

[33] Rhamdhani MA, Hayes PC, Jak E. Nickel laterite Part 2-thermodynamic analysis of phase transformations occurring during reduction roasting. *Miner Process Extr*. 2009; 118: 146-155. https://doi.org/10.1179/174328509X431409.

[34] Valix M, Cheung W. Effect of sulfur on the mineral phases of laterite ores at high temperature reduction. *Miner Eng.* 2002; 15(7): 523-530. https://doi.org/10.1016/S0892-6875(02)00069-9.

[35] Valix M, Cheung WH. Study of phase transformation of laterite ores at high temperature. *Miner Eng.* 2002; 15(8): 607-612. https://doi.org/10.1016/S0892-6875(02)00068-7.

[36] Shoubao L, Eng B, Eng M. Study of nickeliferrous laterite reduction. A Thesis Submitted to the School of Graduate Studies in Partial Fulfilment of the Requirements for the Degree of Master Engineering, University of Science and Technology, Beijing; 1999.https://translate.google.com/?sl=en&tl=es&text=Study%20of%20nickeliferrous%20laterite%20reduction&op=translate.

[37] Castellanos Suárez J. Cinética de la reducción de los minerales oxidados de níquel en Cuba. Kinetics of the reduction of oxidized nickel minerals in Cuba. *Min Geol.* 1984; *2*: 197-222. (Spanish).

[38] Shofi A, Supriyatna Y, Prasetyo AB. Selective Reduction of Southeast Sulawesi Nickel Laterite using Palm Kernel Shell Charcoal: Kinetic Studies with Addition of Na2SO4 and NaCl as Additives. *Bull Chem React Eng Catal.* 2020; *15*(2), 501-513. https://doi.org/10.9767/bcrec.15.2.7733.501-513.

Kinetika procesa pečenja/selektivne redukcije uz upotrebu mešavine bitumenskog uglja i lož ulja kao aditiva

Hugo Javier Angulo-Palma[1,2], Manuel Saldana[3,4], Ángel Legrá Legrá[1], Alisa Lamorú Urgellés[1], Carlos Hernández Pedrera[5], Sandra Gallegos[3], Felipe M. Galleguillos Madrid[6] and Norman Toro[3]

[1]*Centro de Investigaciones del Níquel ``Alberto Fernández Montes de Oca´´ (CEDINIQ), Moa, Holguín, Cuba*
[2]*Departamento de Metalurgia Química, Universidad de Moa, Holguín, Cuba*
[3]*Faculty of Engineering and Architecture, Universidad Arturo Prat, Iquique, Chile*
[4]*Departamento de Ingeniería Química y Procesos de Minerales, Universidad de Antofagasta, Antofagasta, Chile*
[5]*Facultad de Ingeniería Química y Agronomía, Universidad de Oriente, Santiago de Cuba, Cuba*
[6]*Centro de Desarrollo Energético Antofagasta, Universidad de Antofagasta, Antofagasta, Chile*

(Stručni rad)

Izvod

Lateritna ruda je trenutno glavna sirovina koja omogućava ekstrakciju nikla Caron procesom. Do danas, kinetičko ponašanje procesa pečenja/selektivne redukcije lateritnih ruda nikla u pilot postrojenju je nedovoljno istraženo. U ovoj studiji, kinetičko ponašanje, faza koja kontroliše i mehanizmi koji opisuju ovaj proces primenom mešavine 2,00 mas.% bitumenskog uglja i 1,25 mas.% mazuta kao redukcionog aditiva određivani su tokom evaluacije visokog i niskog toplotnog profila. Faze redukovanih/izluženih minerala i polazne rude analizirane su rendgenskom difrakcijom praha. Pokazano je da smeša koja se koristi kao redukcioni aditiv garantuje adekvatnu transformaciju u oba termička profila; odnos između zaostalog nikla i vremena zadržavanja je opisan reakcijom prvog reda sa koeficijentima determinacije većim od 0,949. Iako nije analiziran uticaj vazduha posle sagorevanja, faza koja kontroliše proces je bila difuzija kroz sloj pepela sa energijom aktivacije od 14,4060 kJ mol^{-1}. Dakle, najpreciznija kombinacija za opisivanje procesa je difuzija kroz sloj pepela i rast jezgara.

Ključne reči: kinetika i mehanizmi reakcije; rad peći; pirometalurgija; lateritna ruda nikla; Caron proces

Application of response surface methodology to optimize the treatment process of high conversion of free fatty acids using (1R)-(-)-camphor-10--sulfonic acid and iron(III) sulphate

Adeeb Hayyan[1,2], Khalid M. Abed[1,3], Mohammed A. Al-Saadi[4], Amal A. M. Elgharbawy[5,6], Yousef Mohammed Alanazi[7], Jehad Saleh[7], Nur Hanie Mohd Latiff[8], Sharifah Shahira Syed Putra[9], Mohd Roslan Mohd Nor[10] and Shareef Fadhil Mahel Alhashemi[11]

[1]*Department of Chemical Engineering, Faculty of Engineering, Universiti Malaya, Kuala Lumpur, Malaysia*
[2]*Sustainable Process Engineering Centre (SPEC), Faculty of Engineering, Universiti Malaya, Kuala Lumpur, Malaysia*
[3]*Department of Chemical Engineering, College of Engineering, University of Baghdad, Baghdad, Iraq*
[4]*National Chair of Materials Science and Metallurgy, University of Nizwa, Nizwa, Oman*
[5]*International Institute for Halal Research and Training (INHART), International Islamic University Malaysia, Kuala Lumpur, Malaysia*
[6]*Bioenvironmental Engineering Research Centre (BERC), Department of Biotechnology Engineering, Faculty of Engineering, International Islamic University Malaysia (IIUM), Kuala Lumpur, Malaysia*
[7]*Department of Chemical Engineering, College of Engineering, King Saud University, Riyadh, Saudi Arabia*
[8]*Global Centre for Environmental Remediation (GCER), College of Engineering, Science, and Environment (CESE), University of Newcastle, Callaghan, Australia*
[9]*Faculty of Industrial Sciences and Technology, Universiti Malaysia Pahang Al-sultan Abdullah, Lebuhraya Tun Abdul Razak, 26300 Gambang, Pahang, Malaysia*
[10]*Halal Research Group, Academy of Islamic Studies, Universiti Malaya, Kuala Lumpur, Malaysia*
[11]*Department of Chemistry, College of Science, Sultan Qaboos University, Muscat, Oman*

ORIGINAL SCIENTIFIC PAPER

UDC: 665.75:622.276.32

Hem. Ind. **79(2)** 79-92 (2025)

Abstract

This study investigates biodiesel production from acidic crude palm oil using one homogeneous catalyst, (1R)-(-)-camphor-10-sulfonic acid (10-CSA), and one heterogeneous catalyst, iron(III) sulphate, focusing on their catalytic activity, recyclability, and process optimisation by using response surface methodology. Optimal conditions were identified by utilising a Box-Behnken factorial design. For 10-CSA, the optimised conditions yielded a free fatty acid (FFA) reduction to 0.43 wt.%, with a catalyst dosage of 1.5 wt.% (investigated range: 1.0-2.0 wt.%), methanol-to-oil molar ratio of 12.67:1 (investigated range: 10 to 14:1), reaction temperature of 59.6 °C (investigated range: 50 to 65 °C), and reaction time of 33.1 min (investigated range: 30 to 40 min). For iron(III) sulphate, the optimised conditions led to FFA reduction to 1.04 wt.%, with a catalyst dosage of 3.14 wt.% (investigated range: 2.5 to 3.5 wt.%), methanol-to-oil molar ratio of 12:1 (investigated range: 10 to 14:1), reaction temperature of 60 °C (investigated range: 55 to 70 °C), and reaction time of 178.6 min (investigated range: 150 to 180 min). Results of the ANOVA analysis confirmed the significance of key factors for both catalysts ($p < 0.05$), with R^2 values of 0.937 for 10-CSA and 0.916 for iron(III) sulphate, indicating strong model fits. The mean relative percent deviation (MRPD) was <5 % for both models, demonstrating high predictive accuracy. The lack of fit was found to be insignificant ($p > 0.05$), confirming the adequacy of the models. Both catalysts achieved high FFA conversions of 95.2 % for 10-CSA and 88.2 % for iron(III) sulphate, which meets the EN 14214 and ASTM D6751 standards. Notably, 10-CSA exhibited superior catalytic activity and recyclability, highlighting its potential for industrial-scale biodiesel production. This study offers practical insights into optimising esterification processes for biodiesel production from acidic crude palm oil.

Keywords: Acidic crude palm oil; biodiesel; esterification; homogeneous acid catalyst; heterogeneous acidic catalyst.

Available on-line at the Journal web address: http://www.ache.org.rs/HI/

Corresponding authors: Adeeb Hayyan, Department of Chemical Engineering, Faculty of Engineering, University Malaya, Kuala Lumpur 50603, Malaysia; E-mail: adeeb.hayyan@yahoo.com
Amal A. M. Elgharbawy, International Institute for Halal Research and Training (INHART), International Islamic University Malaysia, P.O Box 10, 50728 Kuala Lumpur, Malaysia; E-mail: amalgh@iium.edu.my

Paper received: 15 May 2024; Paper accepted: 17 Mach 2025; Paper published: 7 May 2025.
https://doi.org/10.2298/HEMIND240515003H

1. INTRODUCTION

Biodiesel has a superior emission profile compared to diesel, substantially reducing emissions of unburned hydrocarbons, carbon monoxide, sulphates, polycyclic aromatic hydrocarbons, nitrated polycyclic aromatic hydrocarbons, and particulate matter [1-5]. As a result of the limited annual production of crude palm oil and the increasing global market demand, the priority of crude palm oil usage has been given to palm oil refineries for food processing. Acidic crude palm oil (ACPO), produced in palm oil mills, is considered a less favourable variant of crude palm oil due to its association with various operational and processing factors, such as milling inefficiencies, prolonged storage durations, and the effects of climate change [6]. Acidic oil with high free fatty acid (FFA) content has to be submitted to a pretreatment step to remove the FFA before refinery processing or biodiesel production [4,6-11]. Many types of heterogeneous acid catalysts have been used in biodiesel production, such as ferric sulphate and sulphated zirconia [12,13]. In addition, lipases were used as biocatalysts in esterification and transesterification of acidic oils or fats to produce biodiesel [14-16]. However, immobilisation is required to ensure long stability and efficiency of lipases. Homogeneous acid catalysts play a crucial role in biodiesel production, participating in the transesterification process. Thus, these catalysts have been extensively studied due to their effectiveness in facilitating conversion of triglycerides into fatty acid methyl esters. In addition to acidic, alkaline catalysts have also been explored for their potential in biodiesel production [17]. However, different challenges have also been recognised associated with the use of homogeneous catalysts. For instance, the presence of high amounts of FFAs in biodiesel feedstock can lead to issues such as the formation of water and soap, as well as separation problems when using alkaline catalysts, indicating the need for exploration of alternatives to address these limitations [18]. Therefore, research has been directed towards the development and evaluation of novel catalysts for biodiesel production [19]. Recently, ionic liquids and deep eutectic solvents were applied to esterify FFA in acidic oils [20-23]. Among different substances, (1R)-(-)--camphor-10-sulfonic acid (10-CSA) and iron(III) sulphate ($Fe_2(SO_4)_3$) have shown potential to be used in the biodiesel industry due to their catalytic activity and the appearance in solid powder form under normal conditions. 10-CSA has been studied for its catalytic properties in various organic reactions [24] as well as in the synthesis of different materials for potential applications in coatings and composites [25]. Furthermore, the chiral nature of 10-CSA has been explored, highlighting its potential for use in enantioselective processes, which could be beneficial in the production of specific biodiesel compounds [26].

On the other hand, $Fe_2(SO_4)_3$ has been investigated for its role in coagulation processes for the removal of pollutants from water, demonstrating its effectiveness in treating wastewater [27]. Potentials of 10-CSA and $Fe_2(SO_4)_3$ for utilisation in the biodiesel industry are further supported by applications of these compounds in polymerisation processes and their use as calibration standards in spectroscopic techniques [28,29]. These diverse applications demonstrate the multifaceted nature of these compounds and their potential for various processes involved in biodiesel production. Thus, catalytic properties, environmental interactions, and diverse applications in organic synthesis and industrial processes make 10-CSA and $Fe_2(SO_4)_3$ attractive for further investigations.

Hence, this study aims to optimise and compare the catalytic activity of a homogeneous acid catalyst (10-CSA) and a heterogeneous acidic catalyst ($Fe_2(SO_4)_3$) for esterification of ACPO and biodiesel production using a Box-Behnken factorial design. The aim was to perform a novel comparative analysis to provide insights into the performance of these catalysts under similar reaction conditions. The design explores the effects of catalyst dosage, methanol-to-oil molar ratio, reaction temperature, and reaction time on biodiesel outcomes. By optimising these factors, the study seeks to develop efficient biodiesel production methods that meet the EN 14214 and ASTM D6751 standards, addressing challenges posed by ACPO and guiding industrial-scale biodiesel production from lower-quality feedstock. This study's findings are intended to primarily aid the transportation sector by providing a renewable alternative to conventional diesel fuel, particularly for vehicle fuel, marine transport, as well as agricultural and construction equipment.

2. MATERIALS AND METHODS

2. 1. Chemicals and materials

Acidic crude palm oil (ACPO) was obtained from a local palm oil mill in Selangor Darul Ehsan, Malaysia. Laboratory-grade methanol 99.8 % was purchased from Merck (Malaysia). Iron(III) sulphate ($Fe_2(SO_4)_3$) (reagent grade 97 %) was purchased from R&M Chemicals (Malaysia). (1R)-(-)-camphor-10-sulfonic acid (10-CSA) (ACS grade 99 %) was purchased from Merck (Malaysia).

2. 2. Esterification (production of biodiesel from acidic crude palm oil)

The arbitrary amount of ACPO was first heated in an oven at 70 °C. The reactor system was maintained at the desired temperature by adjusting the temperature of the circulating water bath. Next, 30 g of ACPO was measured and poured into a multi-unit batch reactor, with each unit having a 1 dm^3 volume. Mechanical stirring was used to ensure homogeneity, while atmospheric pressure was maintained by an automated control system. In specific, all experiments were carried out in a laboratory scale batch multi-unit reactor system with methanol reflux, with a jacketed vessel connected to a circulating bath. The reaction temperature and stirring speed were monitored by uniquely designed feedback controllers. The catalyst was mixed with methanol before being added to the reactor. When using 10-CSA as the catalyst, the catalyst dosage ranged from 0.25 to 2.25 wt.%, while the methanol-to-oil molar ratio varied from 2 to 14, requiring 2.17 to 15.18 g of methanol. When using iron(III) sulphate, the catalyst dosage ranged from 2 to 6 wt.%, while the methanol-to-oil molar ratio ranged from 8 to 12, requiring 8.68 to 13.02 g of methanol. The reactor was then connected to a reflux condenser and magnetic stirring was adjusted to 450 rpm. At the same time, the reaction time was recorded using a stopwatch. After each experimental run (Supplementary material, Tables S1 and S2), the product was left to settle by gravity and the excess methanol was evaporated in the oven. The FFA content of the treated ACPO was determined and reported for each experiment. The optimal conditions for ACPO esterification were verified by repeating three validation experiments. The last section of this study was characterisation of the produced biodiesel. The biodiesel quality was checked for its compliance with specifications in the EN 14214 and ASTM D6751 standards for biodiesel. The FFA content of ACPO was determined based on the American Oil Chemist's Society (AOCS) official method Ca 5a-40 commercial fats and oils [19,30]. The ester content, mono, di and triacylglycerols, and free and total glycerol contents were determined using a gas chromatography flame ionisation detector (GC/FID) (Perkin Elmer Clarus 500, Netherlands).To measure the methyl ester (biodiesel) content in the sample, different concentrations of the diluted standard (FAME C14-C18) mixed with *n*-hexane were injected into the GC column respectively using splitless mode injector with a capillary column (SP 2330 polar column ID: 0.32mm). Helium was used as a carrier gas at a flow rate of 1 cm^3 min^{-1}, and each sample run time was approximately 40 min, starting at 50 °C for about 1 min and subsequently increased to 220 °C at 2 °C min^{-1} and held at this temperature for 10 min. Approximately 1 µL of the sample was diluted with *n*-hexane before being injected into the GC. The weights of biodiesel produced were determined by comparing them to the sample of pure standards [31]. The yield, % of biodiesel was calculated by following Equation (1):

$$\text{Yield} = (\text{Total weight of biodiesel}/\text{Total weight of oil in the sample})\times 100 \quad (1)$$

2. 3. Optimisation method

Response surface methodology (RSM) was employed to determine optimal operating conditions for ACPO esterification performed with the use of the investigated homogeneous and heterogeneous catalysts. A Box-Behnken factorial design with four factors and three levels was selected for this study, comprising 29 factorial points and five centre points to enhance robustness. The four factors were catalyst dosage, methanol-to-oil molar ratio, reaction temperature, and reaction time. Table 1 presents the specific values for these factors when 10-CSA was used as the homogeneous catalyst, while Table 2 provides the same information for the heterogeneous catalyst ($Fe_2(SO_4)_3$).

Table 1. *Experimental range and levels of the factors for (1R)-(-)-camphor-10-sulfonic acid*

Factor	Symbols	Range and levels		
		-1	0	1
Catalyst dosage, wt.%	*A*	0.25	1.25	2.25
Methanol-to-oil molar ratio	*B*	2	8	14
Reaction temperature, °C	*C*	40	60	80
Reaction time, min	*D*	10	30	50

Table 2. *Experimental range and levels of the factors for iron (III) sulphate*

Factor	Symbols	Range and levels		
		-1	0	1
Catalyst dosage, wt.%	*A*	2	4	6
Methanol-to-oil molar ratio	*B*	8	10	12
Reaction temperature, °C	*C*	60	70	80
Reaction time, min	*D*	100	150	200

A second-order response surface was derived to describe the esterification process with general Equation (2):

$$F = \alpha_0 + \alpha_1 A + \alpha_2 B + \alpha_3 C + \alpha_4 D + \alpha_{12} AB + \alpha_{13} AC + \alpha_{14} AD + \alpha_{23} BC + \alpha_{24} BD + \alpha_{34} CD + \alpha_{11} A^2 + \alpha_{22} B^2 + \alpha_{33} C^2 + \alpha_{44} D^2 \quad (2)$$

where, F / wt.% represents the FFA content of the treated ACPO, whereas, for $Fe_2(SO_4)_3$, the objective function was transformed to represent ln the FFA content (ln F).

The transformation was used to achieve a more significant model fit. In this model, α_0 is the intercept term, α_1, α_2, α_3, and α_4 are linear coefficients, α_{12}, α_{13}, α_{14}, α_{23}, α_{24}, and α_{34} are interactive coefficients, α_{11}, α_{22}, α_{33}, and α_{44} are quadratic coefficients, and *A, B, C,* and *D* represent the actual factors, which are catalyst dosage, methanol-to-oil molar ratio, reaction temperature, and reaction time, respectively. Experimental data analysis and response surface plotting were conducted using Design-Expert software (version 12.0.3.3, Stat-Ease Inc., MN) [31,32]. Table S1 (Supplementary material) provides the Box-Behnken design used for optimising 10-CSA-catalyzed esterification, while Table S2 (Supplementary material) presents the design for optimising ($Fe_2(SO_4)_3$)-catalysed esterification.

3. RESULTS AND DISCUSSION

3. 1. Optimization of the process using (1R)-(-)-camphor-10-sulfonic acid

Optimisation of biodiesel production using (1R)-(-)-camphor-10-sulfonic acid was performed by investigating the effects of catalyst dosage, methanol-to-oil molar ratio, reaction temperature, and reaction time on FFA reduction and conversion efficiency. Furthermore, the first step in analysing the results involved creating a predictive model using response surface methdology (RSM) with the Box-Behnken factorial design. This design allows for the systematic evaluation of the key factors affecting esterification, stated above. A quadratic regression model for 10-CSA was derived from the experimental data, and the following equation was obtained (Equation 3):

$$\begin{aligned}\ln F = {} & 0.3364 - 0.6454A - 0.5751B - 0.1076C - 0.3463D - 0.5016AB + 0.0275AC - 0.2036AD - 0.0410BC - \\ & - 0.1488BD - 0.0154CD + 0.2870A^2 + 0.2208B^2 + 0.2843C^2 + 0.1707D^2 \end{aligned} \quad (3)$$

Results of the ANOVA analysis for the response surface quadratic model for 10-CSA is presented in Table 3. The RSM application yielded a statistically significant quadratic model for optimising FFA conversion (*F*-value = 46.67, $p < 0.0001$), with only a 0.01 % probability that the observed variance could arise from noise. The model's high adjusted R^2 (0.918) and predicted R^2 (0.877) values demonstrated excellent agreement, confirming its strength in predicting FFA conversion within the experimental design space. Moreover, the model's strong signal-to-noise ratio (adequate precision = 25.442) validated its utility for process optimisation.

Catalyst dosage (*A*) and methanol-to-oil molar ratio (*B*) emerged as the most influential factors, with exceptionally high *F*-values of 254.15 and 201.79, respectively ($p < 0.0001$). Reaction time (*D*) also exhibited a significant impact ($F = 73.14$, $p < 0.0001$), while reaction temperature (*C*) showed moderate significance (*F*-value = 7.06, $p = 0.0110$). Quadratic terms for all factors (A^2, B^2, C^2, D^2; $p < 0.01$) further highlighted nonlinear relationships between the variables and FFA conversion, suggesting the presence of optimal operating conditions beyond which the response plateaus or declines.

Significant interactions were observed between the catalyst dosage and methanol-to-oil ratio (*AB*; *F*-value = 51.17, $p < 0.0001$), catalyst dosage and reaction time (*AD*; *F*-value = 8.43, $p = 0.0058$), and methanol-to-oil ratio and reaction time (*BD*; *F*-value = 4.50, $p = 0.0397$). The strong *AB* interaction implies synergistic effects, where increasing both catalyst dosage and methanol-to-oil ratio enhances FFA conversion more than their individual contributions. Conversely, interactions involving temperature (*AC*, *BC*, *CD*) were statistically insignificant ($p > 0.05$), indicating negligible combined effects with other variables.

While higher catalyst dosages initially improve conversion rates, diminishing returns may occur at elevated levels due to potential saturation effects. Similarly, excessive methanol-to-oil ratios could dilute reactant concentrations or increase operational costs without proportional gains in FFA reduction.

While the methanol-to-oil ratio (*B*) is generally significant, the quadratic term for temperature (C^2, +0.2843) indicates that its effect becomes more pronounced near the reference point. This nonlinearity suggests that the temperature influence intensifies within specific operational ranges, potentially overshadowing the methanol-to-oil ratio (*B*) in localised regions of the design space. Thus, around the reference conditions, catalyst dosage (*A*) and temperature (*C*) may dominate due to curvature effects, even though the methanol-to-oil ratio (*B*) remains critical overall.

***Table 3.** ANOVA analysis for the response surface quadratic significant model for (1R)-(-)-camphor-10-sulfonic acid*

Source	Sum of squares	Degree of freedom	Mean square	*F*-value	*p*-value
Model	25.70	14	1.840	46.670	< 0.0001
A	10.00	1	10.00	254.150	< 0.0001
B	7.940	1	7.940	201.790	< 0.0001
C	0.278	1	0.277	7.060	0.0110
D	2.880	1	2.880	73.140	< 0.0001
AB	2.010	1	2.010	51.170	< 0.0001
AC	0.006	1	0.006	0.153	0.6972
AD	0.332	1	0.332	8.430	0.0058
BC	0.013	1	0.013	0.342	0.5618
BD	0.177	1	0.177	4.500	0.0397
CD	0.002	1	0.002	0.048	0.827
A^2	1.070	1	1.070	27.170	< 0.0001
B^2	0.633	1	0.633	16.080	0.0002
C^2	1.050	1	1.050	26.650	< 0.0001
D^2	0.378	1	0.378	9.610	0.003
Residual	1.690	43	0.039		
Pure error	0.016	33	0.001		

The perturbation plot (Figure S1) shows that the catalyst dosage (*A*) and methanol-to-oil molar ratio (*B*) have the strongest influence on FFA conversion during 10-CSA-catalysed esterification, as indicated by their steeper curves. Reaction temperature (*C*) and reaction time (*D*) have less impact, with flatter curves, highlighting the critical role of catalyst dosage and methanol-to-oil ratio in optimising FFA conversion.

From Figure S2, the diagnostic plots confirm the robustness of the quadratic model. The normal plot of residuals demonstrates that residuals align closely with a straight line, indicating adherence to a normal distribution. The residual *vs*. predicted plot exhibits a random scatter of points, suggesting homoscedasticity (constant variance) across the range of predicted values. The Box-Cox plot reveals that the current transformation parameter in the Box-Cox transformation, used to identify the most appropriate transformation of the response variable to stabilize variance and improve normality (λ) of 1 lies within the confidence interval for the optimal λ (0.57), implying that transformation of the response variable is not necessary [33]. Furthermore, the Cook's distance plot indicates that there are not influential outliers that significantly distort the model, as most data points exhibit low Cook's distances. Collectively, these diagnostics validate the model's assumptions of normality, constant variance, and absence of influential outliers, confirming its reliability for predicting FFA conversion [34].

The response surface plots (Fig. 1) elucidate the effects of key factors and their interactions on FFA reduction. At a constant reaction temperature of 60 °C and reaction time of 30 min, increasing both catalyst dosage and methanol-to-oil molar ratio significantly reduced the FFA content. This synergistic effect underscores the critical role of these factors in driving the esterification reaction. Higher methanol-to-oil ratios likely shift the reaction equilibrium toward ester formation, while increased catalyst dosages enhance reaction kinetics. Meanwhile**,** at a fixed methanol-to-oil molar ratio of 8:1 and reaction time of 30 min, the effect of reaction temperature was significant but less pronounced compared to the catalyst dosage. The lack of a significant interaction between the catalyst dosage and temperature suggests that temperature variations have a limited impact on FFA reduction within the studied range. Additionally**,** a constant methanol-to-oil molar ratio of 8:1 and reaction temperature of 60 °C, longer reaction times and higher catalyst dosages synergistically improved FFA reduction. This highlights the importance of optimising both parameters to maximise the conversion efficiency.

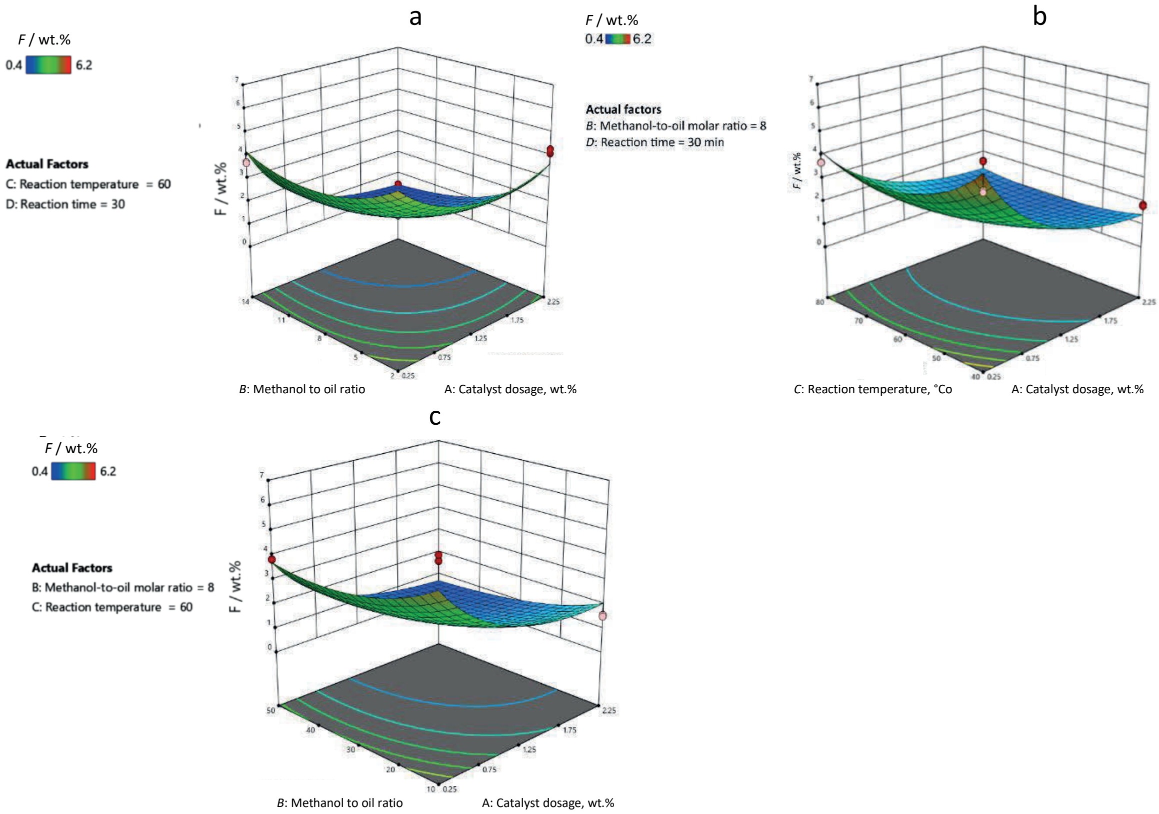

Figure 1. *3D response surface plots of the effect of 10-CSA on the FFA reduction as a function of: (a) catalyst dosage and methanol-to-oil molar ratio, (b) catalyst dosage and reaction temperature, (c) catalyst dosage and reaction time. The other factors were held at zero level.*

The contour plots (Fig. S3, Supplementary material) provide a clear visualisation of the response surface, enabling the identification of optimal operating conditions. For instance, the steep gradients in the contour lines confirm the strong influence of these factors on FFA reduction. Moreover, the relatively flat contour lines suggest that these factors have a more moderate impact, consistent with their lower F-values in the ANOVA analysis.

A set of constraints was applied to determine the optimal conditions for 10-CSA -catalysed esterification. Table S3 (Supplementary material) outlines the optimisation constraints, and Table S4 (Supplementary material) shows the resulting optimised solution. The optimal conditions for this process were a catalyst dosage of 1.5 wt.%, a methanol-to-oil molar ratio of 12.67:1, a reaction temperature of ~60 °C, and a reaction time of 33.11 min, resulting in an FFA content of 0.43 wt.% . These optimal conditions align with previous studies that emphasise the importance of catalyst dosage and methanol-to-oil molar ratio in driving esterification.

Several studies have investigated the impact of these parameters on FFA production and have identified optimal conditions. The significance of catalyst dosage and solvent effect in achieving high conversion and selectivity to FFA has been demonstrated by Jia *et al.* [35] realising 100 % conversion and 96.5 % selectivity to FFA at the optimal catalyst content and in methanol as a solvent. Furthermore, Xie *et al.* [36] highlighted the impact of catalyst dosage, methanol-to-oil molar ratio, and reaction temperature on FFA conversion to biodiesel. The study demonstrated that under specific operational conditions, including a methanol/oil molar ratio of 30:1, a catalyst dosage of 5 wt.%, a reaction temperature of 140 °C, and a reaction duration of 8 h, a high oil conversion of 92.2 % was achieved with total FFA transformation to biodiesel. The current study demonstrated good results at a lower conversion temperature, which is more suitable for industry.

Production of biodiesel from feedstock with high FFA contents often requires the use of solid catalysts to reduce FFA levels and ensure high biodiesel yields. Faruque *et al.* [37] utilised sulphated zirconia as a solid acid heterogeneous catalyst for biodiesel production from Neem oil, achieving a 95 % biodiesel yield while maintaining a 9:1 methanol-to-oil ratio. Solid acid catalysts have been preferred for high FFA esterification due to their insensitivity to the FFA content, elimination of the need for a biodiesel washing step, ease of catalyst separation, and lower product contamination levels. Additionally, solid acid catalysts are less corrosive, produce less waste, and are easier to separate from reactants and products, making them preferable over hazardous mineral acids for high FFA esterification [38]. Furthermore, the economic benefit of using solid catalysts in biodiesel production lies in their reusable nature for low-quality feedstock, leading to cheaper production costs [39]. The use of solid catalysts for biodiesel production has also been explored in the context of specific feedstock. For instance, efficient conversion of low-grade, nonedible oil feedstock into biodiesel was demonstrated using pumice as a bifunctional solid catalyst, which can catalyse the esterification of FFA and transesterification of fatty acid glycerides simultaneously [40]. This highlights the versatility of solid catalysts in enabling the conversion of diverse feedstocks into biodiesel.

3. 2. Optimisation of the process using iron(III) sulphate

Optimisation of biodiesel production using iron (III) sulphate was performed by evaluating the effects of (a) catalyst dosage, (b) methanol-to-oil molar ratio, (c) reaction temperature, and (d) reaction time on FFA reduction and conversion efficiency. A quadratic regression model for this process was derived in a similar manner as for that catalysed by 10-CSA, focusing on the key factors impacting esterification (Eq. 4):

$$\begin{aligned}\ln F = {} & -0.332888 + -0.645336A + -0.563832B + -0.110702C + -0.347448D + -0.485991AB + \\ & + 0.0219763AC + -0.209352AD + -0.0303575BC + -0.159192BD + -0.0119114CD + \\ & + 0.289957A^2 + 0.224655B^2 + 0.288779C^2 + 0.172073D^2\end{aligned} \tag{4}$$

The quadratic model (Table 4) developed for the second catalyst exhibited statistical significance (*F*-value = 45.71, $p < 0.0001$), with the catalyst dosage (*F*-value = 251.85, $p < 0.0001$) and methanol-to-oil molar ratio (*F*-value = 192.25, $p < 0.0001$) emerging as the dominant factors influencing FFA reduction.

Table 4. *ANOVA analysis for the response surface quadratic significant model for iron(III) sulphate*

Source	Sum of squares	Degree of freedom	Mean square	*F*-value	*p*-value
Model	25.390	14	1.810	45.71	< 0.0001
A	10.00	1	10.00	251.85	< 0.0001
B	7.630	1	7.630	192.25	< 0.0001
C	0.294	1	0.294	7.41	0.0093
D	2.900	1	2.900	73.00	< 0.0001
AB	1.890	1	1.890	47.61	< 0.0001
AC	0.004	1	0.004	0.097	0.7565
AD	0.351	1	0.351	8.83	0.0048
BC	0.007	1	0.007	0.186	0.6686
BD	0.203	1	0.203	5.11	0.0289
CD	0.001	1	0.001	0.029	0.8665
A^2	1.090	1	1.090	27.48	< 0.0001
B^2	0.655	1	0.655	16.50	0.0002
C^2	1.080	1	1.080	27.26	< 0.0001
D^2	0.384	1	0.384	9.68	0.0033
Residual	1.710	43	0.039		
Pure Error	0.007	33	0.0002		

Reaction time (*F*-value =73.00, $p < 0.0001$) and temperature (*F*-value = 7.41, $p = 0.0093$) also contributed significantly, albeit to a lesser extent. Synergistic interactions were observed between the catalyst dosage and methanol ratio (*AB*, $p < 0.0001$), catalyst dosage and reaction time (*AD*, $p=0.0048$), and methanol-to-oil molar ratio and reaction time (*BD*, $p = 0.0289$), highlighting the interconnected roles of these parameters in driving esterification efficiency. The significant quadratic terms (A^2, B^2, C^2, D^2; $p < 0.01$) confirmed nonlinear relationships, suggesting the existence of optimal operating conditions beyond which FFA reduction plateaus. Despite a significant lack of fit ($p < 0.0001$), the model demonstrated strong predictive capability, as evidenced by the high adjusted, $R^2 = 0.916$, and predicted, $R^2 = 0.874$, along with an exceptional signal-to-noise ratio (adequate precision is 25.045). The natural log transformation of the response variable ($\lambda = 1$) aligned with the Box-Cox recommendation $\lambda = 0.57$), validating the model's stability. These results underscore the catalyst's sensitivity to dosage and methanol-to-oil molar ratio, with temperature and time acting as secondary levers, and provide a reliable framework for optimising FFA conversion in industrial applications.

While temperature-related factors are generally significant, their local influence near the reference point is reduced due to the nonlinear response surface behaviour, where the effect plateaus, and the process becomes less sensitive to temperature variations within that narrow range.

The perturbation plot (Fig, S4, Supplementary material) for the $Fe_2(SO_4)_3$-catalysed esterification process illustrates the sensitivity of FFA content to changes in process factors at the reference point: catalyst dosage of 1.25 wt.%, methanol-to-oil molar ratio of 8:1, reaction temperature of 60 °C, and reaction time of 30 min. Increasing the catalyst dosage from the reference point significantly reduces the FFA percentage, highlighting its critical role in esterification efficiency. The methanol-to-oil molar ratio also influences FFA reduction but to a slightly lesser extent. Reaction temperature and reaction time exhibit flatter slopes, indicating minimal effects on FFA content within the studied range. Overall, for the $Fe_2(SO_4)_3$ catalyst, the catalyst dosage stands out as the most significant factor affecting esterification, followed by the methanol-to-oil molar ratio, as confirmed by their high F-values. While the perturbation plot shows minimal temperature influence near the reference point, Equation (4) and the ANOVA results (*F-value* = 7.41, $p = 0.0093$) indicate that temperature-related factors significantly affect FFA content across the broader experimental range. This suggests that the effect of temperature becomes more pronounced at conditions further from the reference point, likely due to nonlinear interactions captured by the quadratic term (C^2).

A normal plot of residuals was utilised to confirm the distribution of residuals associated with the esterification process facilitated by $Fe_2(SO_4)_3$ (Fig. S5, Supplementary material). This analytical step is crucial for affirming that the residuals follow a normal distribution, a key assumption for the validity of subsequent statistical analysis [41]. The graph demonstrated that the data points, signifying the externally studentised residuals, were in close proximity to the theoretical line that represents a normal distribution. Such proximity lends support to the normality premise for the statistical evaluations applied in our model. Notably, while a minor number of data points stray from this theoretical line, the magnitude of their divergence falls within permissible ranges and does not suggest any underlying issues with the model, like heteroscedasticity or nonlinear dynamics. These residuals are differentiated by FFA values, indicating the non-existence of a discernible connection between the magnitude of residuals and FFA concentrations. The absence of a discernible pattern reinforces the integrity of our statistical model, indicating that the projections made from the $Fe_2(SO_4)_3$-catalyzed esterification process stand on a firm statistical foundation suitable for drawing inferences. The 3D surface plots (Fig. 2) and contour plots (Fig. S6, Supplementary material) reveal significant interactions between key process variables affecting FFA reduction during the esterification process.

The catalyst dosage and methanol-to-oil molar ratio exhibit the most pronounced effects, with optimal FFA reduction achieved at higher catalyst dosages (1.5 to 2.25 wt.%) and methanol-to-oil molar ratios (10-14). Similarly, increasing both catalyst dosage and reaction time (40 to 50 min) leads to greater FFA reduction, while the reaction temperature (60 to 80 °C) has a moderate influence.

Based on these findings, the optimal conditions for maximising FFA reduction are identified as a catalyst dosage of 1.5 to 2.25 wt.%, methanol-to-oil molar ratio of 10-14, reaction temperature of 60 to 80 °C, and reaction time of 40 to 50 min. Operating within these ranges ensures efficient FFA conversion while minimising resource consumption.

Table S5 (Supplementary material) outlines the optimisation constraints and Table S6 (Supplementary material) shows the optimised solutions for $Fe_2(SO_4)_3$-based esterification, with a focus on the catalyst dosage, methanol-to-oil molar ratio, reaction temperature, reaction time, and the corresponding FFA content.

The best solution uses a catalyst dosage of 3.14 wt.%, a 12:1 methanol-to-oil molar ratio, a temperature of 60 °C, and a reaction time of 178.59 min. This setup results in an FFA content of 1.04 % with FFA conversion of 88.2 % with a desirability score of 0.77, indicating how well the solution aligns with the desired outcomes. The similar desirability scores across other solutions suggest that small changes in the catalyst dosage and reaction time can impact the final FFA content, with this particular combination showing a high level of optimisation. The data suggest that the catalyst dosage is a key factor in achieving effective esterification. Variations in this parameter can influence the balance between efficient FFA reduction and the risk of overusing the catalyst, which can increase costs or impact sustainability. The consistent desirability scores across multiple solutions point to the robustness of the optimisation process.

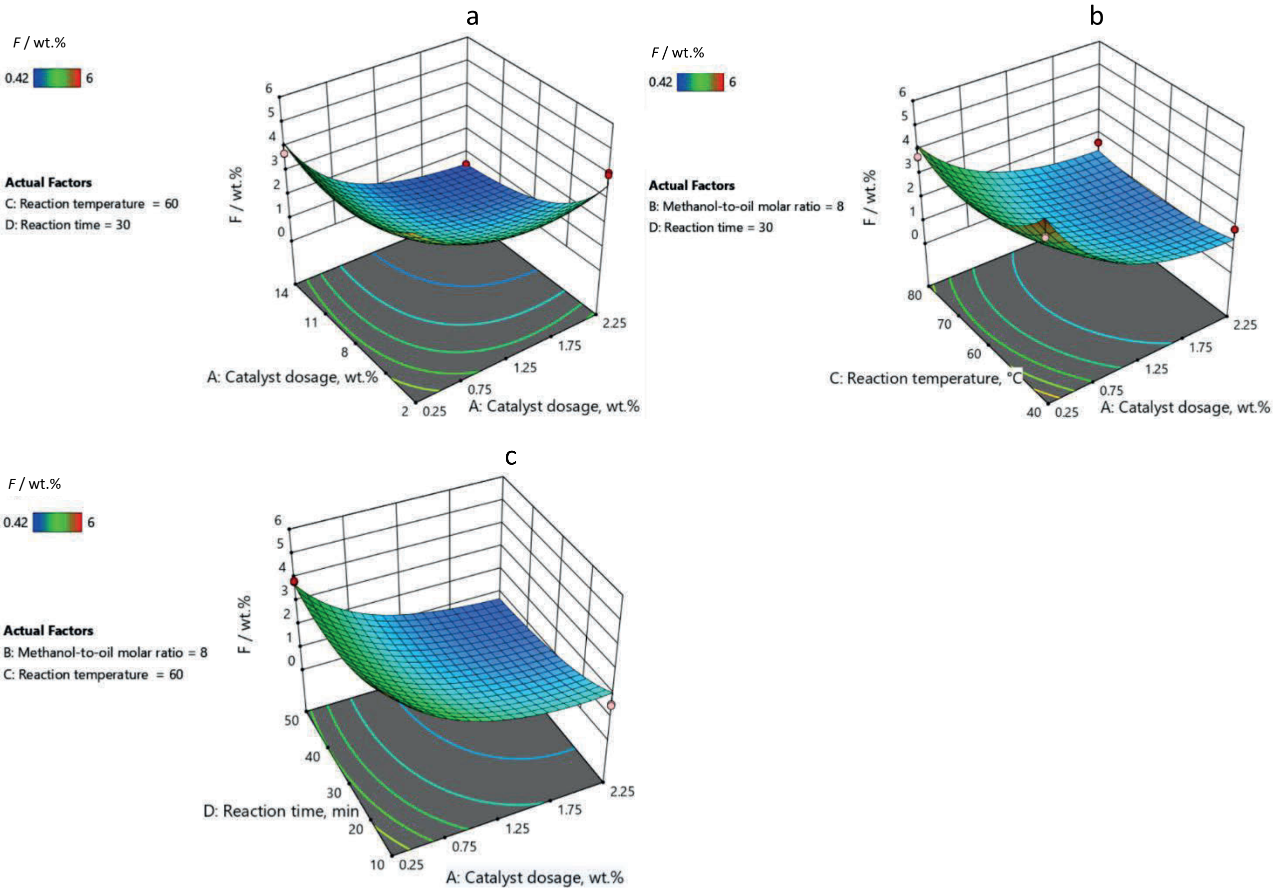

Figure 2. *3D response surface plots of the effect of Fe$_2$(SO$_4$)$_3$ on the FFA reduction as a function of: (a) catalyst dosage and methanol-to-oil molar ratio, (b) catalyst dosage and reaction temperature, (c) catalyst dosage and reaction time. The other factors were held at zero level*

3.3. Physicochemical properties of biodiesel produced from acidic crude palm oil

Table S7 (Supplementary material) outlines the specifications for biodiesel derived from ACPO with the use of Fe$_2$(SO$_4$)$_3$ as a catalyst, comparing the results with standards like EN 14214 and ASTM D6751. The biodiesel meets or exceeds the key industry requirements, including the ester content, monoacylglycerol content, diacylglycerol content, and total glycerol content under a catalyst dosage of 1.5 wt.%, a methanol-to-oil molar ratio of 12.67:1, a reaction temperature of 59.6 °C, and a reaction time of 33.1 min.

The biodiesel exhibited a molar ester percentage of 96.3 %, slightly below the EN 14214 minimum requirement of 96.5 %, but still indicative of high conversion efficiency. The contents of monoacylglycerols (0.05 wt.%), diacylglycerols (0.025 wt.%), and triacylglycerols (<0.01 wt.%) were significantly lower than the maximum limits set by EN 14214, indicating efficient transesterification. Both free glycerol (<0.01 wt.%) and total glycerol (0.050 wt.%) contents met the stringent limits of EN 14214 and ASTM D6751, reflecting high product purity. The water content (473 mg kg^{-1}) complied with both standards, ensuring good fuel stability. Metal contaminants, including potassium (1 mg kg^{-1}) and phosphorus (7.10 mg kg^{-1}), were well within permissible limits, minimising risks of engine deposits. The biodiesel density (86 kg m^{-3}), flash point (182 °C), and sulphated ash (<0.005 %) satisfied the respective EN and ASTM requirements, ensuring safe storage and combustion characteristics. Additionally, it exhibited a low total contamination (0.008 mg kg^{-1}) and achieved a Class 1 rating in the copper strip corrosion test, confirming excellent oxidative stability and corrosion resistance. Low levels of free glycerol and sulphated ash indicate a high level of purity in the final product. The water content, although close to the maximum limit, remains within acceptable boundaries, suggesting effective control of moisture during production.

The flashpoint, a critical safety measure, significantly exceeds the minimum requirements, indicating safe handling and storage. However, the cloud point of 16 °C could be a concern in colder climates, where biodiesel may solidify more readily than the conventional diesel. This could require additional measures or additives to ensure performance in diverse conditions. These findings suggest that the optimised conditions for $Fe_2(SO_4)_3$-based esterification yield a product that aligns with industry standards, indicating its potential for large-scale biodiesel production. However, further work may be needed to address the cloud point and other cold-weather properties for broader applicability.

Heterogeneous catalysis in biodiesel production was investigated in other studies reported in the literature. For example, Loryuenyong *et al.* [42] optimised the production of a heterogeneous $Fe_2(SO_4)_3$-calcium oxide/activated charcoal catalyst for biodiesel synthesis. Furthermore, the use of iron-based catalysts has been explored in the production of biodiesel from various feedstocks, such as waste cooking oils [43].

Several studies have investigated the optimal conditions for FFA reduction, providing valuable insights into the influence of catalyst dosage and reaction time on the esterification process. Betiku *et al.* [44] demonstrated the reduction of FFA content from ~28.8 to ~0.4 wt.% using a methanol/FFA molar ratio of 46:1, ferric sulphate dosage of 12 wt.%, and a reaction time of 75 min. Similarly, another study [45] has found that a 19.8:1 methanol-to-FFA molar ratio was effective only within an FFA range of 15 to 25 wt.%, whereas 5 wt.% sulphuric acid showed better performance, working effectively within the FFA range of 15 to 35 wt.%. Furthermore, an artificial neural network-genetic algorithm (ANN-GA) and RSM was utilised to establish the optimum reduction of FFA to 0.58 wt.% with a methanol/NSO molar ratio of 18.51, ferric sulphate dosage of 6 wt.%, and a reaction time of 62.8 min [46]. This emphasises the significance of considering both catalyst dosage and reaction time in tandem to achieve the desired FFA content.

These studies collectively emphasise the critical role of catalyst dosage and reaction time in FFA reduction during biodiesel production. By carefully optimising these parameters, it is possible to achieve significant reductions in the FFA content, ultimately contributing to the production of high-quality biodiesel.

3. 4. Recyclability of the catalysts

Table S8 (Supplementary material) illustrates recyclability of the catalysts used in the present study. The results suggest that homogeneous catalysts, such as 10-CSA, demonstrated higher catalytic activity during recycling runs compared to $Fe_2(SO_4)_3$. This observation suggests that homogeneous acids may be more suitable for industrial-scale biodiesel production due to their consistent catalytic activity and potential for reuse in multiple reaction cycles [47]. The difference in catalytic effectiveness between 10-CSA and $Fe_2(SO_4)_3$ can be attributed to the fundamental characteristics distinguishing homogeneous and heterogeneous catalysts. Homogeneous acid-based catalysts tend to distribute evenly throughout the reaction mixture, resulting in a broader reactive site. This trait likely accounts for their higher initial catalytic efficiency and better recyclability [48]. Conversely, heterogeneous acids may exhibit declining catalytic performance over time due to fouling, leaching, or structural changes [49]. Moreover, separating and purifying the biodiesel was challenging due to the presence of residual catalysts, unreacted methanol, and by-products, which made achieving high purity and process efficiency difficult, especially during recyclability studies.

Data from Table S8 (Supplementary material) indicate that the reduction in FFA content and conversion to FFA with 10-CSA is more consistent over multiple recycling runs compared to those achieved with $Fe_2(SO_4)_3$. FFA reduction with 10-CSA improves with each run, but the rate of FFA conversion from an initial high value tends to decrease over the recycling runs, possibly indicating a decrease in catalytic effectiveness. $Fe_2(SO_4)_3$ shows a more significant decline, suggesting its limitations in maintaining catalytic activity over repeated use [50]. These findings imply that homogeneous catalysts, like 10-CSA, could be better suited for large-scale biodiesel production due to their ability to retain catalytic activity over multiple uses, reducing the need for frequent catalyst replacement, thereby lowering production costs [51].

On the other hand, $Fe_2(SO_4)_3$ performance declines as the number of recycling runs increases, suggesting that it may not be ideal for industrial-scale production. This decrease could lead to increased expenses due to more frequent catalyst replacements or additional measures to rejuvenate the catalyst activity [52]. Given the obtained results, future research could focus on enhancing the recyclability of homogeneous catalysts to maintain high catalytic activity and stable FAME conversion rates over time. This might involve modifying the catalyst chemical structure to reduce degradation or developing methods to restore the catalyst effectiveness after repeated use. Studies might also examine the potential benefits of combining homogeneous and heterogeneous catalysts to capitalise on the strengths of each type, which could lead to a more efficient and sustainable biodiesel production process [43]. In summary, the obtained results suggest that homogeneous catalysts, particularly10-CSA, could be beneficial for improving the sustainability and efficiency of biodiesel production. Further research into catalyst optimisation and design could bolster robustness and scalability in this industry.

4. CONCLUSION

The ACPO esterification process using 10-CSA and $Fe_2(SO_4)_3$ as a homogenous and heterogeneous catalyst, respectively, was optimised by using RSM. The optimal conditions for 10-CSA were a catalyst dosage of 1.5 wt.%, a methanol-to-oil molar ratio of 12.67:1, a reaction temperature of 59.6 °C, and a reaction time of 33.1 min. These conditions reduced the FFA content to 0.41 wt.% and achieved a FFA conversion rate of 95.14 %. For $Fe_2(SO_4)_3$, the best conditions were a catalyst dosage of 3.14 wt.%, a methanol-to-oil molar ratio of 12:1, a reaction temperature of 60 °C, and a reaction time of 178.6 min, resulting in an FFA reduction to 0.99 wt.% and a FFA conversion of 95.2 % for 10-CSA and 88.2 % for iron(III) sulphate. These findings suggest that 10-CSA is the preferred homogeneous catalyst for large-scale biodiesel production due to several key benefits: its stable solid form, faster reaction times compared to $Fe_2(SO_4)_3$, and greater catalytic activity. Its ability to maintain performance over multiple use points to its cost-effectiveness and sustainability for industrial-scale operations. However, potential challenges encountered during the study include the difficulties in separating and purifying the final biodiesel product to ensure high purity and process efficiency. Therefore, future research should focus on improving separation and purification techniques in homogenous catalysis for biodiesel production. The present study primarily focused on optimising the biodiesel production process rather than catalyst separation. The findings highlight the key process parameters that enhance efficiency and yield, providing valuable insights for improving large-scale biodiesel production.

SUPPLEMENTARY MATERIAL

Additional data are available electronically at https://www.ache-pub.org.rs/index.php/HemInd/article/view/1343, or from the corresponding author on request.

Author contributions: *Adeeb Hayyan: Conceptualization, Supervision, Writing - original draft; Khalid M Abed: Writing - review & editing; Mohammed A. Al-Saadi: Investigation, Writing - original draft; Amal A. M. Elgharbawy: Data curation, Writing - review & editing; Yousef M. Alanazi: Funding acquisition; Jehad Saleh: Funding acquisition; Nur Hanie MohdLatiff: Writing - review & editing; Sharifah Shahira Syed Putra: Writing - review & editing; Mohd RoslanMohd Nor: Resources; Shareef Fadhil MahelAlhashemi: Funding acquisition, Resources.*

Acknowledgement: *This study was supported by the Project Number (RSP2025R511), King Saud University, Riyadh, Saudi Arabia.*

REFERENCES

[1] Sani YM, Daud WMAW, Abdul Aziz AR. Solid acid-catalyzed biodiesel production from microalgal oil - The dual advantage. *J Environ Chem Eng*. 2013; 1(3): 113-121. https://doi.org/10.1016/j.jece.2013.04.006

[2] Akpan IO, Edeh I, Uyigue L. A Review on Biodiesel Production. *Petrol Chem Ind Int*. 2023; 6(2): 131-141. https://doi.org/10.33140/PCII.

[3] Sakthivel R, Ramesh K, Purnachandran R, Mohamed Shameer P. A review on the properties, performance and emission aspects of the third generation biodiesels. *Renew Sustain Energy Rev*. 2018; 82: 2970-2992. https://doi.org/https://doi.org/10.1016/j.rser.2017.10.037

[4] Elgharbawy AS, Sadik WA, Sadek OM, Kasaby MA. Maximizing biodiesel production from high free fatty acids feedstocks through glycerolysis treatment. *Biomass Bioenergy*. 2021; 146: 105997. https://doi.org/10.1016/j.biombioe.2021.105997

[5] Wu Z, Cai J, Liu Z, Liang X, Yu S, Nie Y. Utilization of biodiesel and glycerol for the synthesis of epoxidized acyl glycerides and its application as a plasticizer. *J Am Oil Chem Soc*. 2023; 100: 733-741. https://doi.org/10.1002/aocs.12715

[6] Hayyan A, Mjalli FS, Hashim MA, Hayyan M, AlNashef IM, Al-Zahrani SM, Al-Saadi MA. Ethanesulfonic acid-based esterification of industrial acidic crude palm oil for biodiesel production. *Bioresour Technol*. 2011; 102(20): 9564-9570. https://doi.org/10.1016/j.biortech.2011.07.074

[7] Hayyan A, Hashim MA, Hayyan M. Agro-industrial acidic oil as a renewable feedstock for biodiesel production using (1R)-(-)-camphor-10-sulfonic acid. *Chem Eng Sci*. 2013; 16(6): 223-227. https://doi.org/10.1016/j.ces.2014.03.031

[8] Sun J, Zhu W, Mu B, Zhong J, Lin N, Chen S, Li Z. Efficient extraction of biodiesel feedstock and dehydration of kitchen waste: A method based on co-dissolution of liquefied dimethyl ether and water. *Waste Manag*. 2022; 147(1): 22-29. https://doi.org/10.1016/j.wasman.2022.04.044

[9] Singh B, Srivastava AK, Prakash O. A Comprehensive Review on Rare Biodiesel Feedstock Availability, Fatty Acid Composition, Physical Properties, Production, Engine Performance and Emission. *Process Integr Optim Sustain*. 2023; 7: 1081-1116. https://doi.org/10.1007/s41660-023-00343-w

[10] Hayyan A, Yeow ATH, Abed KM, Jeffrey Basirun W, Boon Kiat L, Saleh J, Wen Han G, Chia Min P, Aljohani ASM, Zulkifli MY, Alajmi FDH, Alhumaydhi FA, Kadmouse Aldeehani A, Ali Hashim M. The development of new homogenous and heterogeneous catalytic processes for the treatment of low grade palm oil. *J Mol Liq*. 2021; 344:117574. https://doi.org/10.1016/j.molliq.2021.117574

[11] Mateos PS, Casella ML, Briand LE, Matkovic SR. Transesterification of waste cooking oil with a commercial liquid biocatalyst: Key information revised and new insights. *J. Am. Oil Chem. Soc*. 2023; 100(4): 287-301. https://doi.org/10.1002/aocs.12683

[12] Ahmed R, Huddersman K. Review of biodiesel production by the esterification of wastewater containing fats oils and grease (FOGs). *J Ind Eng Chem*. 2022; 110: 1-14. https://doi.org/10.1016/j.jiec.2022.02.045

[13] Rattanaphra D, Harvey AP, Thanapimmetha A, Srinophakun P. Kinetic of myristic acid esterification with methanol in the presence of triglycerides over sulfated zirconia. *Renew Energy*. 2011; 36(10): 2679-2686. https://doi.org/10.1016/j.renene.2011.02.018

[14] Atadashi IM, Aroua MK, Abdul Aziz AR, Sulaiman NMN. The effects of catalysts in biodiesel production. *J Ind Eng Chem.* 2013; 19(1): 14-26. https://doi.org/10.1016/j.jiec.2012.07.009

[15] Lam MK, Lee KT, Mohamed AR. Homogeneous, heterogeneous and enzymatic catalysis for transesterification of high free fatty acid oil (waste cooking oil) to biodiesel. *Biotechnol Adv*. 2010; 28(4): 500-518. https://doi.org/10.1016/j.biotechadv.2010.03.002

[16] Abdulmalek SA, Yan Y. Recent developments of lipase immobilization technology and application of immobilized lipase mixtures for biodiesel production. *Biofuels Bioprod Bioref*. 2022; 16(4): 1062-109. https://doi.org/10.1002/bbb.2349

[17] Jamil F, Saleem M, Ali Qamar O, Khurram MS, Al-Muhtaseb AH, Inayat A, Akhter P, Hussain M, Rafiq S, Yim H, Park YK. State-of-the-art catalysts for clean fuel (methyl esters) production—a comprehensive review. *J Phys Energy*. 2023; 5(1): 014005. https://doi.org/10.1088/2515-7655/aca5b3

[18] Bölük S, Sönmez Ö. Microwave-Assisted Esterification of Oleic Acid Using an Ionic Liquid Catalyst. *Chem Eng Technol*. 2020; 43(9): 1792-1801. https://doi.org/10.1002/ceat.202000045

[19] Hayyan A, Hashim MA, Hayyan M. Application of a Novel Catalyst in the Esterification of Mixed Industrial Palm Oil for Biodiesel Production. *Bioenergy Res*. 2015; 8(1): 459-463. https://doi.org/10.1007/s12155-014-9502-0

[20] Winfield DD, Moser BR. Selective hydroxyalkoxylation of epoxidized methyl oleate by an amphiphilic ionic liquid catalyst. *J Am Oil Chem Soc*. 2022; 100(3): 237-243 https://doi.org/10.1002/aocs.12672

[21] Hayyan A, Yeow ATH, Alkahli NAM, Saleh J, Aldeehani AK, Alkandari KH, Alajmi FD, Alias Y, Junaidi MUM, Hashim MA, Basirun WJ, Abdelrahman MAA. Application of acidic ionic liquids for the treatment of acidic low grade palm oil for biodiesel production. *J Ionic Liq*. 2022; 2(1): 100023. https://doi.org/10.1016/j.jil.2022.100023

[22] Hayyan A, Ali Hashim M, Mjalli FS, Hayyan M, AlNashef IM. A novel phosphonium-based deep eutectic catalyst for biodiesel production from industrial low grade crude palm oil. *Chem Eng Sci*. 2013; 92: 81-88. https://doi.org/10.1016/j.ces.2012.12.024

[23] Hayyan A, Hizaddin HF, Abed KM, Mjalli FS, Hashim MA, Abo-Hamad A, Saleh J, Aljohani ASM, Alharbi YM, Alhumaydhi FA, Ahmad AA, Yeow ATH, Aldeehani AK, Alajmi FDH, Al Nashef I. Encapsulated deep eutectic solvent for esterification of free fatty acid. *Biomass Convers Biorefin*. 2022; 12(9): 3725-3735. https://doi.org/10.1007/s13399-021-01913-z

[24] Pelit E. Synthesis of isoxazolopyridines and spirooxindoles under ultrasonic irradiation and evaluation of their antioxidant activity. *J Chem*. 2017; 2017(1).9161505. https://doi.org/10.1155/2017/9161505

[25] Zhai Y, Pan K, Zhang E. Anti-Corrosive Coating of Carbon-Steel Assisted by Polymer-Camphorsulfonic Acid Embedded Within Graphene. *Coatings*. 2020; 10(9): 897. https://doi.org/10.3390/coatings10090879

[26] Guo P. Three 2D AgI-framework Isomers With Helical Structures Controlled by the Chirality of Camphor-10-Sulfonic Acid. *Daltan Transanction*. 2011: 1716. https://doi.org/10.1039/C0DT01384F

[27] Krupińska I. The influence of aeration and type of coagulant on effectiveness in removing pollutants from groundwater in the process of coagulation. *Chem Biochem Eng Q*. 2016; 30(4): 465-475. https://doi.org/10.15255/CABEQ.2014.2016

[28] GY Han, GQ Shi, LT Qu, JY Yuan, FE Chen PW. Electrochemical Polymerization of Chiral Pyrrole Derivatives in Electrolytes Containing Chiral Camphor Sulfonic Acid. *Polymer International.* 2004*:* 53 (10): 1554-1560. https://doi.org/10.1002/pi.1597

[29] Garcia FJ, Rubio A, Sainz E, Gonzalez P, Lopez FA. Preliminary study of treatment of sulphuric pickling water waste from steelmaking by bio-oxidation with Thiobacillus ferrooxidans. *FEMS Microbiol Rev*. 1994; 14(4): 397-404. https://doi.org/10.1111/j.1574-6976.1994.tb00114.x

[30] American Oil Chemist's Society. Ca 5a-40: free fatty acids, in: Official Methods and Recommended Practices of the AOCS. 5th ed. Champaign, IL; 1998. ISBN: 978-0-935315-82-8.

[31] Park SH, Khan N, Lee S, Zimmermann K, DeRosa M, Hamilton L, Hudson W, Hyder S, Serratos M, Sheffield E. Biodiesel production from locally sourced restaurant waste cooking oil and grease: synthesis, characterization, and performance evaluation. *ACS Omega*. 2019; 4(4): 7775-7784. https://doi.org/10.1021/acsomega.9b00268

[32] Ude CN, Onukwuli OD, Ugwu BI, Okey-Onyesolu CF, Ezidinma TA, Ejikeme PM. Methanolysis optimization of cottonseed oil to biodiesel using heterogeneous catalysts. *Iran. J Chem Chem Eng*. 2020; 39(4): 355-370. https://doi.org/10.30492/ijcce.2020.43368

[33] Borugadda VB, Goud V V. Response surface methodology for optimization of bio-lubricant basestock synthesis from high free fatty acids castor oil. *Energy Sci Eng*. 2015; 3(4): 371-83. https://doi.org/10.1002/ese3.77

[34] Evans R. Verifying Model Assumptions and Testing Normality. *Vet. Surg*. 2024; 53(1). 17. https://doi.org/10.1111/vsu.14034

[35] Jia P, Lan X, Li X, Wang T. Highly Active and Selective NiFe/SiO2 Bimetallic Catalyst with Optimized Solvent Effect for the Liquid-Phase Hydrogenation of Furfural to Furfuryl Alcohol. *ACS Sustain Chem Eng*. 2018; 6(10): 13287-13295. https://doi.org/10.1021/acssuschemeng.8b02876

[36] Xie W, Gao C, Wang H. Biodiesel production from low-quality oils using heterogeneous cesium salts of vanadium-substituted polyoxometalate acid catalyst. *Catalysts*. 2020; 10(9): 1060. 1-13. https://doi.org/10.3390/catal10091060

[37] Faruque MO, Razzak SA, Hossain MM. Application of heterogeneous catalysts for biodiesel production from microalgal oil—a review. *Catalysts*. 2020; 10(9): 1025. https://doi.org/10.3390/catal10091025

[38] Ma'arof NANB, Hindryawati N, Khazaai SNM, Bhuyar P, Rahim MHAb, Maniam GP. Biodiesel (Methyl Esters). *Maejo Int. J. Energy Environ Commun*. 2021; 3(1): 30-43. https://doi.org/10.54279/mijeec.v3i1.245153

[39] Xie W, Wang H. Immobilized polymeric sulfonated ionic liquid on core-shell structured Fe3O4/SiO2 composites: A magnetically recyclable catalyst for simultaneous transesterification and esterifications of low-cost oils to biodiesel. *Renew Energy*. 2020; 145: 1709-1719. https://doi.org/10.1016/j.renene.2019.07.092

[40] Díaz L, Borges ME. Low-quality vegetable oils as feedstock for biodiesel production using k-pumice as solid catalyst. Tolerance of water and free fatty acids contents. *J Agric Food Chem*. 2012; 60(32): 7928-3793. https://doi.org/10.1021/jf301886d

[41] Khor CP, Jaafar M bt, Ramakrishnan S. Optimization of Conductive Thin Film Epoxy Composites Properties Using Desirability Optimization Methodology. *J Optim*. 2016: 652928. 1652928. https://doi.org/10.1155/2016/1652928

[42] Loryuenyong V, Kaewmanee S, Rattanawaraporn S, Chimplenapanon N, Buasri A. Optimization of microwave-assisted biodiesel production using Iron (III) oxide - Calcium oxide / Activated charcoal derived from waste Asian green mussel shell as heterogeneous catalyst. *IOP Conf Ser Mater Sci Eng*. 2023; 1280(1): 012004. https://doi.org/10.1088/1757-899x/1280/1/012004

[43] Melchiorre M, Amoresano A, Budzelaar PHM, Cucciolito ME, Mocerino F, Pinto G, Ruffo F, Tuzi A, Esposito R. Parts-Per-Million (Salen)Fe(III) Homogeneous Catalysts for the Production of Biodiesel from Waste Cooking Oils. *Catal Letters*. 2022; 152(12): 3785-3794. https://doi.org/10.1007/s10562-022-03948-x

[44] Betiku E, Etim AO, Pereao O, Ojumu TV. Two-Step Conversion of Neem (Azadirachta indica) Seed Oil into Fatty Methyl Esters Using a Heterogeneous Biomass-Based Catalyst: An Example of Cocoa Pod Husk. *Energy Fuels*. 2017; 31(6): 6182-6193. https://doi.org/10.1021/acs.energyfuels.7b00604

[45] Chai M, Tu Q, Lu M, Yang YJ. Esterification pretreatment of free fatty acid in biodiesel production, from laboratory to industry. *Fuel Process. Technol*. 2014; 125: 106-113. https://doi.org/10.1016/j.fuproc.2014.03.025

[46] Okpalaeke KE, Ibrahim TH, Latinwo LM, Betiku E. Mathematical Modeling and Optimization Studies by Artificial Neural Network, Genetic Algorithm and Response Surface Methodology: A Case of Ferric Sulfate-Catalyzed Esterification of Neem (Azadirachta indica) Seed Oil. *Front Energy Res*. 2020; 8(November): 1-14. https://doi.org/10.3389/fenrg.2020.614621

[47] Anil N, Rao PK, Sarkar A, Kubavat J, Vadivel S, Manwar NR, Paul B. Advancements in sustainable biodiesel production: A comprehensive review of bio-waste derived catalysts. *Energy Convers Manag*. 2024; 318: 118884. https://doi.org/https://doi.org/10.1016/j.enconman.2024.118884

[48] Pasha MK, Dai L, Liu D, Guo M, Du W. An overview to process design, simulation and sustainability evaluation of biodiesel production. *Biotechnol Biofuels*. 2021; 14(1): 1-24. https://doi.org/10.1186/s13068-021-01977-z

[49] Kokanović A, Ajdačić V, Terzić Jovanović N, Stankic S, Opsenica IM. Pd Nanoparticles Supported on Ultrapure ZnO Nanopowders as Reusable Multipurpose Catalysts. *ACS Appl Nano Mater*. 2023; 6(17): 15820-15828. https://doi.org/10.1021/acsanm.3c02743

[50] Rathore D, Sevda S, Prasad S, Venkatramanan V, Chandel AK, Kataki R, Bhadra S, Channashettar V, Bora N, Singh A. Bioengineering to Accelerate Biodiesel Production for a Sustainable Biorefinery. *Bioeng*. 2022; 9(11): 618. 1ttps://doi.org/10.3390/bioengineering9110618

[51] Alhomaidi E, Aljabri M, Alsharari SS, Alsam A. Chromatographic assessment of biodiesel production from Peganum harmala seed oil using environmentally benign nano-catalysts. *Biomed Chromatogr*. 2024; 38(3): e5794. https://doi.org/10.1002/bmc.5794

[52] Oloyede CT, Jekayinfa SO, Alade AO, Ogunkunle O, Otung NAU, Laseinde OT. Exploration of agricultural residue ash as a solid green heterogeneous base catalyst for biodiesel production. *Eng Rep*. 2023; 5(1): 1-23. https://doi.org/10.1002/eng2.12585

Primena metoda površine odgovora za optimizaciju procesa visoke konverzije slobodnih masnih kiselina korišćenjem (1R)-(-)-kamfor-10-sulfonske kiseline i gvožđe(III) sulfata

Adeeb Hayyan[1,2], Khalid M. Abed[1,3], Mohammed A. Al-Saadi[4], Amal A. M. Elgharbawy[5,6], Yousef Mohammed Alanazi[7], Jehad Saleh[7], Nur Hanie Mohd Latiff[8], Sharifah Shahira Syed Putra[9], Mohd Roslan Mohd Nor[10] i Shareef Fadhil Mahel Alhashemi[11]

[1]*Department of Chemical Engineering, Faculty of Engineering, Universiti Malaya, Kuala Lumpur, Malaysia*
[2]*Sustainable Process Engineering Centre (SPEC), Faculty of Engineering, Universiti Malaya, Kuala Lumpur, Malaysia*
[3]*Department of Chemical Engineering, College of Engineering, University of Baghdad, Baghdad, Iraq*
[4]*National Chair of Materials Science and Metallurgy, University of Nizwa, Nizwa, Oman*
[5]*International Institute for Halal Research and Training (INHART), International Islamic University Malaysia, Kuala Lumpur, Malaysia*
[6]*Bioenvironmental Engineering Research Centre (BERC), Department of Biotechnology Engineering, Faculty of Engineering, International Islamic University Malaysia (IIUM), Kuala Lumpur, Malaysia*
[7]*Department of Chemical Engineering, College of Engineering, King Saud University, Riyadh, Saudi Arabia*
[8]*Global Centre for Environmental Remediation (GCER), College of Engineering, Science, and Environment (CESE), University of Newcastle, Callaghan, Australia*
[9]*Faculty of Industrial Sciences and Technology, Universiti Malaysia Pahang Al-sultan Abdullah, Lebuhraya Tun Abdul Razak, 26300 Gambang, Pahang, Malaysia*
[10]*Halal Research Group, Academy of Islamic Studies, Universiti Malaya, Kuala Lumpur, Malaysia*
[11]*Department of Chemistry, College of Science, Sultan Qaboos University, Muscat, Oman*

(Naučni rad)

Izvod

U radu je izvršeno ispitivanje proizvodnje biodizela iz kiselog sirovog palminog ulja korišćenjem jednog homogenog katalizatora, (1R)-(-)-kamfor-10-sulfonske kiseline (10-CSA) i jednog heterogenog katalizatora, gvožđe(III) sulfata, sa aspekta njihove katalitičke aktivnosti, mogućnosti recikliranja i optimizacije procesa primenom metode odgovora površine. Optimalni uslovi su identifikovani korišćenjem Bok-Behnken faktorskog dizajna. Za 10-CSA, optimizovani uslovi su dali smanjenje slobodnih masnih kiselina (FFA) na 0,43 mas.%, sa dozom katalizatora od 1,5 mas.% (ispitani opseg: 1,0-2,0 mas.%), molarnim odnosom metanola i ulja od 12,60 g do 1:1:1 (umereno temperaturno područje), temperaturom od 59,6 °C (ispitani opseg: 50 do 65 °C), i vremenom reakcije od 33,1 min (ispitani opseg: 30 do 40 min). Za gvožđe(III) sulfat, optimizovani uslovi su doveli do smanjenja FFA na 1,04 mas.%, sa dozom katalizatora od 3,14 mas.% (ispitani opseg: 2,5 do 3,5 mas.%), molarnim odnosom metanola i ulja od 12:1 (ispitani opseg temperature od 1:10°C), temperaturom reakcije od 60 °C (ispitani opseg: 55 do 70 °C), i vreme reakcije od 178,6 min (ispitani opseg: 150 do 180 min). Rezultati ANOVA analize su potvrdili značaj ključnih faktora za oba katalizatora (p <0,05), sa vrednostima R^2 od 0,937 za 10-CSA i 0,916 za gvožđe(III) sulfat, što ukazuje na dobro uklapanje modela. Srednja relativna procentna devijacija bila je <5 % za oba modela, što pokazuje visoku tačnost predviđanja. Utvrđeno je da je nedostatak uklapanja beznačajan (p >0,05), što potvrđuje adekvatnost modela. Oba katalizatora su postigla visoku konverziju FFA od 95,2 % za 10-CSA i 88,2 % za gvožđe(III) sulfat, što ispunjava standarde EN 14214 i ASTM D6751. Značajno je da je 10-CSA pokazao bolju katalitičku aktivnost i mogućnost recikliranja, čime se ističe njegov potencijal za proizvodnju biodizela u industrijskim razmerama. Ova studija nudi praktičan uvid u optimizaciju procesa esterifikacije za proizvodnju biodizela iz kiselog sirovog palminog ulja.

Ključne reči: kiselo sirovo palmino ulje; biodizel; esterifikacija; homogeni kiseli katalizator; heterogeni kiseli katalizator

Effects of buckwheat and millet flour addition on the antioxidant potential of wheat flour and rheological properties of the dough

Marica B. Rakin[1], Danica B. Zarić[2], Tanja Ž. Krunić[2] and Maja Lj. Bulatović[1]

[1]University of Belgrade, Faculty of Technology and Metallurgy, Belgrade, Serbia
[2]Innovation Center of the Faculty of Technology and Metallurgy, Belgrade, Serbia

ORIGINAL SCIENTIFIC PAPER

UDC: 664.653.1:664.641.2:
664.641.12

Hem. Ind. **79(2)** 93-101 (2025)

Abstract

In this work, the antioxidant properties of three types of flour (wheat, buckwheat and millet flour) and rheological properties of three types of dough were investigated: wheat flour dough, dough obtained from a mixture of 50 wt.% wheat flour and 50 wt.% buckwheat flour and dough obtained from a mixture of 50 wt.% wheat flour and 50 wt.% millet flour. Polyphenol content and antioxidant tests have shown that buckwheat flour is superior to wheat and millet flour. The antioxidant activity expressed by the 2,2-diphenyl-1-picrylhydrazyl radical scavenging activity did not correlate with the content of polyphenols, which is a consequence of the presence of tannins and phytic acid in millet flour. Determination of rheological properties was performed by a universal dough characterizer. The substitution of wheat flour with buckwheat and millet flour leads to a weakening of the protein structure. Furthermore, the addition of buckwheat or millet flour reduces the rate of gelatinization and viscosity and has a positive effect on the reduction of retrogradation. The combination of these two types of flour with wheat flour can reduce the aging of bakery products.

Keywords: Mixolab; dough rheology; antioxidants; composite flour.

Available on-line at the Journal web address: http://www.ache.org.rs/HI/

1. INTRODUCTION

Bread and bakery products are the most represented group of products in our diet. The main raw material in these products is wheat flour, which is considered a nutritionally poor raw material in terms of essential amino acids, dietary fiber, polyphenols and minerals [1]. The amino acid profile of wheat flour protein is poor in essential amino acids such as lysine, threonine and methionine [2]. To overcome this deficiency in wheat bakery products, wheat is partially or completely replaced with other cereals or pseudocereals to create enriched functional products. The food industry is faced with a technological challenge, on one hand, how to enrich bakery products with missing nutritional ingredients and, on the other, not to damage the consistency of the dough, which is characteristic of wheat flour [3]. During dough kneading, wheat flour proteins (gliadin and glutenin) form the gluten matrix. Gliadin is responsible for the viscosity, and glutenin for elasticity and firmness of the dough [4]. Gluten helps in expansion and improves the ability to retain gases in the dough [5]. Enriching wheat flour with whole buckwheat or millet flour can yield bakery products with added value in the functional food category.

Buckwheat is classified as a nutritionally valuable raw material, primarily due to proteins rich in essential amino acids, vitamins, minerals and dietary fiber. The advantage of buckwheat is the lack of gluten in its composition. Hulled grain contains 55 % starch, 12 % protein, 7 % total dietary fiber, 4 % lipid, 2 % soluble carbohydrates, including sucrose and fagopyritols, 2 % ash and 18 % other components, such as vitamins, organic acids, polyphenolic compounds, tannins, nucleotides and nucleic acids. Depending on the type of buckwheat, the content of individual components may also vary [6]. Buckwheat contains large amounts of resistant starch (27 to 33.5 %), which can help control blood glucose and lipid levels, regulate intestinal microbiota and reduce obesity [7].

Buckwheat proteins have a high biological value due to a well-balanced composition of amino acids. In addition to the high content of lysine (6.1 %), buckwheat grain proteins also have a high content of arginine (9.1 %) and aspartic

---

Corresponding author: Marica B. Rakin, Faculty of Technology and Metallurgy, University of Belgrade, Karnegijeva 4, Belgrade, Serbia
E-mail: marica@tmf.bg.ac.rs

Paper received: 29 October 2023; Paper accepted: 4 February 2025; Paper published: 22 April 2025.
https://doi.org/10.2298/HEMIND240119004R

acid (11.3 %), compared to other grains. Buckwheat proteins were reported to lower cholesterol levels, have an antihypertensive effect and affect digestion [8,9].

Many studies have suggested a protective role of polyphenolic compounds in buckwheat, which help in prevention of coronary and cancer diseases. Buckwheat is a source of flavonoids, like rutin, quercetin, and kaempferol, which exhibit antioxidant and anti-inflammatory properties [10].

Millet is a grain that naturally does not contain gluten, which makes it an excellent food in the diet of people suffering from various forms of gluten and wheat intolerance. Millet has a high nutritional value, with a large amount of starch of about 60 to 70 %, protein up to 11 %, dietary fiber in the range 2 to 7 % [11,12], minerals: calcium, iron, potassium, magnesium, phosphorus, and zinc, and vitamins such as niacin, B-complex, and vitamin B6. It contains significant amounts of amino acids with sulfur (methionine and cysteine), but also other essential amino acids such as lysine and threonine. In addition, millet is rich in phenolic acids, melanoids, flavonoids and tannins, the content of which is several times higher than in other basic cereals [13].

Introducing millet into the diet, according to literature, can influence cholesterol metabolism, regulate blood pressure, liver function and slow down aging [14,15]. Millet flour is a promising source of micronutrients and proteins, but information on polyphenol compositions in flour is often limited. Nutrients and polyphenol compositions in cereals flours do not depend only on genotype but also on environmental factors. Introduction of buckwheat and millet flour into bakery and confectionery products improves functional properties of these products, while increasing the contents of proteins, dietary fibers, minerals, vitamins and antioxidants. It is undeniable that buckwheat and millet have great nutritional potential, so it is necessary to determine the influence of their addition on rheological properties of the resulting dough and antioxidant properties of the flour mixture.

2. MATERIALS AND METHODS

2. 1. Materials

Wheat flour, wholegrain buckwheat flour and millet flour were purchased in the local market (in Serbia). Chemical compositions of the three flour types (Table 1) were assessed regarding the contents of proteins, total fat, moisture and ash by using standard methods AOAC [16]. Then the carbohydrate content was determined as a balance to 100 %.

Table 1. *Chemical compositions of wheat, wholegrain buckwheat and millet flour*

	Flour samples		
	Wheat flour	Wholegrain buckwheat flour	Millet flour
	Content, wt.%		
Moisture	12.16±0.21^{a}	13.13±0.058^{b}	12.63±0.15^{c}
Proteins	11.03±0.12^{a}	10.33±0.15^{b}	8.81±0.10^{c}
Total fats	1.33±0.058^{a}	2.17±0.153^{b}	1.83±0.12^{c}
Carbohydrates	75.10±0.20^{a}	72.40±0.20^{b}	75.67±0.29^{c}
Ash	0.38±0.06^{a}	1.97±0.21^{b}	1.06±0.30^{c}

Values represent the means (n = 3) ± standard deviation. Values marked by different lower-case letters in the same row are significantly different from each other ($p < 0.05$)

Preparation of composite flours: WH - control sample (wheat flour), two types of mixture: BWH - wheat flour with wholegrain buckwheat flour (mass ratio 50 : 50) and MWH - wheat flour with millet flour (mass ratio 50 : 50)

2. 2. Determination of the total phenolic content and antioxidant activity

In this work, ethanol was used for extraction of antioxidant and phenolic compounds from flour. Extraction was performed by dissolving 1 g of flour in 20 cm^3 of 80 vol.% ethanol. The mixture was then shaken for 30 min at 25 °C and then centrifuged for 10 min at 10,000 rpm. The supernatant was used in further analysis.

2. 2. 1. Determination of the total phenolic content

The content of total phenolics in the flour was determined by the modified Folin/Ciocalteu (FC) method [17], 0.10 cm^3 of sample, 0.90 cm^3 of ethanol, 0.25 cm^3 of the FC reagent (Sigma-Aldrich, USA) and 0.75 cm^3 of sodium carbonate solution (7.5 %, m/v) were mixed. After 2 h, the absorbance was measured by using the UV/visible spectrophotometer (Ultraspec 3300 pro, Amersham Bioscience, Sweden) at 765 nm. The total phenolic content was assessed by plotting the gallic acid calibration curve and expressed as mg of GAE per g of dried sample.

2. 2. 2. Determination of 1,1-diphenyl-2-picrylhydrazyl radical scavenging activity

Antioxidant activity of samples was measured based on scavenging activities of the stable 1,1-diphenyl-2-picrylhydrazyl (DPPH) radical [18]. The samples (0.2 cm^3) were mixed with 2 cm^3 of 0.15 mM DPPH solution (Merck, USA) in ethanol. After 30 min of incubation in the dark at room temperature, the absorbance was measured against a blank at 517 nm by using the UV/visible spectrophotometer (Ultraspec 3300 pro, Amersham Bioscience, Sweden). Inhibition of DPPH radical was calculated as a DPPH capacity, % by using the Equation (1):

$$\text{DPPH capacity} = \frac{A_b - A_s}{A_b} 100 \tag{1}$$

where A_b and A_s are the absorbance of the blank and of the sample, respectively.

2. 2. 3. Determination of 2,2'-azino-bis(3-ethylbenzothiazoline-6-sulfonic acid radical scavenging activity

The 2,2'-azino-bis(3-ethylbenzothiazoline-6-sulfonic acid (ABTS) radical scavenging activity of samples was measured by using a decolorization assay. The ABTS free radical solution (Sigma-Aldrich, USA) was prepared by reaction of a 7 mM aqueous ABTS solution and a 140 mM (2.45 mM final concentration) potassium-persulfate solution. After 16 h, the radical cation solution was diluted with 5 mM phosphate-buffered saline (PBS, pH 7.4) until the initial absorbance value of 0.7 ± 0.05 at 734 nm was reached. The solution with free radicals (1.98 mL) was mixed with 20 µL of each sample, absorbance was measured at 734 nm using a UV Visible spectrophotometer (Ultrospec 3300 pro, Amerischam Bioscienc), after 5 min. ABTS radical scavenging activity, % was calculated by using Equation (2) [19]:

$$\text{ABTS radical scavening activity} = \frac{A_b - A_s}{A_b} 100 \tag{2}$$

2. 3. Rheological characteristic of dough

The mixing and pasting behaviour of the composite flours were determined in a Mixolab 2 universal dough characterizer (Chopin Technologies, France) according to the ICC Standard Method 173 using the "Chopin+" protocol [20]. The procedure was divided into the following three stages:

- Constant temperature stage: temperature was maintained at 30 °C for 8 min;
- Heating stage: temperature was increased to 90 °C at the rate of 4 °C min^{-1} and maintained at 90 °C for 7 min;
- Cooling stage: temperature was reduced to 50 °C at the rate of 4 °C min^{-1} and maintained at 50 °C for 5 min.

The measurement stage required 45 min to complete. The evaluated parameters from the obtained curves were: water absorption (WA); dough development time (DDT); stability (mixing resistance of dough); C1 (maximum torque during mixing); Cs (torque at the end of the holding time at 30 °C); C2 (weakening of the protein, based on mechanical stress at increasing temperature); C3 (rate of starch gelatinization); C4 (minimum torque during the heating period); C5 (torque after cooling at 50 °C); C5-C4 (starch retrogradation at cooling stage, representing the shelf-life of the end products).

2. 4. Statistical analysis

All experiments were performed in triplicate. Mean values were analysed using one-way ANOVA. The Tukey *post hoc* test was performed for means comparison (OriginPro 8, www.originlab.com). Differences were considered as significant at $p < 0.05$.

3. RESULTS AND DISCUSSION

3. 1. Polyphenols and antioxidant capacity

Content of polyphenols and antioxidant activities expressed as DPPH and ABTS radical scavenging activities are shown in Table 2. Both methods measure free radical scavenging activity (radical-scavenging activity - RSA) (*i.e*. DPPH and ABTS). DPPH is one of free radicals which are relatively stable at room temperature and is commonly used for determination of the antioxidant capacity of different molecules. The scavenging capacity against DPPH radical is strongly influenced by the solvent and reaction pH. The sample is usually dissolved in methanol or ethanol so that only methanol /ethanol soluble antioxidants are detected (hydrophilic polar protic molecules). The ABTS radical is soluble in water and organic solvents, enabling determination of the antioxidant capacity of both hydrophilic and lipophilic compounds. The content of polyphenols is the highest in buckwheat flour, and the lowest in the millet flour. Buckwheat flour has 5.4 times more polyphenols than wheat flour, while the millet flour has a slightly lower content that is 22 % less polyphenols than the wheat flour.

Table 2. *Antioxidant activity indicators of flour samples*

Flour	Content of polyphenols, mg g^{-1}	Content of DPPH, %	Content of ABTS, %
Millet flour	0.46 ± 0.01^{a}	19.17 ± 0.78^{a}	1.00 ± 0.21^{a}
Wholegrain buckwheat flour	3.20 ± 0.27^{b}	90.76 ± 3.14^{b}	78.90 ± 8.52^{b}
Wheat flour	0.60 ± 0.09^{ac}	14.02 ± 0.82^{c}	16.73 ± 1.82^{c}

Values represent the means ($n = 3$) ± standard deviation. Values followed by different lower-case letters in the same column are significantly from each other ($p < 0.05$)

Data reported in the literature [18] also indicate that the content of polyphenols in millet flour can be twice as low as in wheat flour. It has been also reported that polyphenolic compounds, particularly phenolic acids, negatively impact the formation of gluten networks and lead to the immediate disruption of dough structure [22,23]. The composition of polyphenols in various types of cereals is different, and therefore different antioxidant capacities should be expected [24,25]. There is a lack of correlation between the polyphenol content and antioxidant activity expressed as DPPH radical scavenging activity (Table 2). This can be explained by the presence of compounds such as tannins and phytic acid that act as antioxidants and are present in millet in greater quantity compared to wheat [25]. Antioxidant activities detected by ABTS radicals follow the content of polyphenols in the samples, and more significant differences are observed. They range from 1.0 % for millet flour to 78.9 % for wheat flour.

3. 2. Dough properties

Mixolab device offers the advantage of assessing various flour characteristics of cereals in a single test, determining the quality of proteins, starch, and associated enzymes. The influence of the addition of 50% whole buckwheat flour and 50% millet flour on the thermomechanical properties of wheat flour is shown in Figure 1, while the values of the main parameters derived from the Mixolab curve are summarized in Table 3.

The first part of the curve reveals the protein properties of the tested flour samples. Characteristic parameters for this stage of dough formation at a constant temperature of 30°C under mixing are: water absorption, dough development time, stability and mechanical weakening.

The Mixolab water absorption value signifies the quantity of water required to achieve a dough consistency of 1.1±0.05 N m and the dough development time refers to the moment of reaching the maximum torque of 1.1 N m and determines the strength of the flour. Addition of 50 % whole buckwheat flour to wheat flour led to an increase in water absorption by 9.4 %, which is due to naturally occurring hydrocolloids and buckwheat fibers [26] needing more time to absorb water. This resulted in an increase in the dough development time (by 30 %) and a decrease in the dough stability by 31.4 %. Addition of millet to wheat flour (MWH) led to a decrease in water absorption due to dilution of gluten, which is in agreement with professional literature [27,28]. The time needed to obtain 1.1 N m was higher when using BWF and MWH, even though WH contained more proteins. The dough made from wheat flour had the greatest stability, because it is also the strongest.

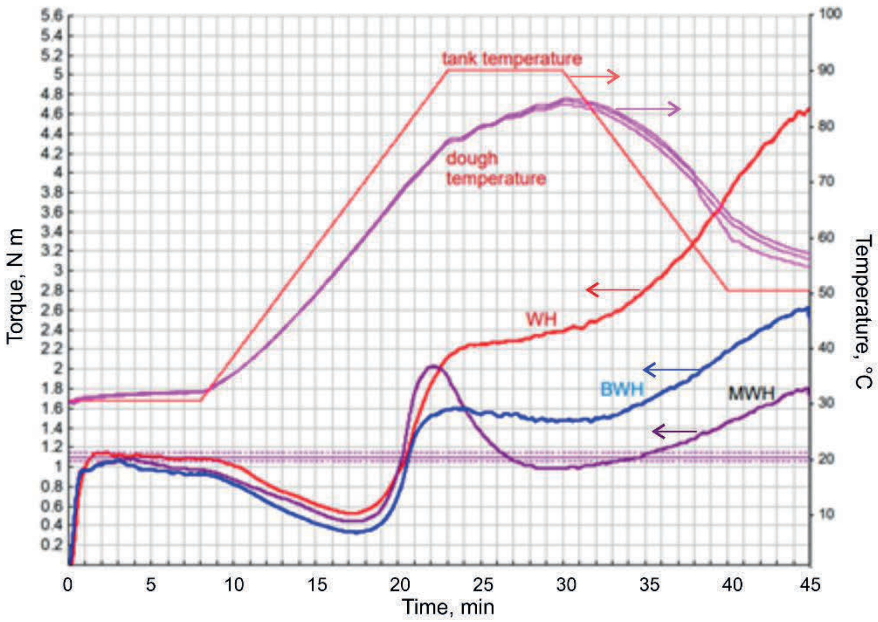

Figure 1. Typical *mixolab curves of tested flours (WH, BWH and MWH)*

Table 3. *Mixolab characteristics of tested flours*

Flour	WA, wt.%	DDT, min	Stability, min	Cs, N m	C2, N m	C3, N m	C4, N m	C5, N m
WH	53.21±0.23^{a}	2.32±0.55^{a}	9.33±0.09a	1.09±0.01^{a}	0.53±0.01^{a}	2.17±0.03^{a}	2.34±0.03^{a}	4.35±0.08^{a}
BWH	57.22±0.11^{b}	3.00±0.38^{a}	6.41±0.21b	0.93±0.02^{b}	0.33±0.01^{b}	1.60±0.01^{b}	1.46±0.02^{b}	2.48±0.05^{b}
MWH	45.00±0.12^{c}	3.91±0.24^{b}	8.41±0.18c	0.97±0.01^{cb}	0.44±0.02^{c}	2.02±0.01^{c}	0.98±0.02^{c}	1.69±0.03^{c}

Values represent the means (n = 3) ± standard deviation. Values followed by different lower-case letters in the same column are significantly from each other ($p < 0.05$)

When the dough temperature is increased from 30°C at a rate of 4°C min^{-1} and mixing continues at a constant speed, the strength of the dough decreases as a result of protein attenuation. An increase in the temperature of the dough implies protein denaturation, which includes the release of water. A decrease in resistance occurs to the lowest point - C2 [29]. C2 point gauges the reduction in protein strength resulting from mechanical work and rising temperature. The lower the C2 value, the weaker the gluten quality, which weakens the ability to retain gas and rise the dough. The higher the C2 value, the better the gluten quality, but if the C2 value is too high, this means that the gluten is too strong and can therefore limit the rise of the dough. High-quality wheat flour exhibits a torque C2 value exceeding 0.4 N m. A range of 0.5 to 0.6 N m suggests superior protein quality, enhanced gluten resistance to heating, and a more robust gluten network.

The value of C2 depends on the characteristics and amount of protein and for the wheat flour it is 0.53 N m, while for the composite flour BWH and MWH it is 0.33 and 0.44 N m, respectively. The reduction of C2 in composite flours is the result of dilution of the gluten content, *i.e.* the addition of incompatible buckwheat and millet proteins, which leads to an increase in the rate of protein weakening due to heat [30,27]. Proteins of lower quality than gluten are less stable and exhibit lower C2. As heating continued, the second part of the curve follows the changes in the dough structure caused by the rise in temperature and mechanical forces of mixing. It depends on characteristics of the starch and enzymatic activity in the flour. The torque starts to increase as a consequence of the starch gelatinization process. In this process, consistency increases due to structural changes: loss of the crystal structure, breaking of glucosidic bonds and establishment of new molecular interactions. Starch grains in contact with water released by protein denaturation slowly swell and the crystal structure is lost. Swelling of starch originating from cereals is primarily a consequence of the presence of amylopectin, because the amylopectin shell breaks, and the contents are released into the surrounding. Amylose acts as a swelling inhibitor [31]. The poured grains slowly stick together forming a high viscosity mater. During heating, disruption of the crystalline regions, primarily composed of amylopectin, allows water absorption and granule expansion and amylose molecules leach out, resulting in an increase in the viscosity with a concomitant increase in the maximum peak torque C3 produced during this heating stage. The value of the maximum torque C3 can be influenced by the content and type of starch, amylolytic activity, damage to starch grains, wheat variety, agroecological conditions during cultivation, *etc.* [32]. Increasing the amount of additives (*i.e.* buckwheat and millet flour) in wheat flour yield lower values of the maximum torque C3, *i.e.* lower viscosity due to different nature of starch in gluten-free flours. The reduction compared to wheat flour is 26.3 % for BWH by and 6.9 % for MWH. The results obtained are consistent with data reported in the literature [33], according to which replacing wheat flour with millet flour leads to a decrease in viscosity. The maximum viscosity (C3) is positively correlated with the viscosity index of the Mixolab profiler, shown in Table 4 (wheat flour 8, mixture with whole buckwheat flour 4, and with millet flour 7). The Mixolab profiler converts the mixolab curve into 6 indexes rated 0-9. It profiles flour on the basic 6 fundamental criteria: absorption (reflects flour quality), mixing (assesses dough stability during kneading at 30°C), gluten (measures gluten behaviour under heat), viscosity, amylase (amylase activity) and retrogradation.

Table 4. *Mixolab profiler index for tested flours*

	Mixolab index rate					
Flour	Absorption	Mixing	Gluten+	Viscosity	Amylase	Retrogradation
WH	1	5	5	8	9	8
BWH	3	2	2	4	6	7
MWH	0	3	5	7	1	4

When the dough is kept at 90°C for 7 min, the torque of the dough decreases until the point C4 is reached, *i.e*. the resistance of the dough in the starch gel phase. The C4 torque reflects the stability of the hot starch paste which decreases slightly for the composite flours. The drop in hot consistency of starch (C3-C4) is greater if amylase activity is higher. Compared to wheat flour, amylase activity is higher in both MWH and BWH. Ninomiya *et al.* found that buckwheat albumin maintained high α-amylase inhibitory activity even after heating at 100 °C for 120 min [34].

During cooling to 50 °C, retrogradation of starch occurs and the consistency of the dough increases. The amylose molecules, which in the phase of swelling and destruction of the starch granule passed into the water phase, are oriented parallel to each other and connected by hydrogen bonds. The re-establishment of the crystalline structure leads to association of starch molecules, resulting in the formation of strong gels, increased viscosity (C5), and a loss of water retention capacity. Upon cooling, amylose reorganizes and forms a stable gel structure. Amylose, due to its linear structure, exhibits a greater tendency for retrogradation compared to amylopectin, which is more branched. This results in faster and more pronounced retrogradation in products that are rich in amylose. This process occurs spontaneously, as it results in a decrease in the free energy of the system, thereby maintaining thermodynamic stability. Wheat flour had the highest values of the degree of retrogradation (2.01 N m) expressed as the difference between C5 and C4 torque values than in the investigated composite flour types. For the mixture with buckwheat flour, the degree of retrogradation is 1.02 N m, and for the mixture with millet flour it is 0.71 N m. Thus, starch retrogradation is minimal in the samples with millet flour (MWH), which we consider to be a result of the highest amylose content. According to the literature [35], the amylose content in millet flour is approximately 33 wt.%, compared to 30 wt.% in wheat flour and around 25 wt.% in buckwheat flour. In a previous study [36], it was also observed that retrogradation is lower in millet flour, and it is suggested that the reduction in C5 as compared to wheat flour, is a consequence of a lower number of dextrins that can form following starch hydrolysis. Additionally, Bharati *et al.* [27] have noted the positive effect of incorporating millet flour on retrogradation.

. The retrogradation index of the Mixolab profiler shown in Table 3 is inversely proportional to the shelf life of the product, namely the higher the index, the faster the bakery product ages (WH flour 8, BWH flour 7, and MWH 4). So, reduction in retrogradation is significant due to the freshness of bakery products, so if we want the best freshness of those products, it is desired to add millet flour. The reason for reduction in retrogradation should be found in the difference in the structure and amount of amylose and amylopectin fraction in non-gluten flour starch compared to wheat starch.

4. CONCLUSION

Addition of whole buckwheat flour and millet flour to wheat flour led to an increase in lipids and mineral substances, and a weakening of the gluten structure of the dough. Prolonging the dough development time while simultaneously reducing dough stability is characteristic of the addition of buckwheat and millet to wheat dough. Also, both types of flour led to a decrease in the maximum torque of the hot starch suspension. Reduction in retrogradation is affected by buckwheat flour, but significantly more by millet flour. thus, if a bakery product with extended freshness is needed, wheat flour should be enriched with millet flour.

The polyphenol content, as well as the antioxidant activity expressed through DPPH and ABTS radicals, was highest in buckwheat flour. Thus, the polyphenol content was as much as 6.9 times higher than in millet flour and 5.4 times higher than in wheat flour. In terms of improving functionality of bakery and confectionery products made from wheat flour, a more significant contribution would be achieved by the addition of buckwheat flour compared to millet flour. Still, the contribution effects of both types of flour to wheat flour are evident. Further research can be directed to a blend of wheat, buckwheat and millet flour in proportions where the wheat flour content is lower than 50 wt.%.

Acknowledgement: This work was supported by the Ministry of Science, Technological Development and Innovation of the Republic of Serbia (Contract No. 451-03-68/2022-14/200287).

REFERENCES

[1] Sabanis D, Tzia C. Effect of Rice, Corn and Soy Flour Addition on Characteristics of Bread Produced from Different Wheat Cultivars. *Food Bioprocess Tech.* 2009; 2: 68-79. https://doi.org/10.1007/s11947-007-0037-7

[2] Jiang XL, Tian JC, Hao Z, Zhang WD. Protein Content and Amino Acid Composition in Grains of Wheat-Related Species. *Agr Sci China*. 2008; 7(3): 272-279. https://doi.org/10.1016/S1671-2927(08)60066-8

[3] Gill S, Vasanthan T, Ooraikul B, Rossnagel B. Wheat Bread Quality as Influenced by the Substitution of Waxy and Regular Barley Flours in Their Native and Extruded Forms, *J Cereal Sci*. 2002; 36(2): 219-237. https://doi.org/10.1006/jcrs.2001.0458

[4] Rani S, Singh R, Kamble DB, Upadhyay A, Kaur BP. Structural and quality evaluation of soy enriched functional noodles. *Food Biosci*. 2019; (32): 100465. https://doi.org/10.1016/j.fbio.2019.100465

[5] Dhaka V, Khatkar BS. Effects of Gliadin/Glutenin and HMW-GS/LMW-GS Ratio on dough rheological properties and bread-making potential of wheat varieties. *J Food Qual.* 2015; 38(2): 71- 82. https://doi.org/10.1111/jfq.12122

[6] Krkošková B, Mrázová Z. Prophylactic components of buckwheat. *Food Res Intern.* 2005; 38(5): 561-568. https://doi.org/10.1016/j.foodres.2004.11.009

[7] Martínez-Villaluenga C, Peñas E, Hernández-Ledesma B. Pseudocereal grains: Nutritional value, health benefits and current applications for the development of gluten-free foods. *Food Chem Toxicol*. 2020; 137: 111178. https://doi.org/10.1016/j.fct.2020.111178

[8] Kayashita J, Shimaoka I, Nakajyoh M. Hypocholes-terolemic effect of buckwheat protein extract in rats fed cholesterol enriched diets. *Nutr Res*. 1995; 15: 691-698. http://dx.doi.org/10.1016/0271-5317(95)00036-I

[9] Li SQ, Zhang QH. Advances in the development of functional foods from buckwheat, *Crit Rev Food Sc. Nutr*. 2001; 41: 451-464. https://doi.org/10.1080/20014091091887

[10] Chao PL, Hsiu S, Hou Y. Flavonoidsinherbs: Biologicalfates and potential interactionswith xenobiotics. *J Food Drug Anal*. 2002; 10: 219-228. https://doi.org/10.38212/2224-6614.2738

[11] Bangar SP, Ashogbon AO, Dhull SB, Thirumdas R, Kumar M, Hasan M, Chaudhary V, Pathem S. Proso-millet starch: Properties, functionality, and applications. *Int J Biol Macromol* 2021; 190: 960-968. https://doi.org/10.1016/j.ijbiomac.2021.09.064

[12] Punia S, Kumar M, Siroha AK, Kennedy JF, Dhull SB, Whiteside WS. Pearl millet grain as an emerging source of starch: A review on its structure, physicochemical properties, functionalization, and industrial applications. *Carbohydr Polym*. 2021; 260: 117776, https://doi.org/10.1016/j.carbpol.2021.117776

[13] Kumar A, Kumari P, Kumar M. Role of millets in disease prevention and health promotion. In: Singh RB,, Watanabe S and Isaza AA,, eds. *Functional Foods and Nutraceuticals in Metabolic and Non-Communicable Diseases*. Academic Press: Cambridge, MA, USA; 2022:341-357 https://doi.org/10.1016/C2019-0-00254-3

[14] Shahidi F, Chandrasekara A. Millet grain phenolics and their role in disease risk reduction and health promotion. *J Funct Foods*. 2013; 5: 570-581. https://doi.org/10.1016/j.jff.2013.02.004

[15] Nishizawa N, Sato D, Ito Y, Nagasawa T, Hatakeyama Y, Choi MR, Choi YY, Yi MW. Effects of dietary protein of proso millet on liver injury induced by Dgalactosamine in rats. *Biosci Biotechnol Biochem.* 2002; 66: 92-96. https://doi.org/10.1271/bbb.66.92

[16] Horwitz W. *Official Methods of Analysis of AOAC International.* 17th ed., Vol 1, Gaithersburg, USA, DC: Association of Official Agricultural Chemists; 2000. ISBN 9780935584677

[17] Singleton VL, Orthofer R, Lamuela-Raventos RM. Analysis of total phenols and other oxidation substrates and antioxidants by means of Folin-Ciocalteu reagent. *Methods Enzymol.* 1999; 299: 152-178. https://doi.org/10.1016/S0076-6879(99)99017-1

[18] Balakrishnan G, Agrawal R. Antioxidant activity and fatty acid profile of fermented milk prepeared by Pediococcus pentosaceus. *J Food Sci Technol.* 2014; 51: 4138-4144. https://doi.org/10.1007/s13197-012-0891-9

[19] Re R, Pellegrini N, Proteggente A, Panniala A, Yang M, Rice-Evans C. Antioxidant activity applying an improved ABTS radical cation decolorization assay. *Free Radic Biol Med.* 1999; 26: 1231-1237. https://doi.org/10.1016/s0891-5849(98)00315-3

[20] Dubat A., Boinot N. *Mixolab Applications Handbook Rheological and Enzymatic Analysis*. 17th ed., Villeneuve la Garenne - France, Chopin Technologies; 2009 www.eqec.pt/doc_ficheiros/091023_mixolab_appli_en.pdf

[21] Poleksić D. Antioxidant and functional properties of durable bakery products with addition of proso millet (*Panicum miliaceum l.*), Ph.D. Thesis, Faculty of Agriculture University of Belgrade, 2018. https://nardus.mpn.gov.rs/bitstream/id/13432/Disertacija.pdf (in Serbian)

[22] Krekora M, Miś A, Nawrocka A. Molecular interactions between gluten network and phenolic acids studied during overmixing process with application of FT-IR spectroscopy. *J Cereal Sci.* 2021; 99: 103203. https://doi.org/10.1016/j.jcs.2021.103203

[23] Welc R, Kłosok K, Szymańska-Chargot M, Nawrocka A. Effect of chemical structure of selected phenolic acids on the structure of gluten proteins. *Food Chem.* 2022; 389: 133109. https://doi.org/10.1016/j.foodchem.2022.133109

[24] Hung VP. Phenolic Compounds of Cereals and Their Antioxidant Capacity. *Crit Rev Food Sci Nutr*. 2016; 56(1): 25-35. https://doi.org/10.1080/10408398.2012.708909

[25] Viswanath V, Urooj A, Malleshi NG. Evaluation of antioxidant and antimicrobial properties of finger millet polyphenols (*Eleusinecoracana*). *Food Chem.* 2009; 114: 340-346. http://ir.cftri.res.in/id/eprint/9086

[26] Choi UK, Yoo BH, Son DH, Kwon DJ, Kim MH, Kim YH. Rheological properties of dough added with barley bran. *Korean J Food Sci Technol*. 2005; 37: 751-756. https://koreascience.kr/article/JAKO200504637354040.pdf (in Korean)

[27] Sharma B, Singh Gujral H, Solah V. Effect of incorporating finger millet in wheat flour on mixolab behavior, chapatti quality and starch digestibility, *Food Chem.* 2017; 231: 156-164. https://doi.org/10.1016/j.foodchem.2017.03.118

[28] Pejcz E, Burešová I, Rheological Characteristics of Model Gluten-Free Dough with Plantago Seeds and Husk Incorporation. *Foods.* 2022; 11(4): 536. https://doi.org/10.3390/foods11040536

[29] Banu I, Stanojeska I, Stoenesci G, Ionescu V, Aprodu I. Estimation of the baking quality of wheat flours based on rheological parameters of the mixolab curve. *Czech J Food Sci*. 2011; 29: 35-44. https://doi.org/10.17221/40/2009-CJFS

[30] Dapčević Hadnađev T, Torbica A, Hadnađev M. Rheological properties of wheat flour substitutes/alternative crops assessed by Mixolab, *Procedia Food Sc.* 2011; 1: 328-334. https://doi.org/10.1016/j.profoo.2011.09.051

[31] Tester RF, Karkalas J, Qi X. Starch - composition, fine structure and architecture - review. *J Cereal Sci.* 2004; 39(2): 151-165. http://dx.doi.org/10.1016/j.jcs.2003.12.001

[32] Cornell HJ, Hoveling AW. The composition, properties and uses of wheat starch. In: Wheat: Chemistry and Utilization, Technomic Publishing Company, Lancaster, 1998, pp 127-172 https://doi.org/10.1201/9780367812713

[33] Goswami D, Gupta SK, Mridula D, Sharma M, Tyagi SK. Barnyard millet based muffins: Physical, textural & sensory properties. *LWT*. 2015; 64: 374-380. https://doi.org/10.1016/j.lwt.2015.05.060

[34] Ninomiya K, Ina S, Hamada A, Yamaguchi Y, Akao M, Shinmachi F, Kumagai H, Kumagai H. Suppressive effect of the α-amylase inhibitor albumin from buckwheat (*Fagopyrum esculentum* Moench) on postprandial hyperglycaemia. *Nutrients*. 2018; 10(10):1503. https://doi.org/10.3390/nu10101503

[35] Nalbandian E, Park D, Camerino N, Ganjyal GM. Value-added pancakes: Incorporation of whole wheat, buckwheat, quinoa, and proso millet flour into pancakes and their effect on product quality. *Cereal Chem.* 2025; 102, 226-238. https://doi.org/10.1002/cche.10858

[36] Chakraborty SK, Tiwari A, Mishra A, Singh A. Rheological properties of refined wheat - millet flour based dough under thermo-mechanical stress, *J Food Sci Technol.* 2014; 52(5): 3044-3050. https://doi.org/10.1007/s13197-014-1339-1

Uticaj dodatka heljde i prosa na antioksidativni potencijal i reološke karakteristike testa od pšeničnog brašna

Marica B. Rakin[1] Tanja Ž. Krunić[2], Danica B. Zarić[2] i Maja Lj. Bulatović[1]

[1]*Univerzitet u Beogradu, Tehnološko-metalurški fakultet, Beograd, Serbia*
[2]*Inovacioni centar Tehnološko-metalurškog fakulteta, Beograd, Serbia*

(Naučni rad)

Izvod

U ovom radu su ispitivana antioksidativna svojstva tri vrste brašna (pšeničnog, heljdinog I brašna od prosa) i reološka svojstva tri vrste testa: testa od pšeničnog brašna, testa od smeše 50 mas.% pšeničnog brašna/ 50 mas.% heljdinog brašna i 50 mas.% pšeničnog brašna/ 50 mas.% brašna od prosa. Sadržaj polifenola i antioksidativna ispitivanja su pokazala da je brašno od heljde značajno superiornije u odnosu i na brašno od pšenice i na brašno od prosa. Antioksidativna aktivnost izražena preko DPPH radikala nije bila u korelaciji sa sadržajem polifenola, što je posledica prisustva tanina i fitiske kiseline u brašnu od prosa. Reološka svojstva su ispitana pomoću univerzalnog uredjaja za karakterizaciju testa. Supstitucija dela pšeničnog brašna brašnom od heljde i prosa dovodi do slabljenja strukture proteina. Osim toga, dodavanje heljdinog ili brašna od prosa smanjuje brzinu želatinizacije i viskoznost, a pozitivno utiče na smanjenje retrogradacije. Kombinacija ove dve vrste brašna sa pšeničnim brašnom može dovesti do smanjivanja brzine starenja pekarskih proizvoda.

Ključne reči: Mixolab; reologija testa; antioksidansi; kompozitna brašna

Synthesis, characterization and electrochemical properties of cobalt-doped phosphate tungsten heteropoly acid and its bronze

Jovana S. Acković[1], Tamara Petrović[2], Jelena Senćanski[3], Aleksandar Mijatović[4], Stevan Blagojević[3], Pavle Tančić[5], Ružica Micić[1] and Maja Pagnacco[5]

[1]University of Priština in Kosovska Mitrovica, Faculty of Sciences and Mathematics, Department of Chemistry, Kosovska Mitrovica, Serbia
[2]University of Belgrade, Faculty of Physical Chemistry, Belgrade, Serbia
[3]University of Belgrade, Institute of General and Physical Chemistry, Belgrade, Serbia
[4]University of Belgrade, Faculty of Mining and Geology, Belgrade, Serbia
[5]University of Belgrade, Institute of Chemistry, Technology and Metallurgy, Department of Catalysis and Chemical Engineering, Belgrade, Serbia

Abstract

Heteropoly acids and their compounds are a fascinating class of multifunctional materials for use in various fields: medicine, magnetism, catalysis and nonlinear optics, as well as for electrochemistry and battery materials. This study used tungsten-phosphate heteropoly acid to synthesize and characterize its Co doped salt (Co-PWA) and tungsten-phosphate bronze (Co-PWB). Thermal analysis was used to determine Co-PWA salt phase transition into Co-PWB bronze occurring at 588 °C. Both samples were further characterized using Fourier transform infrared spectroscopy, X-ray powder diffraction and scanning electron microscopy containing energy dispersive X-ray spectroscopy, and by use of electrochemical examinations. Cyclic voltammetry (as a rapid analytical method) showed that both materials yielded low capacities in an aqueous solution of $LiNO_3$. However, a “slow” analytical method, chronopotentiometry, in which more places of a crystal lattice are occupied with ions (as compared to cyclic voltammetry), yielded solid and stable discharge capacity, making Co-PWB attractive as a potential electrode material for aqueous Li-ion batteries. The results obtained fill the gap in the scientific literature dealing with similar materials.

Keywords: Cyclic voltammetry; chronopotentiometry; lithium intercalation/deintercalation reaction; Li-ion batteries

Available on-line at the Journal web address: http://www.ache.org.rs/HI/

ORIGINAL SCIENTIFIC PAPER

UDC: 661.878`027.118:544.6.076.2

Hem. Ind. **79(2)** 103-114 (2025)

1. INTRODUCTION

Heteropoly acids (HPAs) are strong acids composed of heteropoly anions and protons as their counter cations, constituting a special case of heteropoly compounds particularly important for diverse applications [1-4]. Tungsten phosphoric acid (PWA), a special Keggin’s type compound, has the general formula $H_3PW_{12}O_{40}\times nH_2O$ ($PWA\times nH_2O$; n = 29, 21, 14, and 6) [5-9]. Tungsten phosphoric salts of heteropoly acids are obtained when one, two, or three acid hydrogen-ions are exchanged with a corresponding number of alkaline, alkaline-earth or other metal ions (cations) [10]. Among other important characteristics of heteropoly acids are that they exhibit very strong Brønsted acidity, act as proton conductors as well as undergo fast, reversible, multi-electron transfers leading to the formation of highly conductive, mixed-valence (*e.g.* tungsten(VI,V) or molybdenum(VI,V), ‘heteropoly blue’) compounds [9,11]. Heteropoly acids have been applied as electrolytes in electrochemical super capacitors [12]. Phosphate tungsten bronzes (PWBs) have been obtained through PWA thermal treatment [13-15]. These materials exhibit a variety of physical properties, including superconductivity in certain systems [16-17], could be used as electrode materials for Li-ion batteries [18], as well as exhibit interesting electronic and magnetic properties through their incorporation of metal ions into their structure [19]. Due to their 3-dimensional framework, they possess tunnels (*i.e.* channels) in their structure allowing ions such as Li^+, Na^+, K^+ to

---

Corresponding authors: Jelena Senćanski, Institute of General and Physical Chemistry, University of Belgrade, Studentski trg 12-16, 11000 Belgrade, Serbia

E-mail: jsencanski@iofh.bg.ac.rs

Paper received: 28. September 2024; Paper accepted: 26 May 2025; Paper published: 13 June 2025.

https://doi.org/10.2298/HEMIND240928008A

transport and intercalate within this structure [20,21]. Aside from the structural advantages of PWA and PWB (whose channels allow the intercalation of Li-ions into the structure), high oxidation state of tungsten (W^{6+}) in these compounds prompts their investigation as electrode materials [21,22]. PWA and PWB doped with alkali, earth alkali transition metals, as well as with rare elements have been subject of synthesis and investigation [13,15,16,21-26].

This study deals with novel synthesis and incorporation of Co ions into a heteropoly acid to form Co-PWA salt and its further thermal transformation into Co-PWB bronze. Characterization of these compounds is performed by thermal analysis (*i.e.* thermogravimetric and differential thermal analyses, TGA/DTA), Fourier transform infrared spectroscopy (FTIR), X-ray powder diffraction (XRPD) and scanning electron microscopy using an energy dispersive X-ray spectroscopy (SEM-EDS). Besides the synthesis and characterization of the Co-PWA salt and Co-PWB bronze, which are the main goals of the paper, our second goal was to examine whether these materials might be used as electrode materials for Li-ion batteries. The results obtained could eventually fill the gap in the scientific literature dealing with similar materials.

2. EXPERIMENTAL

2. 1. Synthesis of the studied phases

To carry out the synthesis of heteropoly acid $H_3PW_{12}O_{40}\times29H_2O$, the following procedure was applied: 100 g of $Na_2WO_4\times2H_2O$ (Carl ROTH, Germany) was dissolved in 100 cm^3 of distilled water. Next, 10 cm^3 of 85 % (ρ = 1.70 g cm^{-3}) H_3PO_4 (Merck, Germany) and 80 ml of 37 % (ρ = 1.19 g cm^{-3}) HCl (Merck, Germany) were added. A heteropoly cation is then formed as a white precipitate. Following the solution filtration, the precipitate was transferred to a beaker and dissolved in 100 ml of distilled water, then to a separatory funnel and 70 ml of ether (Carlo Erba, France) and 40 ml of 37 % (ρ = 1.19 g cm^{-3}) HCl were added. The bottom phase presenting the heteropoly acid solution was separated from the other two phases and put into a Petri dish to crystallize (Fig. 1a). Colorless, transparent crystals of $H_3PW_{12}O_{40}\times29H_2O$ (29-PWA; Fig. 1b) were then obtained. These were heated in a kiln at 80 °C to be desiccated for 10 min [13]. After the dehydration of $H_3PW_{12}O_{40}\times29H_2O$ (29-PWA), a compound $H_3PW_{12}O_{40}\times6H_2O$ (6-PWA) was obtained (Fig 1c).

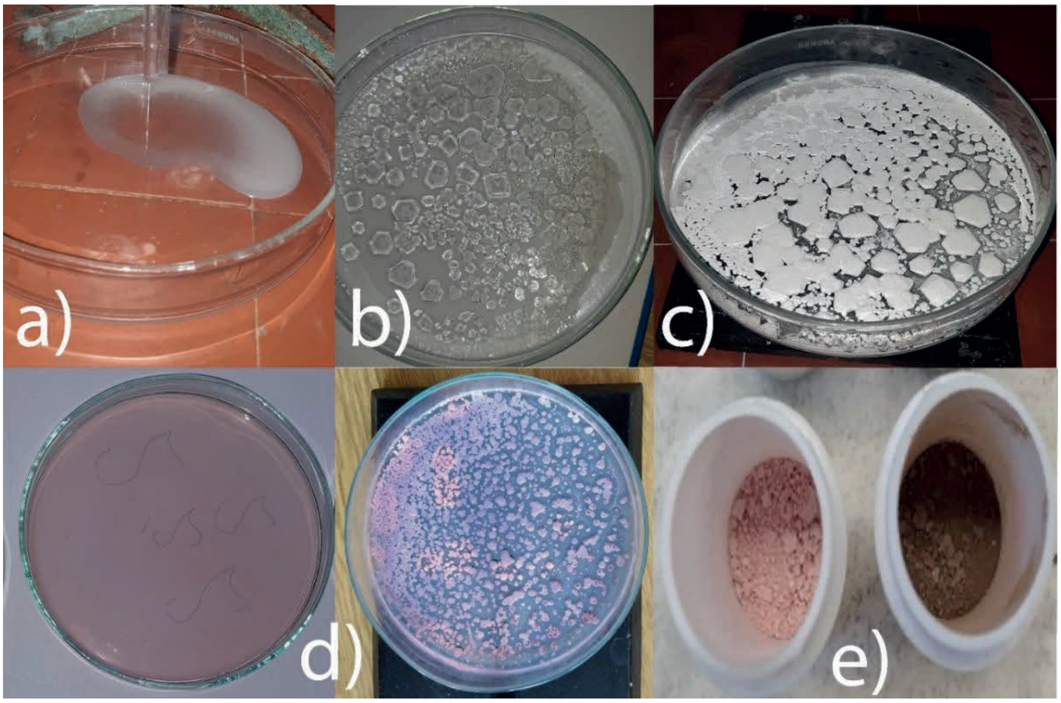

Figure 1. *Presentation of the complete synthesis process: a) heteropoly acid solution; b) beginning of the crystallization; c) formed 6-PWA; d) added $CoCl_2$ salt to the 6-PWA (left- beginning of the crystallization, and right-after crystallization) and e) Co-PWA salt (left) and corresponding Co-PWB bronze (right)*

Ion exchange in equimolar amounts of $CoCl_2\times6H_2O$ resulted in the synthesis of the salts: an aqueous solution of Co-PWA was obtained by dissolving 9.9 g of 6-PWA in distilled water and adding 0.9104 g $CoCl_2\times6H_2O$ in 10 mL of distilled water. The resulting solution was left overnight at room temperature (~25 °C) to carry out the crystallization process (Fig. 1d; purple-pink). The synthesized Co-PWA is then heated in a furnace at a program starting from room temperature rising to 650 °C (at 10 °C min^{-1}), after which Co-PWB is formed (Fig. 1e right; brown).

2. 2. Thermal examinations

Thermal examinations of Co-PWA were performed using STD 2960 Simultaneous DSC-TGA (TA instruments, USA) using a higher scanning rate (10 °C min^{-1}), rising from room temperature to 900 °C in a nitrogen stream.

2. 3. Fourier-transform infrared spectroscopy

The Co-PWA and Co-PWB samples were characterized by the Fourier-transform infrared spectroscopy (FTIR) method by the instrument PerkinElmer (Thermo Fisher, USA) using the KBr pellet technique with 32 scans and 4 cm^{-1} resolution, at a range of 4000 to 400 cm^{-1}.

2. 4. X-ray powder diffraction

The X-ray powder diffraction (XRPD) patterns of the Co-PWA and Co-PWB phases were obtained using a Rigaku Ultima IV automated diffractometer (Rigaku Corporation, Tokyo, Japan) with a Cu tube operating at 40 kV and 40 mA. The instrument utilizes a curved graphite monochromatic diffraction beam and Xe-filled proportional counter. The diffraction data were collected in the 2θ Bragg angle ranges from 3 to 90°, counting for 2° min^{-1} at every 0.05° steps. The divergence and receiving slits were fixed at 0.5° and 0.15 mm, respectively. The XRPD measurements were performed *ex situ* at room temperature (23 °C) in a stationary sample-holder. The diffractometer alignment was checked by means of a standard Si powder material (Rigaku Corporation, Tokyo, Japan). The Rietveld refinement method and the Fullprof program [27] were further carried out to calculate the unit cell parameters of Co-PWB bronze, according to the procedure described elsewhere [28-30].

2. 5. Scanning electron microscopy - energy dispersive X-ray spectroscopy study

The Co-PWA and Co-PWB samples were first gold-coated, whose morphology, microstructure and chemical composition were studied by scanning electron microscopy (SEM) equipped with an energy dispersive X-ray spectrometer (EDS) using a JEOL 840A instrument (JEOL Ltd., Tokyo, Japan).

2. 6. Electrochemical measurements

Suspensions of the Co-PWA and Co-PWB samples as the active material (85 %), carbon black (10 %; Cabot, Boston, USA) as a conductivity levelling additive, and polyvinylidene fluoride (PVDF; Sigma Aldrich, USA) as the binder (5 %) in the N-methyl-2-pyrrolidone solvent (Carl ROTH, Germany), were used to obtain working electrodes for electrochemical experiments. After being homogenized in an ultrasonic bath, the 10 µl of suspension was pasted on a glassy carbon (GC) electrode, as an electrically conducting support. To evaporate the solvent, the paste was dried for 4 h at 120 °C in a vacuum oven. At room temperature (23 °C), cyclic voltammetry (CV) tests were conducted in a three-electrode cell utilising a Gamry PCI4/300 Potentiostat/Galvanostat (Gamry instruments, Philadelphia, USA). A three-electrode system was used, made of a: (i) working glassy-carbon electrode (GC), (ii) counter electrode (broad-platinum foil) and (iii) saturated-calomel electrode (SCE) (reference electrode). A saturated aqueous solution of $LiNO_3$ (6 M, Carl ROTH, Germany) was used as an electrolyte. The active masses pasted on the glassy-carbon electrodes (working electrodes) of Co-PWA and Co-PWB applied were 1.02 and 0.935 mg, respectively. The masses of cathode materials were determined by multiplying the mass of dried suspensions on electrodes by 0.85.

Chronopotentiometry was carried out by use of three current densities: 1000, 2000 and 3000 mA g^{-1}, in the same three electrode system in the voltage range of -0.9 to 0.7 V *vs.* SCE. The pasted mass on the glassy carbon electrode of the electrode material Co-PWB was 0.00085 g determined as described above. The electrode was manually prepared in the same manner as previously described for cyclic voltammetry.

3. RESULTS AND DISCUSSION

3.1. Thermal characterization

Figure 2 presents the results obtained from the thermogravimetric analysis (TGA), as well as the differential thermal analysis (DTA), *i.e.* the TG and DT curves of $CoHPW_{12}O_{40}\times nH_2O$ (Co-PWA) from room temperature (25 °C) to 900 °C. The DT curve of Co-PWA shows three endothermic peaks at approximately 85, 125 and 185 °C, with an exothermic peak at 588 °C (see Fig. 2). The three endothermic peaks found in the DT curve of Co-PWA at low temperatures may be attributable to the physisorbed (up to ~100 °C) and crystal (up to ~450 °C) water liberation [31]. The H_2O content within the Co-PWA salt was estimated from the total TG weight loss of ~8.39 wt.% between room temperature and ~450 °C. Such weight loss corresponds to the calculated water content of *ca.* 15 moles of H_2O in the salt structure, which agrees with the $CoHPW_{12}O_{40}\times 15H_2O$ composition. Further, the solid-solid structural phase transformation from the anhydrous heteropoly Co-PWA salt to the Co-doped phosphate tungsten bronze was determined through the exothermic reaction, which occurred at 588 °C.

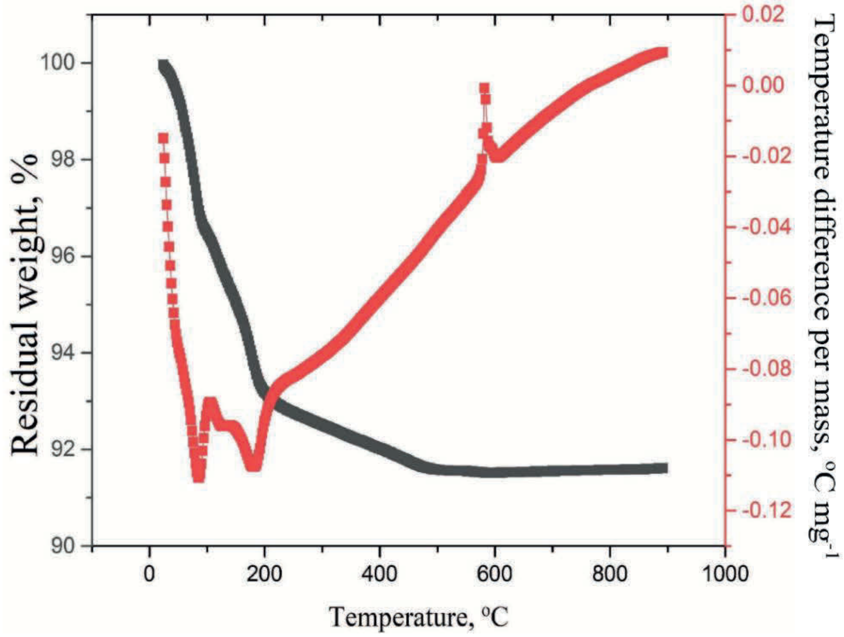

Figure 2. TGA (full line) and DTA (dashed line) curves of $CoHPW_{12}O_{40}\times nH_2O$

3. 2. Structural characterization

3. 2. 1. Comparison of cobalt tungsten doped salt and cobalt tungsten-phosphate bronze

FTIR spectra of the Co-PWA salt and Co-PWB bronze are presented in Figure 3. Table 1 presents assigning of FTIR bands for Co-PWA salt and Co-PWB bronze.

Table 1*. The characteristic FTIR bands of Co-PWA and Co-PWB*

Co-PWA		Reference	Co-PWB		Reference
Wavenumber, cm^{-1}	Assignation		Wavenumber, cm^{-1}	Assignation	
3457 vs	ν_3 (H_2O)	[32]	1118 m	ν_3 (PO_4)	[21]
1732 sh	ν_4 (H_3O^+)	[32,33]	904 sh	ν (W-O-W)	[32,34]
1616 m	ν_2 (H_2O)	[32]	766 vs	ν (W-O-W)	[34]
1075 s	ν_3 (PO_4)	[13,32,34]	~400	ν_4 (PO_4)	[32]
976 s	ν_1 (PO_4)	[13]			
893 m	ν (W-O-W)	[32,34]			
797 s	ν (W-O-W)	[34]			
594 w	ν_4 (PO_4)	[13]			

Marks: vs-very strong, s-strong, m-medium, w-weak, sh-shoulder, ν characteristic vibrations of WO_6 octahedron, ν_1-symmetric stretching, ν_2 bending, ν_3-antisymmetric stretching, ν_4-bending

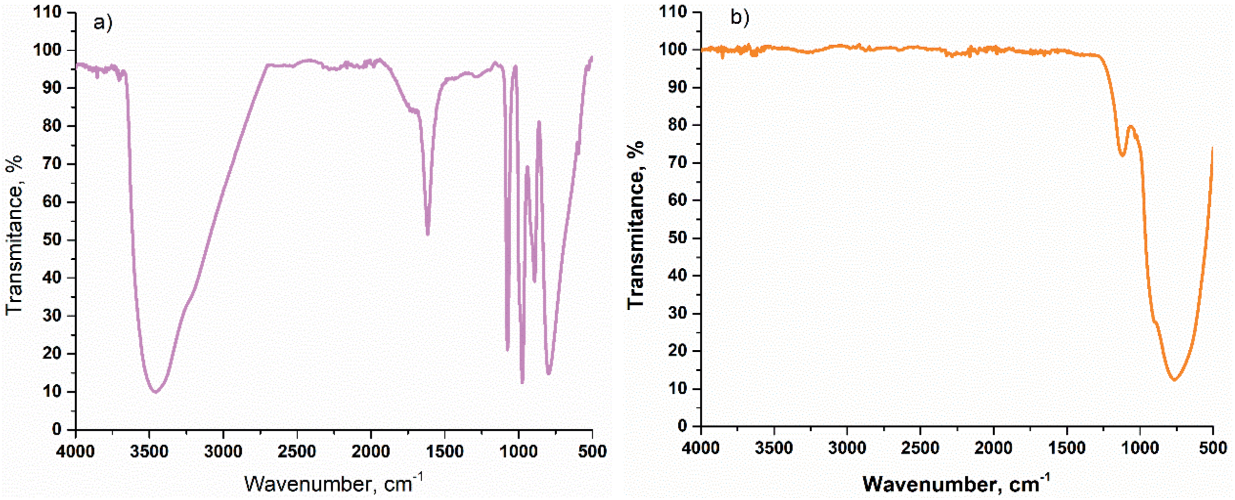

***Figure 3.** FTIR spectra of: a) Co-PWA and b) Co-PWB*

The FTIR spectrum of cobalt-doped heteropoly salt, Co-PWA, shows characteristic vibrational modes associated with the Keggin structure [13], which contain displacements or changes in intensity due to cobalt doping. Characteristic bands for the H_2O molecule are found at wavenumbers in the Co-PWA infra-red spectrum (Table 1): v_1 = 3457 cm^{-1} and v_2 = 1616 cm^{-1} [32]. The shoulder present in the higher wavenumber region (~1732 cm^{-1}) of the bands corresponding to the bending vibration of H_3O^+ ion [32] was also evident in Fe-PWA [21]. Typical vibrations of PO_4 tetrahedra are bands placed at wavenumbers in the Co-PWA spectrum: v_3 = 1075 cm^{-1} [13,32,34], v_1 = 976 cm^{-1} [13] and v_4 = 594 cm^{-1} [13]; while the bands characteristic for vibration of the WO_6 octahedron are located at wavenumbers in the Co-PWA spectrum: v = 893 cm^{-1} [32,34] and v = 797 cm^{-1} [34]. The characteristic vibrational modes of the PO_4 tetrahedron and WO_6 octahedron were reported to be positioned at similar wavenumbers in the FTIR spectra for PWA [13].

After the thermal treatment of the Co-PWA salt, the FTIR spectrum displayed evident changes obviously due to the Co-PWB formation. The phase transformation related to the collapse of the Keggin's structure (*i.e.* complete liberation of water molecules and rearrangement of PO_4 and WO_6 units) and formation of Co-PWB bronze are shown in Figure 3b and Table 1. The band positioned at v_3 = 1118 cm^{-1} in the Co-PWB spectrum is associated with the characteristic vibration of PO_4 tetrahedron [21]; while the shoulder at v = 904 cm^{-1}, and a very strong band at v = 766 cm^{-1} are associated with characteristic vibrations of WO_6 octahedron [34]. The band positioned at ~400 cm^{-1} corresponds to the characteristic vibration of the PO_4 unit [32]. A comparable spectrum was also obtained for another reported bronze Fe-PWB [21].

3. 2. 2. XRPD characterization

XRPD patterns of Co-PWA and Co-PWB phases are presented at Figure 4 and Table 2, while the calculated unit-cell parameters are shown in Table 3.

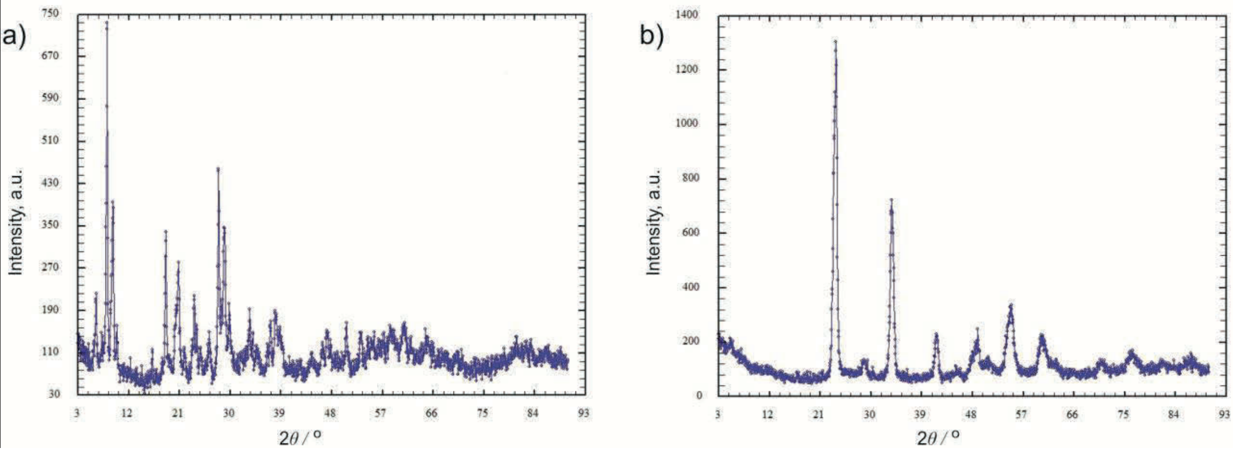

***Figure 4.** XRPD patterns determined for: a) Co-PWA; and b) Co-PWB*

Table 2. *Determined interplanar spacings (d_{det}), and intensities (I_{det}) of the Co-PWA and Co-PWB phases (note: data for monoclinic PWB [13] are also presented for comparison).*

Co-PWA		Co-PWB		monoclinic PWB		
d_{det} / nm*	I_{det} / %	d_{det} / nm*	I_{det} / %	d_{det} / nm	I_{det} / %	hkl
1.433(8)	18	/	/	0.384	41	0 0 2
1.078(1)	100	0.3738(2)	100	0.375	100	0 2 0
0.9531(6)	49	0.3107(4)	4	0.311	6	-1 1 2
0.890(4)	10	0.2660(1)	54	0.268	40	-2 0 2
0.4775(6)	44	/	/	0.264	26	2 0 2
0.4254(3)	29	0.2170(2)	14	0.217	14	-2 2 2
/	/	/	/	0.201	2	2 1 3
0.3771(6)	20	/	/	0.192	3	0 0 4
0.3191(2)	56	0.1866(3)	8	0.187	11	-1 0 4
0.3071(2)	38	0.1798(7)	2	0.181	4	-1 1 4
0.2985(6)	12	0.1678(1)	18	0.167	15	-2 1 4
0.2676(6)	6	0.1533(2)	10	0.153	9	2 4 2
0.234(1)	10	/	/	0.149	3	-1 4 3
/	/	0.12478(9)	4	/	/	/

*The numbers in parentheses are the estimated standard deviations and refer to the last significant number

Table 3. *Calculated unit cell parameters of Co-PWB compared to the reported values for PWB [13]*

	Co-PWB*	PWB*
a_0 / nm	0.745(2)	0.7325(6)
b_0 / nm	0.744(2)	0.7516(9)
c_0 / nm	0.759(1)	0.7686(9)
β_0 / °	89.5(2)	90.79(5)
V_0 / nm^3	0.421(2)	0.4231(9)

*The numbers in parentheses are the estimated standard deviations and refer to the last significant number

Concurring with our previous results [13,21], these two phases are disparate, confirming the solid-solid structural phase transformation observed by the thermal analysis (Fig. 2) and FTIR results (Fig. 3 and Table 1). According to the herein obtained data and bronze data reported elsewhere [13,21,24,25], it could be reasonably assumed that all these compounds are iso-structural, *i.e.* that Co-PWB crystallized in the monoclinic crystallographic system.

Table 3 presents the calculated Co-PWB unit-cell parameters including those reported for un-doped PWB bronze. From these results, it is obvious that the entrance of Co ions into the PWB structure resulted in an increase in the a_0 axis, while all the other parameters were decreased (*i.e.* axes b_0 and c_0, angle β_0 and volume V_0). Co-PWB has almost mutually identical a_0 and b_0 axes (similarly to the Fe-PWB [21]); however, the significant deviation of the angle β_0 from 90° excludes in this case the possibility for its crystallization in a tetragonal crystallographic system.

3. 3. Morphological characterization

Figures 5a and 5c present morphology of the materials Co-PWA salt and Co-PWB bronze. Cracks in the agglomerated plates for both compounds are most probably the consequence of the synthesis procedure by which water evaporates.

To detect chemical elements, EDS line scans were carried out for both samples, as presented in Figures 5b and 5d. The chemical elements: O, W, Co and P were detected in both, where differing atomic and weight concentrations of W, O, P and Co were observed. The reason for such behavior most probably might lie in the inhomogeneous distribution of the particles in the samples studied. Nevertheless, these results confirm the entering of Co into the both PWA and PWB compounds, which is in line with the above-discussed FTIR and XRPD studies.

3. 4. Electrochemical characterization

3. 4. 1 Cyclic voltammetry measurements

Often used as a rapid analytical method, cyclic voltammograms (CVs) were obtained at a scan rate of 20 mV s^{-1} for all samples measured within their potential corresponding electrochemical stability windows (+0.09 to -0.85 V *vs.* SCE for Co-PWA; Fig. 6a; and +0.6 to -1.0 V vs. SCE for Co-PWB; Figs. 6b,c), and a 5 mV s^{-1} was also applied for Co-PWB (Fig. 6d).

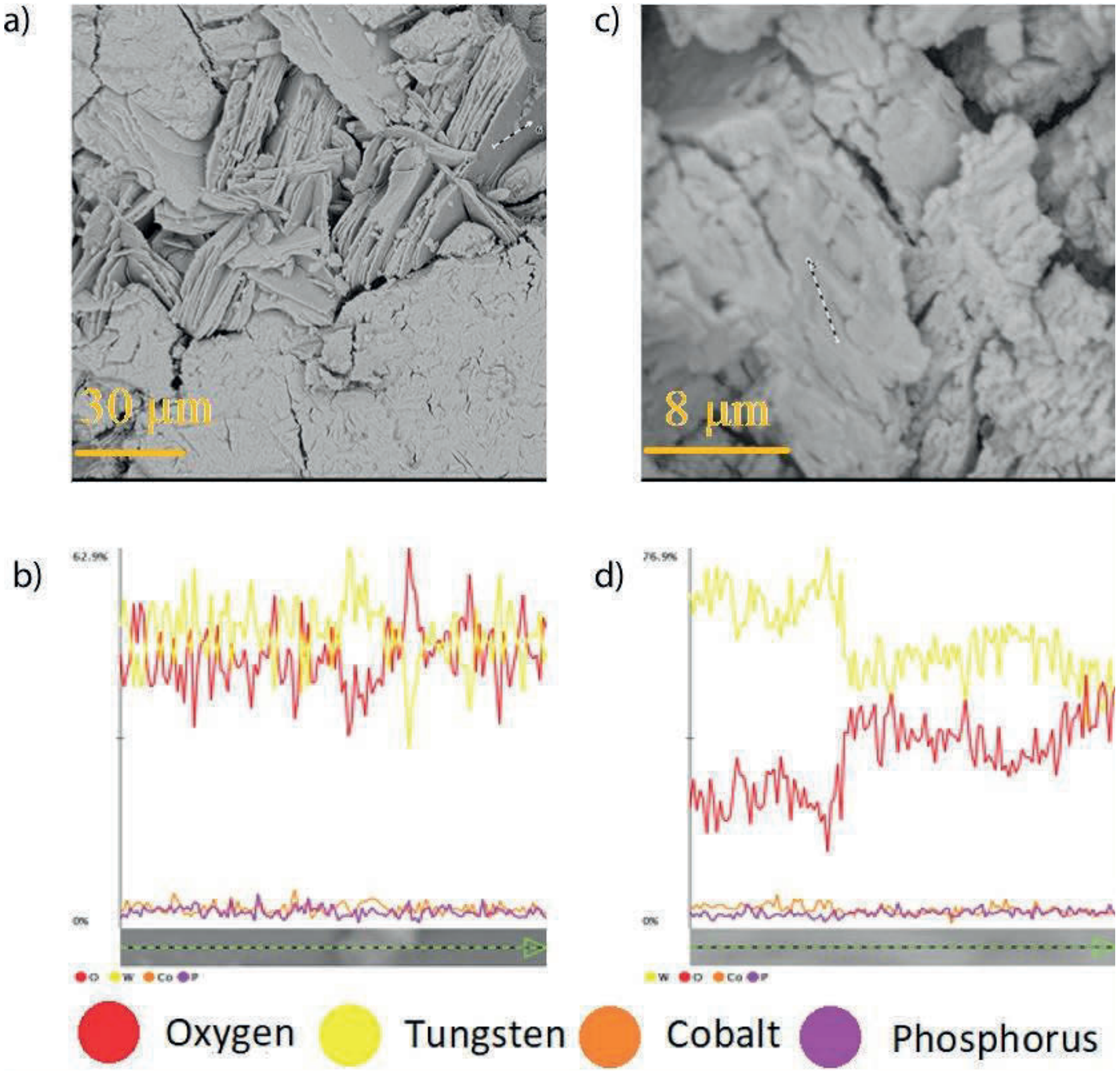

Figure 5. *SEM-EDS scanning: a) SEM presenting the entire region and a line scan (marked in black and white arrows) of Co-PWA; b) the combined EDS line scan of Co-PWA; c) SEM presenting the entire region and a line scan (marked in black and white arrows) of Co-PWB; d) the combined EDS line scan of Co-PWB. The Y axes correspond to atomic mass percents, while the X axes are mapping lines presented in Figures 5a) and 5c). For interpretation of the references to colour in this figure legend, the reader is referred to the web version of this article*

The Co-PWA CV (reduction during the 1st cycle) is composed of four ion insertion peaks at -0.2, -0.39, -0.56 and -0.74 V *vs.* SCE (Fig. 6a). A tentative explanation is that Li^+ ions entered the Co-PWA, thereby causing a formation of four distinct phases of $CoLi_x$-PWA salt. The first de-insertion process for Co-PWA was followed by anodic peaks positioned at -0.67 and -0.14 V *vs.* SCE. Deposition of the material over the ions insertion caused a significant distinction between the cathodic and anodic capacity. The formed unstable electrode material precipitated in an aqueous solution of $LiNO_3$ (see Supplementary Material, Fig. S1.) resulting in a low anode capacity, due to which there was not sufficient electrode material remaining on the glassy carbon electrode for the ions' de-insertion. As proven by the immersion of the electrode in an aqueous solution of $LiNO_3$, Co-PWA was not displaced from the working electrode into the electrolyte prior to the ions insertion (Supplementary Material, Fig. S1.). The insertion of ions, therefore, probably leads to the formation of $CoLi_x$-PWA salt unstable in the electrolyte. As previously determined, Fe-PWA exhibited the same behavior over the first cathode cycle in the same electrolyte [21]. Based on the results obtained, while demonstrating that the Co-PWA salt is not usable as an electrode material for aqueous Li-ion batteries, its redox activity deserves further examination in other electrolytes, especially in non-aqueous ones.

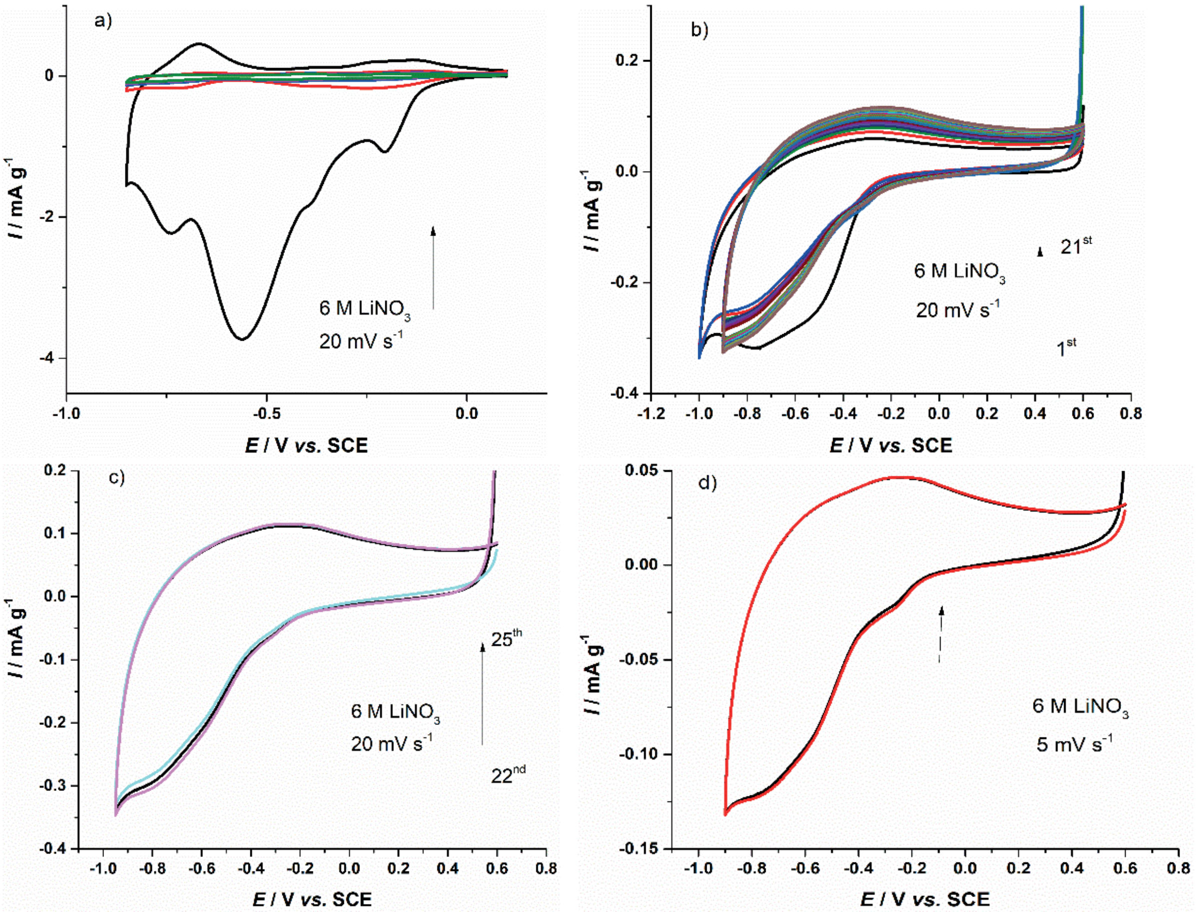

Figure 6. *Cyclic voltammetry measurements: a) CVs of Co-PWA; b) CVs of Co-PWB recorded at 20 mV s^{-1} 1st to 21st cycle; c) CVs of Co-PWB recorded at 20 mV s^{-1} 22nd to 25th cycle ; and d) CV obtained at a scanning rate of 5 mV s^{-1} for Co-PWB*

Compared to the four clearly visible peaks for ions insertion in Co-PWA, the structure of its corresponding bronze Co-PWB allows only two small and broad peaks (*i.e.* -0.26 and -0.74 V *vs.* SCE) when polarization rate was 5 mV s^{-1} (Fig. 6d), which are not visible at a higher polarization rate of 20 mV s^{-1} (Figs. 6b and 6c). The initial enhanced electrochemical activity of the Co-PWA salt compared to its thermally obtained bronze is likely a consequence primarily of: (i) different structures between the Co-PWA and Co-PWB compounds; and (ii) the presence of water in the Co-PWA structure, which is lacking in the Co-PWB structure, as unquestionably determined in the present studies (see Figs. 3 and 4; and Tables 1 and 2). Such a situation in Co-PWA obviously provides additional sites for ion-intercalation [31]. However, the potential intercalation of ions into Co-PWA makes it far less stable compared to its corresponding bronze Co-PWB. On the other hand, the stability of Co-PWB was achieved after 21st cycle, as observed in Figs. 6b and 6c. A higher cathode capacity compared to the anodic one for Co-PWB means that the insertion of ions is a more favorable process compared to de-insertion.

When doped, PWB metallic behavior becomes corrupted due to electrons filling the W-O-W hybridized π* conduction band [35-37] changing the metallic behavior of PWB from a semiconductor to an insulator. Consequently, all doped samples exhibit decreased electrical conductivity compared to the un-doped PWB sample. The lithium-doped bronzes (Li_3-PWB and Li_n-PWB) exhibit both: (i) sluggish kinetics of broad and barely visible peaks, as well as (ii) irreversible delithiation caused by structural transformation [26]. Similar forms of the CVs is noted for Fe-PWB [21], Co-PWB [this work], and Li_3-PWB [26]. Compared to Li^+ in Li_3-PWB, doping with more charged ions (*e.g.* Co^{2+} and Fe^{3+}), therefore, seemingly protects the bronze structure from transformation into its unstable form in $LiNO_3$ aqueous solution caused by ion insertion.

3. 4. 2. Chronopotentiometry measurements of cobalt tungsten-phosphate bronze

To simulate the charge and discharge of the electrode material as if in a battery, the chronopotentiometry method was applied for Co-PWB in a 6M aqueous solution of $LiNO_3$. The three rates of 1000, 2000 and 3000 mA g^{-1} were applied to charge and discharge the electrode material. The charge and discharge curves are presented in Figure 7a, while dependences of discharge capacities on the cycle number obtained for each current are presented in Figure 7b.

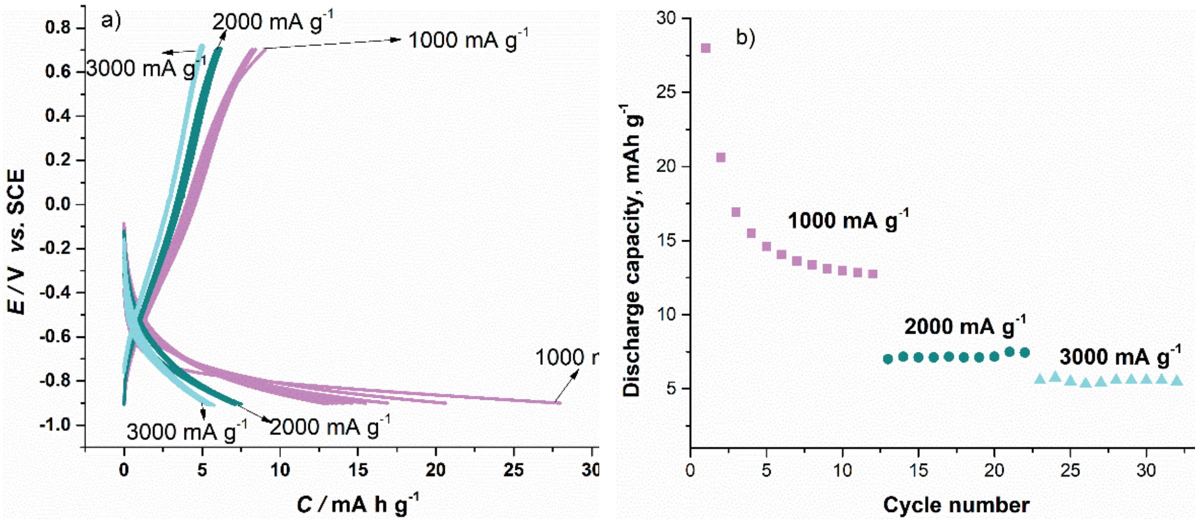

Figure 7. *Chronopotentiometry measurements: a) charging and discharging cycles of Co-PWB; and b) discharge capacity vs. cycle number of Co-PWB in an aqueous solution of 6 M $LiNO_3$*

According to the herein obtained results, the initial capacity for 1000 mA g^{-1} was ~28 mAh g^{-1}, while stabilization was achieved after the tenth cycle yielding a capacity of ~13 mAh g^{-1}. Compared to a reported study [26] in which the material PWB was examined, the initial capacity obtained was ~67 mAh g^{-1} and after stabilization reached ~25 mAh g^{-1} at a polarization rate of 100 mA g^{-1}; the results obtained indicate that the material Co-PWB has a potential for higher capacities at slower currents applied. In the present study, the capacity was stabilized just after the tenth cycle, although the literature [26] indicates that capacity stabilization may be achieved after one hundred cycles. Further, stabilization of the material was accomplished immediately when the currents applied were 2000 and 3000 mA g^{-1}, indicating that a stable structure was achieved over the charging and discharging processes under the application of such higher current rates. Therefore, chronopotentiometry showed that Co-PWB has a potential as an electrode material for aqueous Li-ion batteries.

4. CONCLUSION

This research has aimed to synthesize novel heteropoly materials Co-PWA salt and its bronze Co-PWB obtained by the thermal treatment of Co-PWA at an intermediate temperature (588 °C). The materials were characterized using XRPD, FTIR, SEM, EDS, cyclic voltammetry, as well as chronopotentiometry methods. The presence of Co was undoubtedly confirmed in both Co-PWA salt and Co-PWB bronze, thereby verifying their successful syntheses. Both cyclic voltammetry and chronopotentiometry yielded stable capacities. Based on the results obtained, Co-PWB might be a promising electrode material. The results obtained bridge the gap in the scientific literature on these and similar materials.

SUPPLEMENTARY MATERIAL

Additional data are available electronically at https://www.ache-pub.org.rs/index.php/HemInd/article/view/1384, or from the corresponding author on request.

Acknowledgement: *This work was financially supported by the Ministry of Science, Technological Development and Innovation of the Republic of Serbia (Grants No. 451-03-66/2024-03/200026, 451-03-66/2024-03/200051, 451-03-66/2024-03/200146 and 451-03-65/2024-03/200126) and the Faculty of Science and Mathematics, University of Priština in Kosovska Mitrovica (Grant No. IJ-2301). The authors thank Dr Zoran Nedić for his useful help in preparing the materials in the bronze synthesis. M.P. acknowledges the support of the EU: the EIC Pathfinder Challenges 2022 call through the Research Grant 101115149 (project ARTEMIS), as well as the support of the Office of Naval Research Global through the Research Grant N62902-22-1-2024.*

REFERENCES

[1] Kamiya Y, Okuhara T, Misono M, Miyaji A, Tsuji K, Nakajo T. Catalytic chemistry of supported heteropolyacids and their applications as solid acids to industrial processes. *Catal Surv Asia.* 2008; 12: 101-113. https://doi.org/10.1007/s10563-008-9043-7

[2] Chikin AI, Chernyak AV, Jin Z, Naumova YS, Ukshe AE, Smirnova NV, Volkov VI, Dobrovolsky YA. Mobility of protons in 12-phosphotungstic acid and its acid and neutral salts. *J Solid State Electrochem.* 2012; 16: 2767-2775. https://doi.org/10.1007/s10008-012-1687-6

[3] Kourasi AM, Wills RGA, Shah AA, Walsh FC. Heteropolyacids for fouel cell applications. *Electrochim Acta.* 2014; 127: 454-466. https://doi.org/10.1016/j.electacta.2014.02.006

[4] Imofeeva MN, Maksimov GM, Likholobov VA. Acidity of solutions of heteropoly acids with various structures and compositions. *Kinetic Catal.* 2001; 42: 30-34. https://doi.org/10.1023/A:1004892411282

[5] Kima JD, Hayashi S, Mori T, Honma I. Fast proton conductor under anhydrous condition synthesized from 12-phosphotungstic acid and ionic liquid. *Electrochim Acta.* 2007; 53: 963-967. https://doi.org/10.1016/j.electacta.2007.08.009

[6] Schneea J, Devredb F, Gaigneauxb EM, Vimonta A, Assessing the dispersion of supported $H_3PW_{12}O_{40}$ catalysts: No longer a hurdle thanks to in situ IR upon pyridine adsorption. *Appl Catal.* 2019; 578: 116-121. https://doi.org/10.1016/j.apcata.2019.03.022

[7] Brown GM, Noe-Spirlet MR, Busing WR, Levy HA. Dodecatungstophosphoric acid hexahydrate, $(H_5O_2^+)_3(PW_{12}O_{40}^{3-})$. The true structure og Keggins pentahydrate from single-crystal X-ray and neutron diffraction data. *Acta Cryst.* 1977; B33: 1038-1046. https://doi.org/10.1107/S0567740877005330

[8] Spirlet MR, Busing WR. Dodecatungstophosphoric acid-21-water by neutron diffraction. *Acta Cryst.* 1978; 34(3): 907-910. https://doi.org/10.1107/S0567740878004306

[9] Kremenović A, Spasojević-de Biré A, Dimitrijević R, Sciau P., Mioč UB, Colomban Ph. Keggin's ion structural modification and expansion of dodecatungstophosphoric acid hexahydrate induced by temperature treatment: In situ X-ray powder diffraction and Raman investigations. *Solid State Ion.* 2000; 132: 39-53. https://doi.org/10.1016/S0167-2738(00)00727-X

[10] Davidović M, Čajkovski T, Colomban Ph, Mioč UB, Likar-Smiljanić V, Čajkovski D, Biljić R, Nedić Z. The influence of monovalent and bivalent cations on the electrical properties of 12-tungstophosphoric acid salts. *Solid State Ion.* 2005; 176: 2881-2885. https://doi.org/10.1016/j.ssi.2005.09.020

[11] Kulesza PJ, Rutkowska IA, Janiszewska C, Noto VD, Vezzu K, Negro E. Development and characterization of polyoxometallate-based systems for aqueous redox flow batteries. *Meet Abstr.* 2022; MA2022-01: 1999. https://doi.org/10.1149/MA2022-01481999mtgabs

[12] Ammam M, Fransaer J. Ionic liquid-heteropolyacid: Synthesis, characterization, and supercapacitor study of films deposited by electrophoresis. *J Electrochem Soc.* 2011; 158: A14. https://doi.org/10.1149/1.3507254

[13] Mioč UB, Dimitrijević RŽ, Davidović M, Nedić ZP, Mitrović MM, Colomban Ph. Thermally inducted phase transformations of 12-tungstophosphoric acid 29-hydrate:synthesis and characterization of PW_8O_{26}-type bronzes. *J Mater Sci.* 1994; 29: 3705-3718. https://doi.org/10.1007/BF00357338

[14] Dimitrijević RŽ, Colomban Ph, Mioč UB, Nedić Z, Todorović MR, Tjapkin N, Davidović M. Synthesis, conductivity and structural characterization of phosphorous bronzes originating from heteropolyacids. Relation with similar proton containing phases. *Solid State Ion.* 1995; 77: 250-256. https://doi.org/10.1016/0167-2738(94)00310-O

[15] Maksimović TV, Maksimović JP, Joksović LjG, Nedić ZP, Pagnacco MC. Oscilatorna reakcija kao sistem detektor za dopirane i nedopirane fosfat-volframove bronze. *Hem Ind.* 2018; 72(5): 275-283. (in Serbian) https://doi.org/10.2298/HEMIND180402018M

[16] Sweedler AR, Raub ChJ, Matthias BT. Superconductivity of the alkali tungsten bronzes. *Phys Lett.* 1965; 15(2): 108-109. https://doi.org/10.1016/0031-9163(65)91292-8

[17] Brusetti R, Bordet P, Bossy J, Schober H, Eibl S. Superconductivity in the tungsten bronze Rb_xWO_3 ($0.20 \leqslant x \leqslant 0.33$) in connection with its structure, electronic density of states, and phonon density of states. *Phys Rev.* 2007; B76: 174511. https://doi.org/10.1103/PhysRevB.76.174511

[18] Yoon S, Jo C, Noh SY, Lee CW, Song H, Lee J. Development of a high-performance anode for lithium ion batteries using novel ordered mesoporous tungsten oxide materials with high electrical conductivity. *PCCP.* 2011; 13: 11060-11066. https://doi.org/10.1039/C1CP20940J

[19] Wasserman K, Pope MT, Salmen M, Dann JN, Lunk HJ. Thermal degradation of polyoxotungstates-an effective method for the preparation of tungsten bronzes. *J Solid State Chem.* 2000; 149: 378-383. https://doi.org/10.1006/jssc.1999.8556

[20] Dong X, Lu Y, Wu Z, Liu X, Tong Y. Photochromic hierarchical $(NH_4)_xWO_3$ nanocrystals with bronze tunnel structure for energy-saving windows. *Chem Eng J.* 2023; 477: 147064. https://doi.org/10.1016/j.cej.2023.147064

[21] Acković J, Micić R, Nedić Z, Petrović T, Senćanski J, Pagnacco M, Tančić P. Synthesis, characterization and electrochemical properties of iron doped phosphate tungsten heteropoly acid (Fe-PWA) and its bronze (Fe-PWB): Comparative study. *Sci Sinter.* 2024; 56: 367-380. https://doi.org/10.2298/SOS230812053A

[22] Pagnacco M, Marković S, Potočnik J, Krstić V, Tančić P, Mojović M, Mojović Z. The influence of electrode constituents on hydrogen evolution reaction on phosphate W-and Mo bronze based electrodes. *J Electrochem Soc.* 2022; 169(10): 106508. https://doi.org/10.1149/1945-7111/ac96ab

[23] Maksimović JP, Maksimović TV, Nedić ZP, Pagnacco MC. The minor influence of calcium doped phosphate tungsten bronze on the Briggs-Rauscher reaction dynamics. *Contemp Mater.* 2018; 184-189. https://doi.org/10.7251/COMEN1802184M

[24] Maksimović TV, Maksimović JP, Tančić PI, Potkonjak NI, Nedić ZP, Joksović LjG, Pagnacco MC. A possible connection between phosphate tungsten bronzes properties and Briggs-Rauscher oscillatory reaction response. *Sci Sinter.* 2021; 53: 223. https://doi.org/10.2298/SOS2102223M

[25] Maksimović T, Tančić P, Maksimović J, Mara D, Ilić M, Van Deun R, Joksović Lj, Pagnacco M. Novel cerium and praseodymium doped phosphate tungsten bronzes: Synthesis, characterization, the behavior in the Briggs-Rauscher reaction and photoluminescence properties. *Opt Mater.* 2023; 143: 114125. https://doi.org/10.1016/j.optmat.2023.114125

[26] Vujković M, Nedić Z, Tančić P, Aleksić OS, Nikolić MV, Mioč U, Mentus S. Electrochemical lithiation/delithiation kinetics and capacity of phosphate tungsten bronze and its chemically pre-lithiated derivatives aqueous solutions. *J Mater Sci.* 2016; 51: 2481-2489. https://doi.org/10.1007/s10853-015-9560-5

[27] Rodriguez-Carvajal, J. Program Fullprof (Computer software). In Proceedings of the Abstract of 15th Conference of International Union of Crystallography, Satellite Meeting on Powder Diffraction, Toulouse, France, July 16-19th 1990; p. 127.

[28] Tančić P, Dimitrijević R, Poznanović M, Pačevski A, Sudar S. Crystal structure and chemical composition of ludwigite from Vranovac ore deposit (Boranja Mountain, Serbia). *Acta Geol Sin-Engl.* 2012; 86(6): 1524-1538. https://doi.org/10.1111/1755-6724.12020

[29] Tančić P, Kremenović A, Vulić P. Structural dissymmetrization of optically anisotropic $Grs_{64\pm1}Adr_{36\pm1}Sps_2$ grandite from Meka Presedla (Kopaonik Mt., Serbia). *Powder Diffr.* 2020; 35(1): 7-16. https://doi.org/10.1017/S0885715619000897

[30] Tančić P, Kremenović A. Rietveld crystal structure refinement of a natural rhombohedral grossular-andradite garnet from Serbia. *Geol Q.* 2022; 66(7): 1639. http://dx.doi.org/10.7306/gq.1639

[31] Mioč U, Davidović M, Tjapkin N, Colomban Ph, Novak A. Equilibrium of the protonic species in hydrates of some heteropolyacids at elevated temperatures. *Solid State Ion.* 1991; 46: 103-109. https://doi.org/10.1016/0167-2738(91)90136-Y

[32] Ratajczak H, Barnes AJ, Bielański A, Lutz HD, Müller A, Pope MT. Vibrational Spectroscopy of Heteropoly Acids. In: Pope, MT, Müller A. (eds) Polyoxometalate Chemistry From Topology via Self-Assembly to Applications. *Springer Dordrecht*. 2001; 101-116. https://doi.org/10.1007/0-306-47625-8_8

[33] Jose da Silva M, Macedo de Oliveira C. Catalysis by Keggin heteropolyacid salts. *Curr Catal.* 2018; 7: 26-34. https://doi.org/10.2174/2211544707666171219161414

[34] Rocchiccioli-Deltcheff C, Fournier M, Franck R, Thouvenot R, Vibrational investigations of polyoxometalates. 2. Evidence for anion-anion interactions in molybdenum(VI) and tungsten(VI) compounds related to the keggin structure. *Inorg Chem.* 1983; 22: 207-216. https://doi.org/10.1021/ic00144a006

[35] Martinez-de la Cruz A, Rodriguez FEL, Rodriguez JI. Electrochemical lithium insertion in the phosphate tungsten bronze $P_8W_{12}O_{52}$. *Solid State Ion.* 2005; 176: 2625-2630. https://doi.org/10.1016/j.ssi.2005.08.009

[36] Martínez-de la Cruz A, Rodríguez FEL. Electrochemical lithium insertion in $(PO_2)_4(WO_3)_{2m}$ ($2\leq m\leq 10$): Relation among the electrochemical insertion process and structural features. *Electrochim Acta.* 2009; 54: 3176-3183. https://doi.org/10.1016/j.electacta.2008.11.056

[37] Wang E, Greenblatt M. Lithium and sodium insertion reactions of phosphate tungsten bronzes. *J Solid State Chem.* 1987; 68: 38-44. https://doi.org/10.1016/0022-4596(87)90282-9

Sinteza, karakterizacija i elektrohemijske osobine kobaltom dopirane fosfat volframove heteropoli kiseline i njene bronze

Jovana S. Acković[1], Tamara Petrović[2], Jelena Senćanski[3*], Aleksandar Mijatović[4], Stevan Blagojević[3], Pavle Tančić[5], Ružica Micić[1] i Maja Pagnacco[5]

[1]Univerzitet u Prištini, Prirodno-matematički fakultet, Departman za hemiju, Kosovska Mitrovica, Srbija.
[2]Univerzitet u Beogradu, Fakultet za fizičku hemiju, Beograd, Srbija.
[3]Univerzitet u Beogradu, Institut za opštu i fizičku hemiju, Beograd, Srbija.
[4]Univerzitet u Beogradu, Rudarsko-geološki fakultet, Beograd, Srbija.
[5]Univerzitet u Beogradu, Institut za hemiju, tehnologiju i metalurgiju, Katedra za katalizu i hemijsko inženjerstvo, Beograd, Srbija

(Naučni rad)

Izvod

Heteropoli kiseline i njihova jedinjenja su fascinantna klasa multifunkcionalnih materijala koji se koriste u različitim naučnim oblastima: medicini, magnetizmu, katalizi, nelinearnoj optici kao i u elektrohemiji gde se primenjuju kao materijali za baterije. U ovoj studiji je polazna tačka volfram-fosfatna heteropoli kiselina iz koje je sintetisana i karakterisana njena kobaltova so (Co-PWA) i kobaltom dopirana volfram-fosfatna bronza (Co-PWB). Termička analiza je korišćena za određivanje faznog prelaza Co-PWA soli u Co-PWB bronzu koji se odvija na 588 °C. Ova temperatura je korišćena za žarenje Co-PWA da bi se sintetisala Co-PWB. Oba uzorka su dalje karakterisana korišćenjem infracrvene spektroskopije sa Furijeovom transformacijom (engl. Fourier transform infrared spectroscopy), difrakcije rendgenskih zraka na prahu (engl. X-ray powder diffraction) i skenirajuće elektronske mikroskopije koja sadrži energetsku disperzivnu rendgensku spektroskopiju (engl. scanning electron microscopy using an energy dispersive X-ray spectroscopy), kao i korišćenjem elektrohemijskih ispitivanja. Prisustvo kobalta je nedvosmisleno pokazano i u Co-PWA i Co-PWB, pri cemu je potvrdjeno uspešno dopiranje. Za elektrohemijska ispitivanja korišćene su ciklična voltametrija kao "brza" tehnika i metoda hronopotenciometrije radi simuliranja punjenja i pražnjenja baterije. Ciklična voltametrija je izmerila nestabilan i mali kapacitet za Co-PWA i stabilan za Co-PWB u vodenom rastvoru $LiNO_3$. Razlog pada kapaciteta kod Co-PWA je nestabilnost ove soli u navedenom elektrolitu. Zbog stabilnog kapaciteta Co-PWB dobijenim merenjem cikličnom voltametrijom, ovaj material je podvrgnut hronopotenciometrijskom punjenju i pražnjenju pri strujama 1000, 2000 i 3000 mA g^{-1}. Ovom metodom je pokazan stabilan kapacitet pri svakoj od primenjenih struja, što ga čini atraktivnim elektrodnim materijalom za vodene Li-jonske baterije. Dobijeni rezultati dopunjuju naučnu literaturu koja se bavi ispitivanjem sličnih materijala i doprinose boljem razumevanju karakteristika dopiranih kiselina i njihovih bronzi različitim metalima.

Ključne reči: ciklična voltametrija, hronopotenciometrija, reakcije interkalacije/deinterkalacije litijuma, Li jonske baterije

Efficiency evaluation of a natural material for removal of cationic oxazine and anionic azo dyes from aqueous solutions

Asma Boudaoud[1], Chifaa Ad[2], Mebrouk Djedid[2], Mokhtar Benalia[2], Mounira Guermit[1] and Soltani Amel[3]

[1]Laboratory of Process Engineering, Materials and Environmental, Department of Common Trunk Science and Technology; Faculty of Technology, Amar Telidji University of Laghouat, Laghouat, Algeria
[2]Laboratory of Process Engineering, Materials and Environmental, Department of Process Engineering, Faculty of Technology, Amar Telidji University of Laghouat, Laghouat, Algeria
[3]Higher Normal School of Laghouat, Laghouat, Algeria

Abstract

The current work involves studying the adsorption process of brilliant cresyl blue (BCB) and methyl orange (MeO) dyes using local pumpkin seed husks (LPSH). The LPSH adsorbent was analysed by using Fourier transform infrared spectroscopy, scanning electron microscopy with energy dispersive x-ray spectroscopy, X-ray diffraction and Brunauer-Emmett-Teller analyses. The descriptive analysis of the morphology of LPSH revealed a heterogeneous surface, while the structural analysis showed the presence of functional groups typical of lignocellulosic structures and it was confirmed that the mesoporous surface of the adsorbent had a specific surface area of ~1.53 $m^2 g^{-1}$. The adsorption isotherm studies suggested that the Langmuir model best described the adsorption of MeO, while the Freundlich model is more suitable for describing the adsorption of BCB. According to the thermodynamic analyses, the adsorption of BCB was exothermic and spontaneous, whereas the adsorption of MeO was endothermic and non-spontaneous. The results of evaluating the efficiency of the LPSH adsorbent showed that the maximum adsorption capacities are ~81 mg g^{-1} for the BCB dye and ~8.2 mg g^{-1} for the MeO dye.

Keywords: Brilliant cresyl blue; methyl orange; adsorption; pumpkin seed husks; synthetic dye solutions.

TECHNICAL PAPER

UDC: 547.556.33-045.38

Hem. Ind. **79(2)** 115-125 (2025)

1. INTRODUCTION

Water quality can be compromised due to the presence of harmful substances originating from various sources, such as industrial discharges, agricultural runoff, and sewage. The resulting pollution can be classified based on the type of pollutants: chemical, biological, or physical, along with the source and the amount of water affected. To understand how polluted the water is, it is necessary to determine concentrations of the contaminants and how they impact different uses of the water (*e.g.* for drinking), as well as aquatic life, and recreational activities [1]. Also the pollutants can be divided into several categories, such as natural and synthetic pollutants [2-4].

Synthetic dyes such as Brilliant cresyl blue and methyl orange are compounds used in many industrial sectors such as the paper industry, printing, natural and synthetic textiles production, leather and fur industry, plastics manufacturing, and pharmaceutical industry, as well as in research laboratories [5,6]. These dyes are discharged with liquid effluents into streams without prior treatment. High toxicity of these pollutants and their non-biodegradability contribute to environmental degradation [7] imposing the need for treatment of this wastewater.

Work on the removal of emerging pollutants by biomaterials obtained from agricultural waste has yielded promising results. Thus, these precursors from agriculture constitute alternative materials, both economic and eco-friendly [8-10]. In addition, enormous amounts of waste are generally available from farms and agro-industrial facilities in many countries, where agricultural residues notably represent a significant unused resource.

Corresponding author: Asma Boudaoud, Amar Telidji University of Laghouat, Laghouat, Algeria
E-mail: a.boudaoud@lagh-univ.dz

Paper received: 26 November 2023; Paper accepted: 27 March 2025; Paper published: 1 Mayl 2025.
https://doi.org/10.2298/HEMIND231126006B

This research aims to evaluate local pumpkin seed husks (LPSH) as a naturally adsorbing material for removing cationic dye brilliant cresyl blue and anionic dye methyl orange from synthetic wastewater by a batch adsorption process.

For this purpose, this study includes the examination of raw LPSH characteristics using Fourier transform infrared spectroscopy (FTIR), scanning electron microscopy with energy dispersive X-ray spectroscopy (SEM-EDX), X-ray diffraction (XRD), and Brunauer-Emmett-Teller (BET) and Barrett-Joyner-Halenda (BJH) methods. Also, effects of various operational variables have been studied such as pH value of the solution, contact time, initial concentration, and temperature. This work also includes investigations of the most significant isotherm models, as well as thermodynamic parameters, to accurately define the mechanism and behaviour of the dye adsorption.

1. MATERIALS AND METHODS

2. 1. Materials

Chemical reagents used in this study were cationic oxazine dye Brilliant cresyl blue (BCB: $C_{34}H_{40}Cl_4N_6O_2Zn$, purity >95 %), anionic azo dye: methyl orange (MeO: $C_{14}H_{14}N_3NaO_3S$, purity >98 %), sodium hydroxide (NaOH, purity > 80% and sulfuric acid (H_2SO_4, purity >95 %), all obtained from Fluka and Sigma-Aldrich (Germany).

2. 2. Preparation of pumpkin seed husks

Local pumpkin seed husks (*Cucurbita moschata*) from Laghouat, Algeria, were selected as the adsorbent for this investigation. It was prepared by using a simple method that involved washing with distilled water, grinding, sifting, and drying for 24 h at 105 ± 5 °C. A fine pumpkin seed husks powder with a particle size of ≤ 800 µm was obtained as a result of this method [11].

2. 3. Characterization of pumpkin seed husks

Structural and morphological characteristics of LPSH samples have been evaluated using the Fourier transfer infrared (FTIR) spectroscopy (4200-FTIR JASCO, Japan), scanning electron microscopy combined with energy dispersive X-ray (SEM-EDX, Thermo Scientific™ Quattro, United States), and X-ray diffraction (XRD, Philips PW3373, United Kingdom). Specific surface area and porosity parameters were determined by using the Brunauer-Emmett-Teller (BET) and Barrett-Joyner-Halenda (BJH) methods (ASAP 2020 Plus Version 2.00–Malvern Panalytical, Malvern, United States). One sample was prepared for each test.

2. 4. Preparation of dye solutions

Dyes used in this study were BCB and MeO (Fig. 1), with the chemical formula: $C_{34}H_{40}Cl_4N_6O_2Zn$ and $C_{14}H_{14}N_3NaO_3S$, respectively. The dyes were dissolved so to prepare the stock solutions of 1000 mg dm^{-3}, (2.6 and 3.1 mmol dm^{-3}, respectively) and different concentrations were obtained by diluting the stock solutions. To change the pH of the dye solutions, either 0.1 mol dm^{-3} NaOH or 0.2 mol dm^{-3} H_2SO_4 solutions were added.

2. 5. Batch adsorption experiments

Adsorption experiments were carried out in batch mode in 150 cm^3 beakers placed on a shaker at 150 rpm. In each beaker, a dose of LPSH was carefully mixed with 100 ± 1.0 cm^3 of BCB or MeO solutions for studying the influence of factors such as the adsorbent dose, pH, contact time, initial concentration and temperature. A series of batch adsorption experiments were conducted with factors modified according to the One-Factor-at-a-Time (OFAT) method [12]. The experiments involved different conditions, as shown in Table 1.

All dye samples were filtered and diluted to measure the dye concentrations before, after, and at equilibrium adsorption using an UV-Visible spectrophotometer (UVILINE 9400, France) at maximum wavelengths: λ_{max}=627 nm for BCB and λ_{max}=465 nm for MeO at pH≥4, λ_{max}=508 nm for MeO at pH <4 (Fig. 1). The experiments were repeated and measured three times for accuracy.

Table 1. *Experimental conditions for investigating the effects of different adsorption factors*

Experiment	Factor	Conditions
1	Adsorbent mass: 0 to 1 g	Initial concentration = 15 mg dm^{-3} (39 μmol dm^{-3} for BCB and 46 μmol dm^{-3} for MeO) pH 3.7 for BCB and pH 6.62 for MeO Contact time = 180 min Temperature = 298 K
2	pH solution: 2 to 8	Initial concentration = 15 mg dm^{-3} (39 μmol dm^{-3} for BCB and 46 μmol dm^{-3} for MeO) Adsorbent mass = 0.1 g for BCB and 0.2 g for MeO Contact time = 180 min Temperature = 298 K
3	Contact time: 0-180 min	Initial concentration = 50 mg dm^{-3} (130 μmol dm^{-3} for BCB and 153 μmol dm^{-3} for MeO) pH = 5 for BCB and pH=7 for MeO Adsorbent mass = 0.1 g for BCB and 0.2 g for MeO Temperature = 298 K
4	Initial concentration: 15 to 100 mg dm^{-3} (39 to 259 μmol dm^{-3} for BCB; 46 to 305.5 μmol dm^{-3} for MeO)	Adsorbent mass = 0.1 g for BCB and 0.2 g for MeO pH 5 for BCB and pH 7 for MeO Contact time = 20 min for BCB and 90 min for MeO Temperature = 298 K
5	Temperature: 298-328 K	Initial concentration = 50 mg dm^{-3} (130 μmol dm^{-3} for BCB and 153 μmol dm^{-3} for MeO) pH 5 for BCB and pH 7 for MeO Contact time = 20 min for BCB and 90 min for MeO Adsorbent mass = 0.1 g for BCB and 0.2 g for MeO

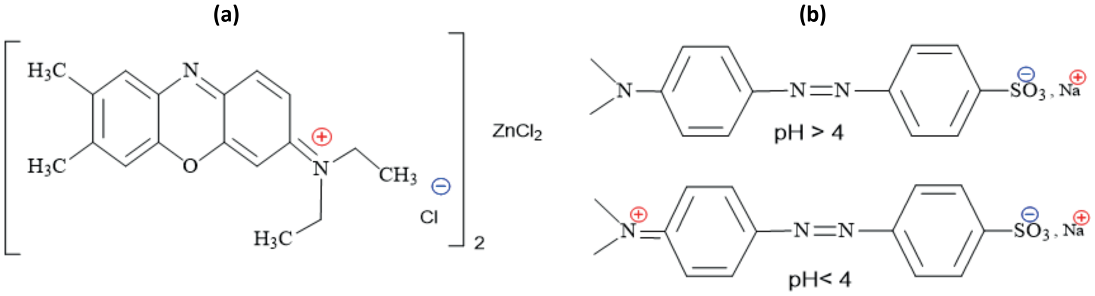

Figure 1. *Chemical structures of (a) - brilliant cresyl blue and (b) - methyl orange*

In order to quantify the adsorption performance of LPSH for BCB and MeO, the amounts of dyes adsorbed per unit mass of LPSH, Q, were calculated using the following equation:

$$Q = \frac{(C_i - C_t)V}{W} \tag{1}$$

where C_i and C_t are the initial and concentration at time t, respectively, V is the volume of dye solution, and W is the weight of the LPSH adsorbent.

2. RESULTS AND DISCUSSION

3. 1. Adsorbent characterization

Infrared spectroscopy analyses (FTIR) were performed to determine functional groups characterizing this LPSH adsorbent (Figure 2).

The spectrum shows a large band at 3432.71 cm^{-1}, which is attributed to the stretching vibration of O-H hydroxyl groups or amine groups (N–H). While aliphatic C-H stretching vibrations are characterized by a band between 2907.19 and 2843.15 cm^{-1}. It was determined, from the LPSH spectrum, that the carbonyl (C=O) stretch at 1735.37 cm^{-1} indicates the presence of a carbonyl-containing functional group (carboxylic acid, ketone, aldehyde, or lactone). The asymmetric stretch of a carboxylate (COO^-) group is indicated by the band at 1592.34 cm^{-1}. The aromatic C=C stretching vibrations are characterized by two additional bands at 1424.59 and 1377.26 cm^{-1}. The band at 1034.10 cm^{-1} was assigned to C-O-C ether groups. The results obtained by this spectrum are similar to those observed for other lignocellulosic materials [13,14].

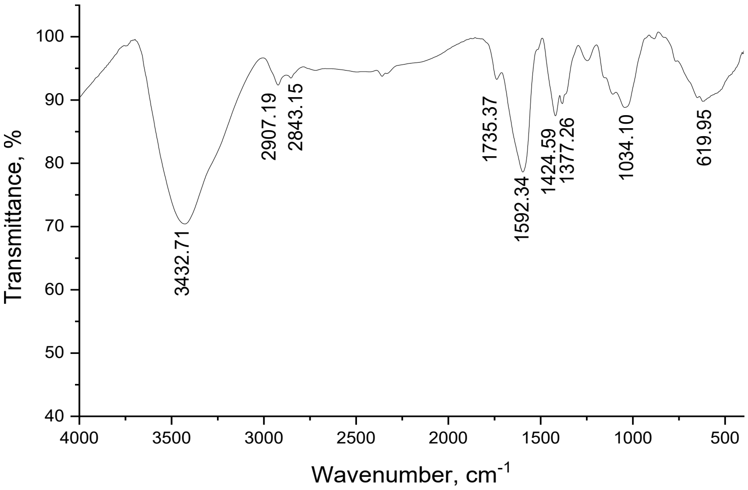

Figure 2. *FTIR spectrum of pumpkin seed husks*

Morphology analysis and elemental identification were performed by using an SEM-EDX device, providing the results reported in Figure 3 and Table 2. The results show that LPSH has a heterogeneous and rough surface, which contains few holes and cavities. Elemental identification at the EDX spectrum confirmed that the adsorbent LPSH consists of molecules containing carbon (C) and oxygen (O) with major weight of 51.85 % for C (with a specific measurement repetition of 0.9405) and 48.15 % for O (with a specific measurement repetition of 0.9495).

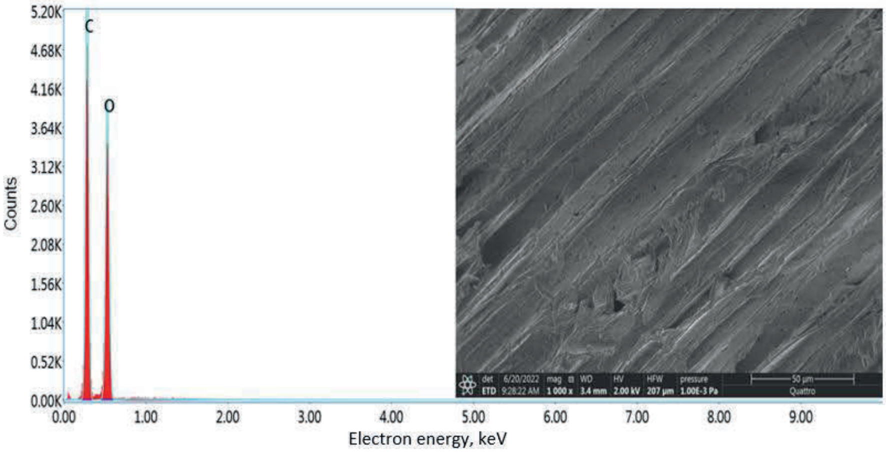

Figure 3. *SEM micrograph and EDX spectrum of pumpkin seed husks*

Table 2. *Elemental identification of pumpkin seed husks by the EDX analysis*

Element	Content, wt.%	Content, at.%	Error, %	Net Intensity
C K	51.85	58.92	7.51	522.93
O K	48.15	41.08	8.90	427.88

According to the X-ray analysis of an LPSH sample shown in Figure 4, there are three peaks at 2θ angles of 16.07, 22.34 and 34.30°. The presence of distinct peaks at 22.34 and 34.30° indicates semi-crystalline regions, while the broader feature around 16.07° suggests an amorphous component structures of pumpkin seed husks. This structure typically distinguishes agricultural materials , consisting of cellulose, lignin, and hemicellulose [15,16].

BET and BJH methods were used to quantify the surface area and porosity of a LPSH sample by studying nitrogen adsorption and desorption isotherms. The results shown in Figure 5 indicate that the obtained N_2 isotherm is classified as type IV (H3) according to the IUPAC classification, signifying a mesoporous material with slit-shaped pores in plate-like aggregates, showing multilayer adsorption, capillary condensation and complex pore connectivity [17]. The BET surface area was measured as 1.5300 ± 0.0272 m² g^{-1}, with a total pore volume of 0.0014 cm³ g^{-1} and an average pore diameter of 3.70 nm. Furthermore, the pore size in the range of 2 to 50 nm corresponds to mesoporous materials [18].

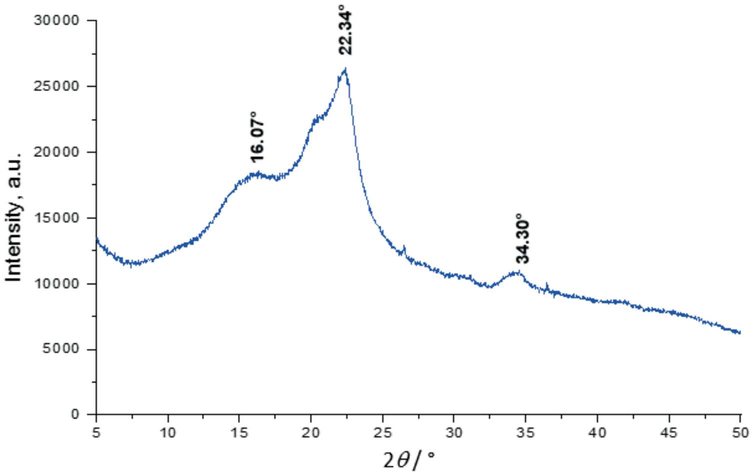

Figure 4. *X-ray diffraction analysis of pumpkin seed husks*

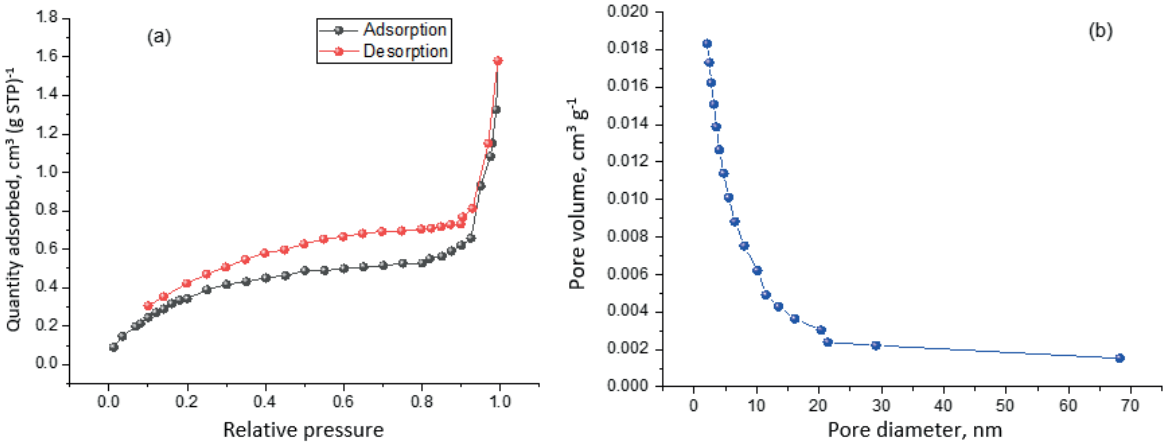

Figure 5. *BET analysis of N_2 adsorption-desorption isotherm (a) and pore size distribution of LPSH (b)*

3. 2. Effect of physico-chemical parameters

3. 2. 1. Effect of pH

The pH of a dye solution is important factor in any adsorption study, as it affects the charge of the adsorbent's surface and the behaviour of the adsorbed ions [19]. The result of this test is illustrated in Figure 6(a). Due to electrostatic interactions between the anionic dye MeO and the positive sites of LPSH, MeO dye is adsorbed most effectively at pH 7 [20].

In the case of the cationic dye (BCB), adsorption increases by rising the pH, indicating less competition for negative sites on the surface of the adsorbent, reaching its maximum at pH 5.

3. 2. 2. Effect of contact time

Generally, increasing contact time results in an increase in the adsorbed amount until reaching the equilibrium, as was also obtained in the present study (Fig. 6(b)). The BCB adsorption reaches equilibrium after 20 min, while for dye MeO the equilibrium is reached after 90 min. This difference is attributed to the higher number of active sites available on the adsorbent surface for the BCB dye as compared to those available for dye MeO the initial dye concentrations were 130 and 153 µmol/md^{-3} for BCB and MeO, respectively, while the equilibrium adsorbed amounts were 209 and 25 µmol/g, for BCB and MeO. A similar pattern of behaviour for the adsorption of dyes BCB and MeO was observed in other related research [21,22].

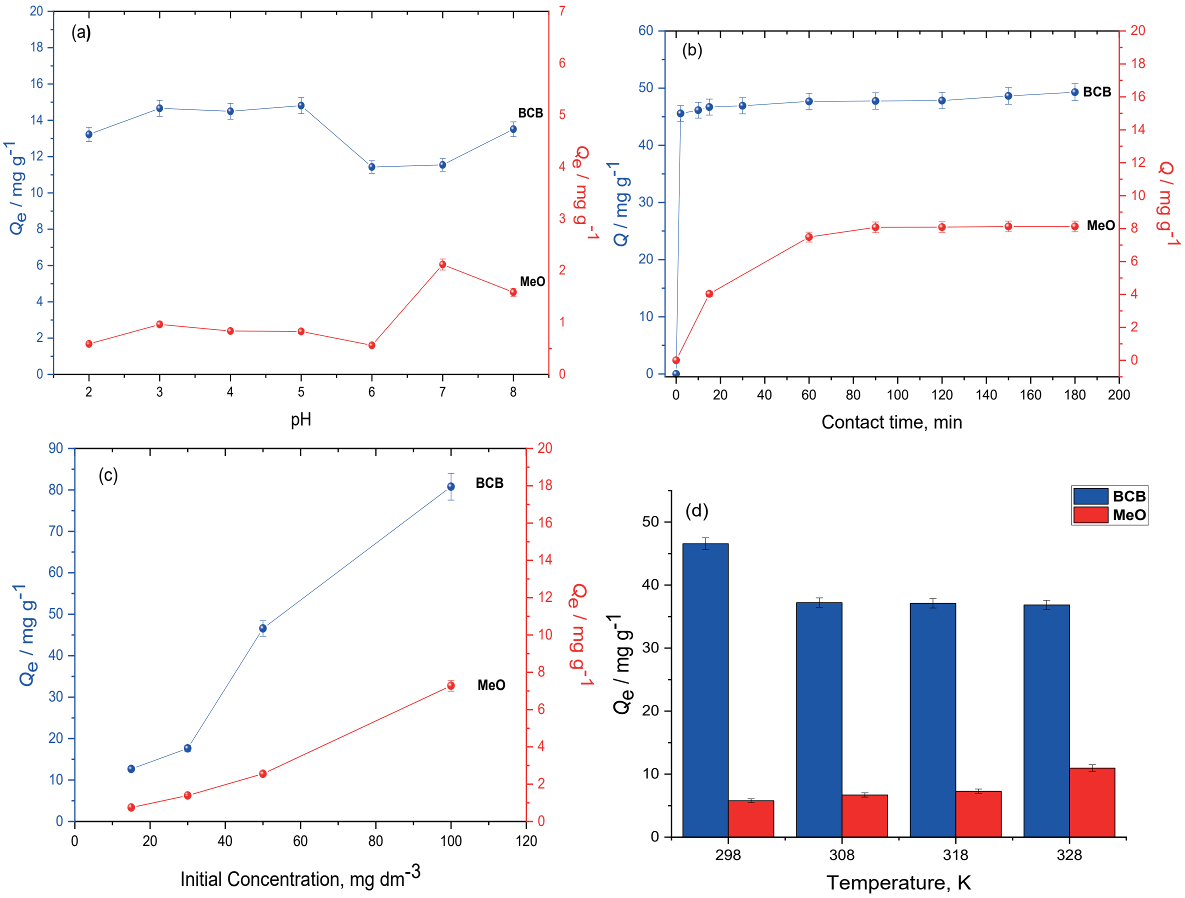

Figure 6. *Adsorption of BCB and MeO onto LPSH: (a) - equilibrium adsorbed dye amount per the adsorbent mass (Q_e) as a function of the solution pH, (b) - adsorbed dye amount per Q as a function of the contact time, (c) - equilibrium adsorbed dye amount per Q_e as a function of the initial dye concentration, (d) - equilibrium adsorbed dye amount per Q_e as a function of the temperature; all experimental conditions for each experimental series are provided in Table 1*

3. 2. 3. Effect of initial concentration

As shown in Figure 6(c), the increase in adsorbed amounts is observed with an increase in the initial concentrations of BCB and MeO, as expected. However, it can be concluded that both dyes do not occupy all the active sites of the adsorbent.

3. 2. 4. Effect of temperature

The influence of temperature on the adsorption of MeO and BCB was studied in the range 298 to 328 K (Fig. 6(d)). It can be noted that that as the temperature rises, the amount of BCB that can be adsorbed decreases slightly (indicating an inverse relationship). This can be explained by the weakening of the bonds between BCB and the active sites of the adsorbent. The results suggest that the adsorption of BCB by LPSH adsorbent is exothermic. In contrast, in the case of MeO, the adsorbed amount increases with rising the temperature. This is because the mobility of MeO molecules increases at higher temperatures, enhancing the interaction between MeO and the active sites of the adsorbent LPSH. The obtained result indicate that adsorption of MeO by LPSH is an endothermic process [23].

3. 3. Adsorption isotherm studies

Adsorption is governed by mathematical equations that relate the adsorbed amount to the equilibrium concentration of the solute. Thus, the adsorbed amount (per unit adsorbent mass) plotted as a function of the equilibrium concentration at constant temperature represents the adsorption isotherm. Among the most commonly used isothermal models are the Freundlich [24] and Langmuir [25] isotherms.

The results obtained allowed for the plotting of linear shapes according to the Freundlich (Equation (2)) and the Langmuir (Equation (3)) isothermal models (Figure 7), enabling calculation of the various constants for both models.

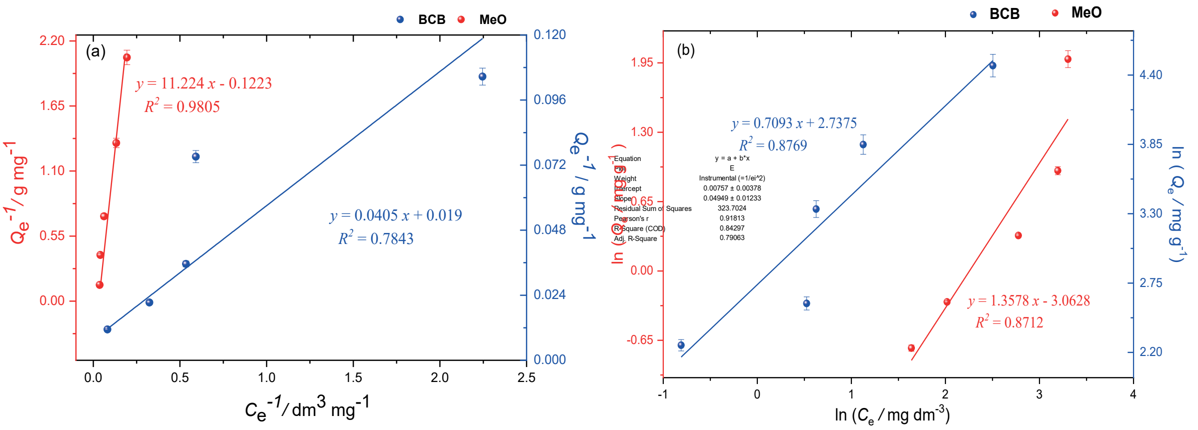

Figure 7. *Linear fits of Langmuir (a) and Freundlich (b) isotherms and equilibrium data for BCB and MeO adsorption onto LPSH, experimental conditions: initial dye concentrations C_0: 15 to 100 mg dm^{-3}(39 µmol dm^{-3} for BCB and 46 µmol dm^{-3} for MeO); W = 0.1 g for BCB and 0.2 g for MeO; pH 5 for BCB and pH 7 for MeO; contact time 20 min for BCB and 90 min for MeO; T = 298 K*

$$\ln Q_e = 1/n \ln C_e + \ln K_F \quad (2)$$

$$1/Q_e = 1/Q_m + 1/K_L Q_m \, 1/C_e \quad (3)$$

where Q_m / mg g^{-1} is the maximum adsorption capacity of a saturated monolayer onto the adsorbent's surface; K_L / dm^3 mg^{-1} is the rate constant of the Langmuir model; K_F / mg^{1-n} dm^{3n} g^{-1} is the Freundlich constant of the maximum adsorption capacity and n is the empirical constant related to the adsorbent surface heterogeneity.

The calculated constants of the Freundlich and Langmuir models show that the Freundlich isotherm was best adapted to the experimental results, with a correlation coefficient R^2 of 0.8769, with a maximum experimental BCB adsorption of 80.7± 4.0 mg g^{-1} (209 ± 10 µmol g^{-1}) indicating the possibility of multilayer adsorption of BCB onto LPSH [26]. For MeO adsorption the results obtained show that the Langmuir isotherm provided the best fit to the experimental data, with a correlation coefficient R^2 of 0.9805, and the calculated maximum adsorption capacity of MeO was 8.2 ± 0.0 mg g^{-1} (25 ± 0 µmol g^{-1}), suggesting a homogeneous monolayer arrangement of MeO dye on the LPSH surface [27].

3. 4. Thermodynamic studies

Thermodynamic parameters such as the enthalpy change (Δ*H*°), entropy change (Δ*S*°) and free energy change (Δ*G*°) are essential for a better understanding of the temperature effects on the energies of adsorption.

The values of Δ*H*° and Δ*S*° were estimated from the graphical presentation of Δ*G*° as a function of temperature *T* according to Equations (4), (5) and (6) [28]:

$$K_d = \frac{Q_e}{C_e} \quad (4)$$

$$\Delta G^\circ = -RT \ln K_d \quad (5)$$

$$\Delta G^\circ = \Delta H^\circ - T\Delta S^\circ \quad (6)$$

where R is the ideal gas constant, 8.314 J mol$^{-1}\cdot$K^{-1}; T / K is temperature and K_d is the distribution constant.

Figure 8 shows the evaluation of thermodynamic parameters with respect to temperature of BCB and MeO adsorption onto pumpkin seed husks. From the obtained curves, which include the thermodynamic parameters for BCB and MeO adsorption, we observe that Δ*G*° as a function of temperature is linear, and its negative values (-6.46 to -1.98 kJ mol^{-1}) indicate the spontaneous adsorption of BCB, while the adsorption of MeO is non-spontaneous process (Δ*G*°= 4.92 to 2.87 kJ mol^{-1}) [16]. Moreover, the positive values of Δ*H*° (+25.01 ± 1.17 kJ mol^{-1}) suggest endothermic process of MeO and the negative values of Δ*S*° (-67.64 ± 3.74 J mol^{-1} K^{-1}) indicate an increasing order at the interface LPSH/MeO during this adsorption. In contrast, the adsorption of BCB onto LPSH is an exothermic process (Δ*H*°=-45.31 ± 17.72 kJ mol^{-1} < 0) [29], with an increase in randomness between the BCB dye and the LPSH adsorbent (Δ*S*°= +133.60 ± 56.59 J mol^{-1} K^{-1} > 0) [30].

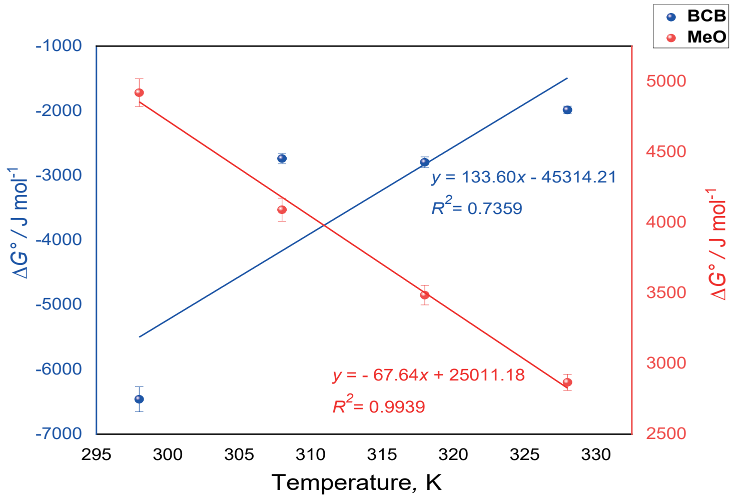

Figure 8. *Linear plots of free energy versus temperature, experimental conditions: C_0: 50 mg dm^{-3} (130 μmol dm^{-3} for BCB and 153 μmol dm^{-3} for MeO); W = 0.1 g for BCB and 0.2 g for MeO; pH 5 for BCB and pH 7 for MeO; contact time = 20 min for BCB and 90 min for MeO; T = 298 to 328 K; shaker speed = 150 rpm.*

3. 5. Comparative studies

The pumpkin seed husk adsorbent used in the present study exhibited superior BCB dye adsorption compared to previous studies using raw, unmodified agricultural residues (Table 3), achieving high removal efficiency in a significantly shorter time-frame, while the results for dye MeO adsorption were acceptable.

Table 3. *Comparative evaluation of agricultural waste materials as adsorbents for BCB and MeO dyes*

Adsorbents	Adsorbates	Isotherm model	Adsorption capacity, mg g^{-1}	Ref.
Inula Racemosa leaves	BCB	Freundlich	3.49 at 10 min	[31]
Peanut hull			4.39 at 12 h	[32]
Pumpkin seed husks			80.7 at 20 min	Present work
Anchote peel	MeO		103.03 at 140 min	[33]
Palm fibers		Langmuir	48.79 at 120 min	[34]
Sawdust			50.52 at 120 min	[34]
Pumpkin seed husks			8.2 at 90 min	Present work

4. CONCLUSION

With the aim of evaluating the efficiency of Algerian pumpkin seed husks in removing cationic and anionic dye pollutants, this research has focused first on studying the characteristics of the surface of this adsorbent. The results indicate that the surface of the seed husks is not homogeneous; it is rough and consists of mesopores, with a significant specific surface area of 1.53 ± 0.027 m² g^{-1} and is rich in organic chemical groups responsible for the fixation of BCB and MeO dyes through electrostatic attraction and hydrogen bonds.

The results obtained in the adsorption studies allowed us to advance the following points:

Isothermal study: the adsorption of BCB dye was well described by the Freundlich isotherm, with a maximum adsorption capacity of 80.7± 4.038 mg g^{-1} (209 ± 10 μmol g^{-1}). In contrast, the Langmuir isotherm was more favorable for the adsorption of MeO dye onto LPSH, with a maximum adsorption capacity of 8.2 ± 0.004 mg g^{-1} (25 ± 0 μmol g^{-1}).

Thermodynamic study: the results show that the adsorption process for BCB dye using the LPSH adsorbent was spontaneous and exothermic, while the adsorption process for MeO dye was non-spontaneous and endothermic.

Overall, the results of our work indicate that this study is significant in demonstrating that raw LPSH has an acceptable and favorable adsorption capacity compared to other adsorbents.

Acknowledgement: The authors gratefully acknowledge the support and accompaniment of the Directorate General of Scientific Research and Technological Development Algeria and the Algerian Ministry of Higher Education and Scientific Research.

REFERENCES

[1] Chaudhry FN, Malik MF. Factors Affecting Water Pollution. *A Rev J Ecosyst Ecography.* 2017; 7(225): 1-3. https://doi.org/10.4172/2157-7625.1000225

[2] Hussain S, Khan N, Gul S, Khan S, Khan H. *Contamination of Water Resources by Food Dyes and Its Removal Technologies.* In Water Chemistry. *Eds; Intech Open London, UK,* 2020. https://doi.org/10.5772/intechopen.90331

[3] Iwuozor KO, Ighalo JO, Emenike EC, Ogunfowora LA, Igwegbe CA. Adsorption of methyl orange: A review on adsorbent performance. *Curr Res Green Sustain Chem.* 2021; 4: 100179. https://doi.org/10.1016/j.crgsc.2021.100179

[4] Al-Gubury HY, Alteemi HS, Saad AM , Al-Shamary RR. Removal of Hazardous Brilliant Cresyl Blue Dye Utilizing Aluminum Oxide as Photocatalyst. *Indones J Chem.* 2019; 19(2): 292-297. https://doi.org/10.22146/ijc.30135

[5] Alhujaily A., Yu H., Zhang X. Ma F. Adsorptive removal of anionic dyes from aqueous solutions using spent mushroom waste. *Appl Water Sci.* 2020; 10: 183. https://doi.org/10.1007/s13201-020-01268-2

[6] Cako E, Gunasekaran KD, Soltani RDC, Boczkaj G. Ultrafast degradation of brilliant cresyl blue under hydrodynamic cavitation based advanced oxidation processes (AOPs). *Water Resour Ind.* 2020; 24: 100179. https://doi.org/10.1016/j.wri.2020.100134

[7] Adegoke KA, Bello OS. Dye sequestration using agricultural wastes as adsorbents. *Water Resour Ind.* 2015; 12: 8-24. https://doi.org/10.1016/j.wri.2015.09.002

[8] Zulti F, Setiadewi N, Waluyo A, & Susanti E. Removal pollutants in textile wastewater using unmodified rice husk. *E3S Web Conf.* 2024; 483: 02008. https://doi.org/10.1051/e3sconf/202448302008

[9] Yetgin S, Amlani M. Agricultural low-cost waste adsorption of methylene blue and modelling linear isotherm method versus nonlinear prediction. *Clean Technol Environ Policy*. 2024. https://doi.org/10.1007/s10098-024-02928-6

[10] Alivio RKO, Go AW, Angkawijaya AE, Santoso SP, Gunarto C, Soetaredjo FE. Extractives-free sugarcane bagasse as adsorbent for the removal of Rhodamine B (Basic Violet 10) with high capacity and reusability. *J Ind Eng Chem*. 2023; 124: 175-200. https://doi.org/10.1016/j.jiec.2023.04.007

[11] Ad C, Benalia M, Laidani Y, Elmsellem H, Henini G, Nouacer I, Djedid M. Kinetics, thermodynamics and equilibrium evaluation of adsorptive removal of iron from aqueous solution onto Algerian biosorbent “LUFFA CYLINDRICA.” *J Mater Environ Sci.* 2016; 7(1): 319-30. https://www.jmaterenvironsci.com/Document/vol7/vol7_N1/34-JMES-1968-2012-Ad.pdf

[12] Frey DD, Wang H. Adaptive One-Factor-at-a-Time Experimentation and Expected Value of Improvement. *Technometrics*. 2006; 48(3): 418-431. https://doi.org/10.1198/004017006000000075

[13] Awoyale AA, Lokhat D. Experimental determination of the effects of pretreatment on selected Nigerian lignocellulosic biomass in bioethanol production. *Sci Rep.* 2020; 11: 557. https://doi.org/10.1038/s41598-020-78105-8

[14] Khalfaoui A, Khelifi MN, Khelfaoui A, Benalia A, Derbal K, Gisonni C, Crispino G, Panico A A. The Adsorptive Removal of Bengal Rose by Artichoke Leaves: Optimization by Full Factorials Design. *Water.* 2022; 14(14): 2251. https://doi.org/10.3390/w14142251

[15] Ishak WHW, Ahmad I, Ramli S, Amin MCIM. Gamma Irradiation-Assisted Synthesis of Cellulose Nanocrystal-Reinforced Gelatin Hydrogels. *Nanomaterials.* 2018; 8: 749. https://doi.org/10.3390/nano8100749

[16] Kali A, Amar A, Loulidi I, Hadey C, Jabri M, Alrashdi AA, Lgaz H, Sadoq M. Efficient Adsorption Removal of an Anionic Azo Dye by Lignocellulosic Waste Material and Sludge Recycling into Combustible Briquettes. *Colloids Interfaces.* 2022; 6: 22. https://doi.org/10.3390/colloids6020022

[17] Purbasari A, Ariyanti D, Sumardiono S, Masyaroh M, Salsabila TR. Physical properties and structural characteristics of alkali modified fly ash. *J Phys Conf Ser.* 2021; 1912: 012012. https://doi.org/10.1088/1742-6596/1912/1/012012

[18] Horvat G, Pantic M, Knez Z, Novak Z. A Brief Evaluation of Pore Structure Determination for Bioaerogels. *Gels.* 2022; 8(7): 438. https://doi.org/10.3390/gels8070438

[19] Wawrzkiewicz M, Hubicki Z. Removal of tartrazine from aqueous solutions by strongly basic polystyrene anion exchange resins. *J Hazard Mater.* 2009; 164: 502-509. https://doi.org/10.1016/j.jhazmat.2008.08.021

[20] Estefan E, Elystia S, Kuan WH, Sasmita A. Removal of methyl orange textile dye using magnetic chitosan microspheres adsorbent. *Water Pract Technol.* 2023; 18(12): 3280-3290. https://doi.org/10.2166/wpt.2023.201

[21] Pourreza N, Mirzajani R, Behbahani MT. Removal of brilliant cresyl blue from aqueous solutions using modified zirconia nanoparticles as an adsorbent under ultrasonic action. *Desalin Water Treat.* 2016; 57: 28999-9006. https://doi.org/10.1080/19443994.2016.1193060

[22] Kurniawati D, Sari TK, Adella F, Sy S. Effect of Contact Time Adsorption of Rhodamine B, Methyl Orange and Methylene Blue Colours on Langsat Shell with Batch Methods. 1st Int. Conf. Chem. Sci. Educ. (ICChSE), *J Phys Conf Ser.* 2021; 1788: 012008. https://doi.org/10.1088/1742-6596/1788/1/012008

[23] Wong S, AbdGhafar N, Ngadi N, Razmi FA, Inuwa IM, Mat R, Amin NS. Effective removal of anionic textile dyes using adsorbent synthesized from cofee waste. *Sci Rep.* 2020; 10: 2928. https://doi.org/10.1038/s41598-020-60021-6

[24] Freundlich H, Helle WJ. The Adsorption of cis- and trans-Azobenzene. *J Am Chem Soc.* 1939; 61(8): 2228-30. https://doi.org/10.1021/ja01877a071

[25] Langmuir I. The adsorption of gases on plane surfaces of glass. *J Am Chem Soc.* 1918; 40: 1361-402. https://doi.org/10.1021/ja02242a004

[26] Badri N, Zbair M, Sahibed-Dine A, Chhiti Y, Khamliche L, Bensitel M. Adsorption of Cationic Dyes by Waste Biomass Treated by Phosphoric Acid. *J Mater Environ Sci.* 2018; 9: 1636-1644. https://doi.org/10.26872/jmes.2018.9.6.182

[27] Janet A, Kumaresan R, Uma Maheswari S. Adsorption of Anionic and Cationic Dyes onto Granular Activated Carbon. *Middle-East J Sci Res.* 2015; 23(2): 308-17. https://doi.org/10.5829/idosi.mejsr.2015.23.02.22114

[28] Saha P, Chowdhury S. Insight into adsorption thermodynamics. *Thermodynamics*. 2011; 16: 349-64. https://doi.org/10.5772/13474

[29] Adheem HM, Jasim LS. Preparation and Characterization of a three-component hydrogel composite and study of kinetic and thermodynamic applications of adsorption of some positive and negative dyes from their aqueous solutions. 2nd Int. Sci. Conf. Al-Ayen Univ. IOP Conference Series: *IOP Conf Ser Mater Sci Eng*. 2020; 928: 052027. https://doi.org/10.1088/1757-899X/928/5/052027

[30] Mandal B, Ray SK. Removal of safranine T and brilliant cresyl blue dyes from water by carboxy methyl cellulose incorporated acrylic hydrogels: Isotherms, kinetics and thermodynamic study. *J Taiwan Inst Chem Eng.* 2016, 60: 313-327. https://doi.org/10.1016/j.jtice.2015.10.021

[31] Amara-Rekkab A. Efficient Removal of Brilliant Cresyl Blue from Solution Using *Inula racemosa*: Experimental Insights, DFT Modeling, and Docking Simulation. *Sep. Sci Technol.* 2024; 9(41): e202403331. https://doi.org/10.1002/slct.202403331

[32] Gong R, Li M, Yang C, Sun Y, Chen J. Removal of cationic dyes from aqueous solution by adsorption on peanut hull. *J Hazard. Mater.* 2005; 121(1-3):247-250. https://doi.org/10.1016/j.jhazmat.2005.01.029

[33] Hambisa AA, Regasa MB, Ejigu HG, & Senbeto CB. Adsorption studies of methyl orange dye removal from aqueous solution using Anchote peel-based agricultural waste adsorbent. *Appl Water Sci.* 2023; 13(24). https://doi.org/10.1007/s13201-022-01832-y

[34] Dakhil IH. Recycling of Agriculture Wastes for Efficient Removal of Methyl Orange Dye Using Batch Adsorption Unit. *IOP Conf. Ser.: Mater Sci Eng.* 2020; 881(1): 012186. https://doi.org/10.1088/1757-899X/881/1/012186

Ispitivanje efikasnosti prirodnog materijala za uklanjanje katjonskih oksazin- i anjonskih azo- boja iz vodenih rastvora

Asma Boudaoud[1], Chifaa Ad[2], Mebrouk Djedid[2], Mokhtar Benalia[2], Mounira Guermit[1] and Soltani Amel[3]

[1]Laboratory of Process Engineering, Materials and Environmental, Department of Common Trunk Science and Technology; Faculty of Technology, Amar Telidji University of Laghouat, Laghouat, Algeria
[2]Laboratory of Process Engineering, Materials and Environmental, Department of Process Engineering, Faculty of Technology, Amar Telidji University of Laghouat, Laghouat, Algeria
[3]Higher Normal School of Laghouat, Laghouat, Algeria

(Stručni rad)

Izvod

U ovom radu je ispitan procese adsorpcije boja brijant krezol plave (BCB) i metil narandžaste (MeO) na ljuske semena bundeve sa lokalnog područja (LPSH). LPSH adsorbent je analiziran primenom infracrvene spektroskopije sa Furijeovom transformacijom, skenirajuće electron-ske mikroskopije sa spektroskopijom rendgenskih zraka disperzivne energije, difrakcije rendgenskih zraka i Brunauer-Emmett-Teller analizom. Deskriptivnom analizom morfologije LPSH utvrđena je heterogena površina, dok je strukturnom analizom utvrđeno prisustvo funkcionalnih grupa tipičnih za lignocelulozne strukture. Potvrđena je mezoporozna površina adsorbenta, specifične površine ~1,53 m^2 g^{-1}. Studije izotermne adsorpcije sugerišu da je Langmuirov model najbolje opisao adsorpciju MeO, dok je Frojndlihov model pogodniji za opisivanje adsorpcije BCB. Prema termodinamičkim analizama, adsorpcija BCB je bila egzotermna i spontana, dok je adsorpcija MeO bila endotermna i nespontana. Rezultati procene efikasnosti LPSH adsorbenta su pokazali da su maksimalni kapaciteti adsorpcije ~81 mg g^{-1} za BCB boju i ~8,2 mg g^{-1} za MeO boju.

Ključne reči: Briljantna krezol plava; metil narandžasta; adsorpcija; ljuske semena bundeve; rastvori sintetičkih boja